Terminally Exhausted CD8$^+$ T Cells Resistant to PD-1 Blockade Promote Generation and Maintenance of Aggressive Cancer Stem Cells

Mohona Chakravarti[1], Sukanya Dhar[1], Saurav Bera[1], Abhipsa Sinha[2], Kamalika Roy[3], Anirban Sarkar[1], Shayani Dasgupta[1], Avishek Bhuniya[1], Akata Saha[1], Juhina Das[1], Saptak Banerjee[1], Manisha Vernekar[4], Chiranjib Pal[3], Neyaz Alam[5], Dipak Datta[2], Rathindranath Baral[1], and Anamika Bose[1]

ABSTRACT

Heterogeneity within the tumor-infiltrating lymphocytes (TIL) population limits immunotherapeutic efficacy against cancer. Between two subpopulations of exhausted CD8$^+$ TILs (progenitor-exhausted; T_{PEX}, terminally exhausted; T_{TEX}), T_{TEX} cells remain unresponsive to anti–programmed cell death protein 1(PD-1) therapy. Deciphering whether and how PD-1–resistant T_{TEX} cells engage in tumor promotion could improve the response to immunotherapy. Here, we report that T_{TEX} cells actively participate in tumor progression by modulating cancer stem cells (CSC). T_{TEX} cells strongly correlated with elevated CSC frequency in poorly immune-infiltrated (CD8$^+$ TIL low) advanced human breast and ovarian carcinomas. T_{TEX} directly upregulated CSC frequency *in vitro*, which was not affected by anti–PD-1 treatment. The T_{TEX}-influenced CSCs were highly clonogenic and exhibited a multidrug-resistant phenotype, overexpressing drug efflux pumps like ABCC1 and ABCB1. These CSCs were highly invasive, displaying increased invadopodia development and elevated cofilin, CXCR4, and matrix metalloproteinase 7 (MMP7) expression. The invasive properties along with epithelial–mesenchymal plasticity of T_{TEX}-educated CSCs increased metastasis *in vivo*. T_{TEX} increased cell surface levels and activation of VEGFR2 in CSCs, and silencing or inhibition of VEGFR2 reversed the CSC-stimulatory effects of T_{TEX}. LAMP3 and NRP1 on the surface of T_{TEX} stimulated VEGFR2 in CSCs to promote aggressiveness. Cumulatively, these findings suggest that screening patients with carcinoma for both CD8$^+$ TILs and T_{TEX} frequency prior to anti–PD-1 therapy could improve patient outcomes. In addition, targeting the LAMP3/NRP1–VEGFR2 axis could be a therapeutic strategy in advanced patients with carcinoma with limited CD8$^+$ T-cell infiltration and high T_{TEX} frequency.

Significance: Cross-talk with T_{TEX} CD8$^+$ T cells mediated by the VEGFR2 axis induces aggressive properties in cancer stem cells to promote tumor progression.

Introduction

Intratumoral complexity poses a significant challenge in successful cancer management. A self-renewing rare subset of stem cells, designated as cancer stem cells (CSC), fuels such heterogeneity (1). CSCs remain arrested in a quiescent state; only transiently proliferate to generate heterogeneous malignant tumor bulk, which is generally non-CSC and can seldom foster tumors in xenograft assays (2). However, this hierarchy is not always maintained; plasticity and dedifferentiation of terminally differentiated malignant cells to CSC-like state are also evident under specific conditions (3–4). Intratumoral CSC-supportive niches protect from diverse genotoxicities, by overexpressing ABC-drug efflux proteins, enhancing DNA repair mechanisms, resisting DNA damage and upregulating antiapoptotic proteins (5–7). Tumor-intrinsic hypoxia feeds this flame via upregulation of HIF1α, conferring enhanced therapy resistance and resulting into relapse (8). CSCs also initiate metastasis and secondary tumor formation by inducing extracellular matrix (ECM) reorganization, epithelial–mesenchymal transition (EMT), neovascularization, vascular mimicry, and seeding at the secondary site (9–13).

Substantial evidence suggests the importance of immune cells in regulating CSC fate, like tumor-associated macrophage (TAM), myeloid-derived suppressor cell (MDSC) and Tregs support CSCs, while natural killer (NK) and γδT cells function against it (14–19). Immune-suppressive network increases CSC frequency, stemness, and aggressive phenotypes (20). CSC survival is further ensured due to the truncation of the effector response from infiltrated CD8$^+$ T cells. Within the tumor microenvironment (TME), CD8$^+$ T cells undergo a hierarchical loss of proliferation and effector functions, including the secretion of IL2, TNFα, IFNγ, and β chemokines, as a result of prolonged antigenic exposure and an immune-suppressive milieu. In this "exhausted" state, they show a sustained overexpression of coinhibitory receptors, such as programmed cell death protein 1 (PD-1), TIM3, LAG3, CTLA4, and TIGIT. These hyporesponsive exhausted CD8$^+$ T cells fail to regulate tumor growth (21–24).

[1]Department of Immunoregulation and Immunodiagnostics, Chittaranjan National Cancer Institute (CNCI), Kolkata, India. [2]Cancer Biology Division, CSIR-Central Drug Research Institute, Lucknow, Uttar Pradesh, India. [3]Cellular Immunology & Experimental Therapeutics Laboratory, Department of Zoology, West Bengal State University, Barasat, Kolkata, West Bengal, India. [4]Department of Gynecological Oncology, Chittaranjan National Cancer Institute (CNCI), Kolkata, West Bengal, India. [5]Department of Surgical Oncology, Chittaranjan National Cancer Institute (CNCI), Kolkata, India.

Current address for A. Bose: Department of Pharmaceutical Technology (Biotechnology), National Institute of Pharmaceutical Education and Research (NIPER), SAS Nagar, Mohali, Punjab, India. E-mail: boseanamika@niper.ac.in

Corresponding Author: Anamika Bose, Department of Immunoregulation and Immunodiagnostics, Chittaranjan National Cancer Institute (CNCI), 37, S.P. Mukherjee Road, Kolkata 700026, India. Phone: 9103-3247-65101, ext. 334; E-mail: anamikabose2@gmail.com

Cancer Res 2023;83:1815–33

doi: 10.1158/0008-5472.CAN-22-3864

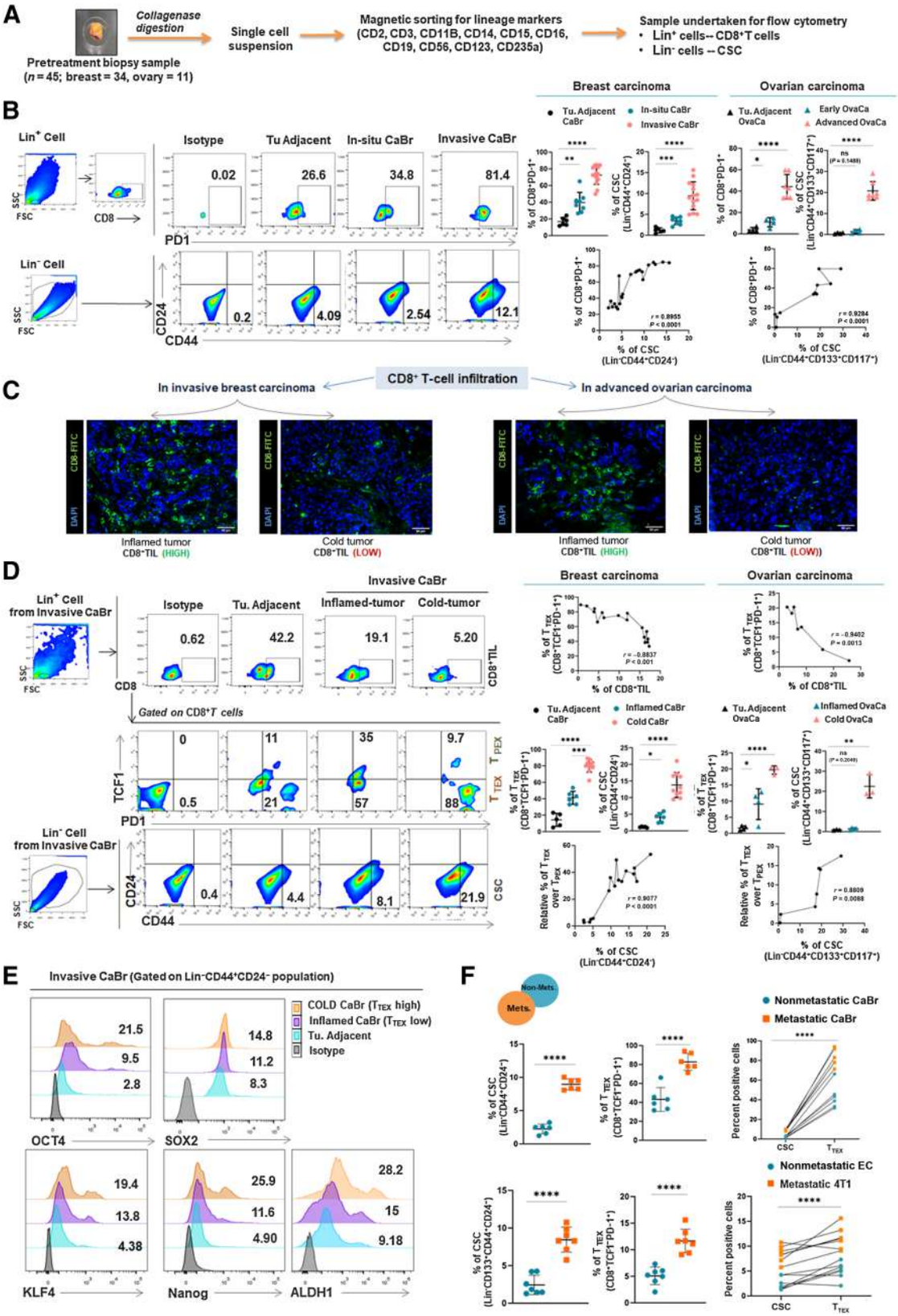

Therefore, over the past decade, numerous studies have focused on revitalization of exhausted CD8$^+$ T cells. Several immune checkpoint inhibitors (ICI) such as pembrolizumab and nivolumab (anti–PD-1), ipilimumab (anti–CTLA4), atezolizumab (anti–PD-L1) showed positive therapeutic responses in the clinical trial (25–26). However, variance within the targeted cell limited their success rate. Recent reports in human melanoma have shone light on such incongruity; existence of two subpopulations, within exhausted CD8$^+$ T-cell pool early-state progenitor exhausted (T_{PEX}; CD8$^+$ PD1$^+$ TCF1$^+$), and late-state terminally exhausted (T_{TEX}; CD8$^+$ PD1$^+$ TCF1$^-$). Although T_{PEX} cells responded to anti–PD-1 therapy, T_{TEX} cells did not (27–29). However, whether these similar subsets exist in other solid tumors remains unknown. Moreover, their behavior within TME, particularly their possible involvement in tumor advancement via CSC modulation remains unexplored.

Our study has found the coexistence of both T_{PEX} and T_{TEX} populations within infiltrated CD8$^+$ TILs of human breast and ovarian carcinoma and murine tumors. Notably, a striking positive correlation between T_{TEX} cells and CSCs was observed, indicating the possibility of their interaction for tumor promotion. Furthermore, *in vitro* and *in vivo* studies revealed that PD-1 therapy–resistant T_{TEX} cells directly generate an aggressive CSC-variant, leading to invasion and hepatic metastasis. This aggression could be neutralized by targeting the LAMP3/NRP1–VEGFR2 cascade.

Materials and Methods

Reagents and antibodies

DMEM high-glucose, minimum essential medium (MEM), RPMI1640, DMEM:F12K (1:1) media, and FBS were procured from Hi-Media. B-27 Supplement (50X) and AIM-V media were procured from Gibco. Recombinant human epidermal growth factor (rEGF) and recombinant human basic fibroblast growth factor (rbFGF) were obtained from Merck-Milipore. VEGFR2 Kinase Inhibitor I, PD-1/PD-L1 small-molecule inhibitor 1 (Abcam), Streptavidin Particles Plus-DM, antibodies for ELISA, rGM-CSF, rIL4, rTNFα, rIL1β, and rIL6 (BD Biosciences) were procured from different vendors as indicated in parentheses. Heparin, Fluoroshield with 4',6-diamidino-2-phenylindole (DAPI) and β-mercaptoethanol were purchased from Sigma-Aldrich. A detailed list of the utilized antibodies is provided in Supplementary Table S1.

Human solid tumors

Postoperative tumors (breast, $n = 34$; ovary, $n = 11$) and tumor-adjacent tissues with proven histopathologic normalcy were obtained from Chittaranjan National Cancer Institute (CNCI, Kolkata, India) following approval from Institutional Ethical Committee (IEC; approval no: CNCI-IEC-RB-2019–6). The IEC is registered under Central Drugs Standard Control Organization (CDSCO), Government of India. For breast carcinoma, tumor–node–metastasis (TNM) staging status and for ovarian carcinoma Federation Internationale des Gynaecologistes et Obstetristes (FIGO) classifications were followed. Detailed information is listed in Supplementary Table S2.

Mice and tumors

Wild-type (Wt) female C57BL/6, BALB/c, and Swiss albino mice (age: 4–6 weeks; average body weight: 18–22 g) were obtained from the Institutional Animal Care and Maintenance Department. Female nude mice of the Crl:NU-*Foxn1nu* strain in BALB/c (age: 4–6 weeks, average body weight: 18–22 g) were obtained from CSIR-Central Drug Research Institute (Lucknow, India). All experimental mice were housed in a pathogen free environment, fed with autoclaved dry pellets (Epic Laboratory, West Bengal Government, Kalyani, West Bengal, India), and water *ad libitum*. The experimental protocol was approved by the Institutional Animal Ethics Committee (IAEC; approval no.: IAEC-1774/RB-15/2017/2 and IAEC-1774/RB-19/2017/15). The IAEC is registered under Committee for the Purpose of Control and Supervision of Experiments on Animals (CPCSEA), Government of India.

Although 4T1 cells were maintained *in vitro*, Ehrlich carcinoma cells were maintained in the intraperitoneal passage of Swiss albino mice. To establish solid 4T1 and subcutaneous Ehrlich carcinoma breast carcinoma tumor, 4T1, and Ehrlich carcinoma cells (1×10^5)/mice were injected subcutaneously into the mammary fat pad of female BALB/c and Swiss albino mice, respectively.

To establish solid melanoma tumor, B16-F10 and B16-F1 cells (1×10^5)/mice were injected subcutaneously into the lower right flank of C57BL/6 mice. Tumor growth was in each mouse was monitored twice a week using a caliper measurement and presented as mm^2 (length × width).

Cell lines and cultures

B16-F10, B16-F1, MCF7, MDA-MB-231, and 4T1 cell lines were obtained from National Centre for Cell Sciences (NCCS, Pune, India). Cell line authentication via short tandem repeat (STR) profiling was conducted by cell repository. Cells were propagated and stored according to the provider's instructions. Cell lines were monitored regularly for ideal cell morphology and possible *Mycoplasma* contamination was eliminated using EZkill Mycoplasma Elimination Kit (Hi-Media). Cells were frozen and stored at passage two. All experiments were conducted within 7 to 10 passages after thawing them.

Figure 1.

T_{TEX} CD8$^+$ PD1$^+$ TCF1$^-$ T cell correlates positively with CSC frequency within cold TME. **A,** Schematic representation of magnetic sorting for isolation of lineage positive and negative population from breast carcinoma and ovary carcinoma biopsy samples. **B,** Representative pseudo-color flow plots for exhausted CD8$^+$ T-cell (Lin$^+$ CD8$^+$ PD1$^+$) and CSC (Lin$^-$ CD44$^+$ CD24$^-$) population in breast carcinoma biopsy samples. Scatter plots on the right represent individual frequency of respective populations with mean ± SD in all groups ($n = 28$ for breast; $n = 11$ for ovary); unpaired nonparametric *t* test. Positive corelation between exhausted CD8$^+$ T cells (Lin$^+$ CD8$^+$ PD1$^+$) and CSC (Lin$^-$ CD44$^+$ CD24$^-$/Lin$^-$ CD133$^+$ CD44$^+$ CD117$^+$) illustrated by scatter plots below, where *r* represents Pearson correlation coefficient, followed by two-tailed *P* values. **C,** Classification of advanced stage carcinomas into inflamed tumors (high CD8$^+$ T-TIL > 10%) and cold tumors (low CD8$^+$ T-TIL < 10%) as depicted by their representative IF image (CD8$^+$ TIL population – FITC tagged; magnification, ×40). **D,** Pseudo-color flow plots for tumor-infiltrated CD8$^+$ T cells, T_{PEX} Lin$^+$ CD8$^+$ PD1$^+$ TCF1$^+$, T_{TEX} Lin$^+$ CD8$^+$ PD1$^+$ TCF1$^-$ cells, and CSCs for tumor-adjacent normal, inflamed, and cold tumors in advanced carcinomas. Scatter plots represent individual percentage of respective populations with mean ± SD in all groups ($n = 16$ for breast; $n = 7$ for ovary); unpaired nonparametric *t* test. Negative correlation between CD8$^+$ TIL with T_{TEX} and positive correlation between relative percentage of T_{TEX} with percentage of CSC represented by scatter plots. *r* represents Pearson correlation coefficient, followed by two-tailed *P* values. **E,** Representative histogram plots depicting status of stem cell regulatory factors OCT4, SOX2, NANOG, KLF4, and ALDH1 within CSCs from invasive patients with breast cancer. **F,** Scatter plots on the left representing CSCs and T_{TEX} frequency across nonmetastatic and metastatic tumors. Top, patient with breast cancer data ($n = 6$ in each cohort); bottom, Ehrlich carcinoma and 4T1 murine model data ($n = 7$ in each cohort) (mean ± SD); unpaired nonparametric *t* test, followed by two-tailed *P* values. Scatter plot on the right depicts association between CSCs and T_{TEX} across metastatic and nonmetastatic cohort. *P* values were calculated from repeated measures two-way ANOVA. **B**, **D**, and **F,** *, $P < 0.05$; **, $P < 0.01$; ***, $P < 0.001$; ****, $P < 0.0001$; ns, nonsignificant.

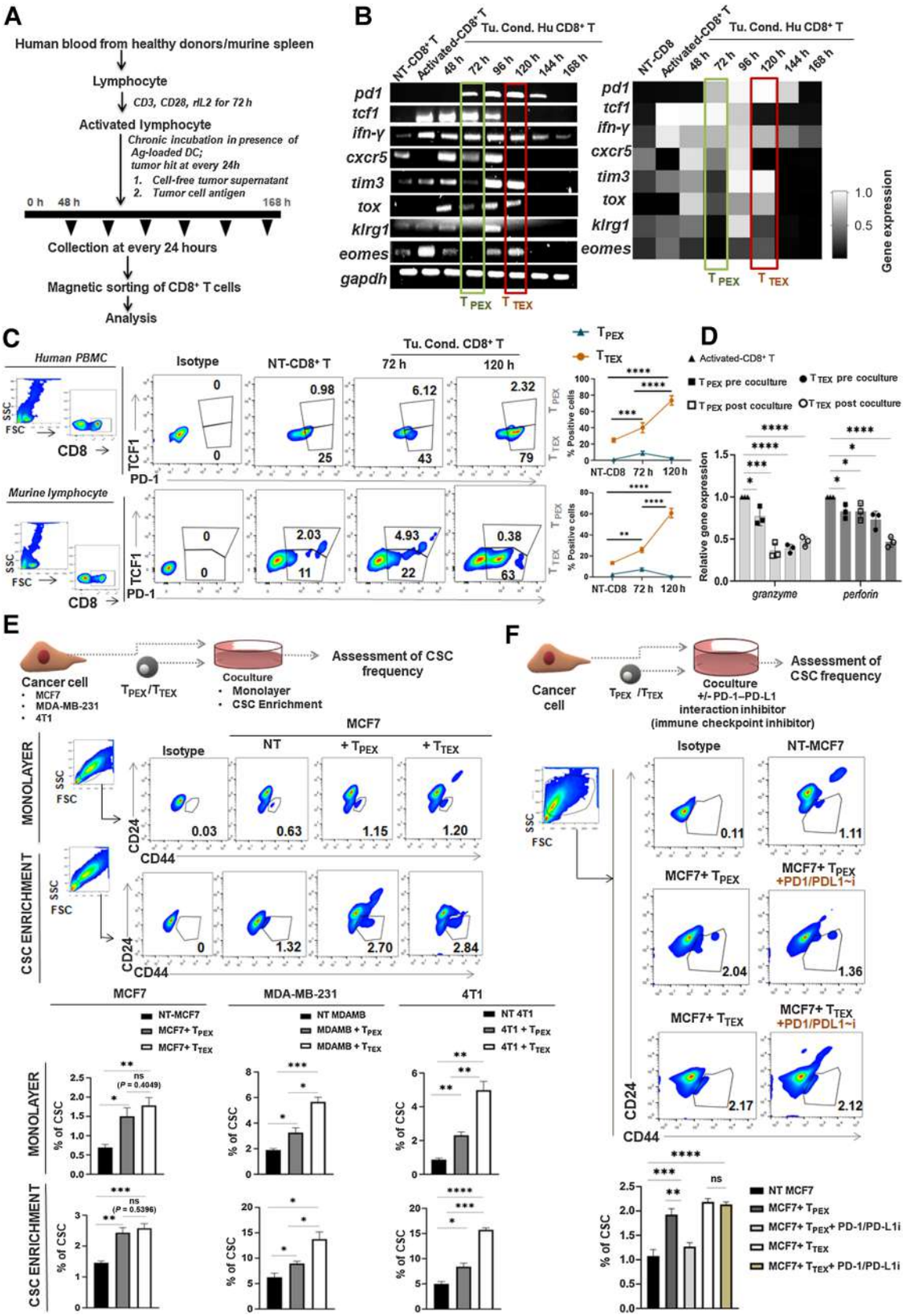

Tumor tissue processing for flow cytometry and cryosectioning

Following collagenase digestion, single-cell suspension was generated from freshly excised solid human and murine tumor specimens. Red blood cells (RBC) were eliminated using RBC lysis buffer (Hi-Media, catalog no. R075). The obtained cells were utilized in flow cytometric staining. For cryosectioning, tumor samples were rinsed in PBS, fixed in 4% paraformaldehyde (PFA) at room temperature for 2 hours and incubated in 30% sucrose solution at 4°C overnight. Finally, they were flash-frozen in liquid nitrogen and stored at −80°C until cryosectioning.

Cryosectioning

Previously prepared fixed tissue samples were embedded in an optimal cutting temperature compound (OCT compound, Leica Biosystems). These samples were sectioned (5 μm) on a Cryostat (Leica CM1950), collected on poly-L-lysine–coated slides and stored at −80°C until further use.

Histology, hematoxylin and eosin staining, and quantification

Freshly harvested tissues were rinsed with PBS and fixed in 10% formalin (in normal saline). Following dehydration, tissues were paraffin-embedded, sectioned (5 μm) using rotary microtome and stained with hematoxylin and eosin (H&E) following standard staining protocol.

Quantification of H&E-positive cells was conducted on ImageJ software as previously described (30). Briefly, acquired images were converted to 8 BIT counterparts and the threshold was adjusted only to select stained population. Binary images with watersheds were generated after the adjustments. General cell count was determined by analyzing particles from this binary image. Relative cellular count was determined by the formula: Number of HE$^+$cells/total measured area

CSC enrichment culture

Tumor cells (2×10^5) were plated on ultra-low adherent plate (Corning) and suspended into serum-free DMEM: F12K (1:1) freshly supplemented with human-rEGF (20 ng/mL), human-rbFGF (20 ng/mL), heparin (40 ng/mL), and 1% B-27 supplement (50×). The culture was fed with fresh complete media at every 3 days. Cells were incubated in a humidified atmosphere at 37°C with 5% CO_2 for 6 days. The generated tumorspheres were dissociated with mild trypsinization and centrifuged to produce single-cell suspension, available for further studies.

Preparation of tumor supernatant

Tumor supernatants were collected from media of confluent MCF7/MDA-MB-231/4T1 cultures. Media from these adherent monolayers were collected, centrifuged, and filter-sterilized prior to use.

Preparation of tumor antigen

Tumor lysate was obtained from a freshly prepared single-cell suspension of solid tumor tissue samples. Cells (2×10^7) were suspended in 1 mL PBS and subjected to 7–10 cycles of freezing (in liquid nitrogen) and thawing (37°C water bath). The generated lysate was extracted by centrifugation and filter sterilization. Protein content was determined by Bradford assay.

Generation of tumor-antigen–loaded dendritic cells

Human dendritic cells (DC) were generated from human peripheral blood mononuclear cells (PBMC) as previously described (31). Briefly, PBMC-derived monocytes were selectively made to adhere to the plastic bottom T75 flask. The adhered monocytes were cultured with GM-CSF (800 U/mL) and rIL4 (500 U/mL) in AIM-V media with 10% FBS for 7 days to differentiate into immature DCs.

Murine DCs were generated from bone marrow precursor cells as previously described (32). Bone marrow from the tibias and femurs of Swiss albino mice were flushed with PBS to generate a single-cell suspension. Erythrocytes were selectively lysed by RBC-lysis buffer (Himedia). The cells obtained were cultured in complete RPMI1640 medium with 10% FBS, supplemented with rGM-CSF (10 ng/mL), and rIL4 (5 ng/mL) for 6 days to generate immature DCs.

For maturation and tumor-antigen loading, immature DCs were incubated overnight in AIM-V media with 10% FBS with rGM-CSF (800 U/mL) and rIL4 (500 U/mL), rTNFα (5 ng/mL), rIL1β (5 ng/mL), rIL6 (150 ng/mL), and tumor antigen (5 μg/mL). Mature antigen-loaded DCs were collected by gentle tapping with an enzyme-free dissociation buffer.

Lymphocyte isolation and tumor conditioning ($T_{PEX/TEX}$ generation)

Lymphocytes were isolated from the blood (5 mL) of healthy donors via 30 minutes of density-gradient centrifugation using Lymphocyte Separating Medium (LSM; Himedia).

Lymphocytes were counted and resuspended in complete RPMI1640 media containing 0.05 mmol/L β-mercaptoethanol. Cells (2×10^6) were seeded in 2 mL media and subjected to CD3/CD28/IL2–mediated activation for 3 days. These preactivated cells were incubated with Tu-Antigen–loaded DCs (30:1 ratio) and chronically subjected to tumor conditioning for 7 days. For tumor conditioning, lymphocytes were simultaneously treated with tumor supernatant (1:25 ratio) and tumor antigen (25 μg/mL). To simulate the chronic tumor load, lymphocytes were subjected to a tumor burden at every 24 hours while being cultured in the same environment. Lymphocytes were collected every 24 hours to assess the degree of conditioning. T_{PEX} were generated after 72 hours of incubation, while T_{TEX} required 120 hours. This was monitored by sequential analysis of respective marker panel using flow cytometry and RT-PCR.

Figure 2.

Terminally exhausted CD8$^+$ T cells induce CSC upregulation; not constrained by anti–PD-1 therapy. **A,** Diagrammatic representation of *in vitro* generation of antigen specific T_{PEX} and T_{TEX} from human PBMCs and murine spleenocyte. **B,** Identification and genetic profiling of T_{PEX} and T_{TEX} pool via RT-PCR for human CD8$^+$ T cells. Quantified gene expression intensities are represented by heatmaps, with dark and light color denoting weak expression and strong expression, respectively. **C,** Representative flow plots for human and murine T_{PEX} and T_{TEX} generated at 72 hours and 120 hours, respectively. Scatter plots represent mean ± SD for T_{PEX} and T_{TEX} frequency across time points. Statistical significance was calculated by two-way ANOVA followed by Tukey multiple comparison test ($n = 6$). **D,** Bar diagrams showing functional status of human T_{PEX} and T_{TEX} both before and after coculture with cancer cell line (MCF7), keeping activated CD8 as control. Relative fold changes in *perforin* and *granzyme* expression are represented in the column (mean ± SD); alpha value was determined by one-way ANOVA followed by Tukey multiple comparison test ($n = 6$). **E,** Pseudo-color flow cytometric plots representing changes in CSC frequency in MCF7 due to T_{PEX} and T_{TEX} population. Summary bar diagrams represent CSC frequency in NT control, cancer cell with T_{PEX}, and cancer cell with T_{TEX} group across MCF7, MDAMB-231, and 4T1 cell lines (mean ± SD). Statistical significance was calculated by unpaired *t* test ($n = 6$) **F,** Flow cytometric plots displaying differential response of T_{PEX} and T_{TEX} to PD-1 blockade, in terms of CSC upregulation in MCF7 cell-line. Bar diagrams depict mean ± SD for CSC frequency across all groups. Statistical significance was calculated from one-way ANOVA followed by Tukey multiple comparison test ($n = 6$). **C**, **D**, **E**, and **F**, *, $P < 0.05$; **, $P < 0.01$; ***, $P < 0.001$; ****, $P < 0.0001$; ns, nonsignificant.

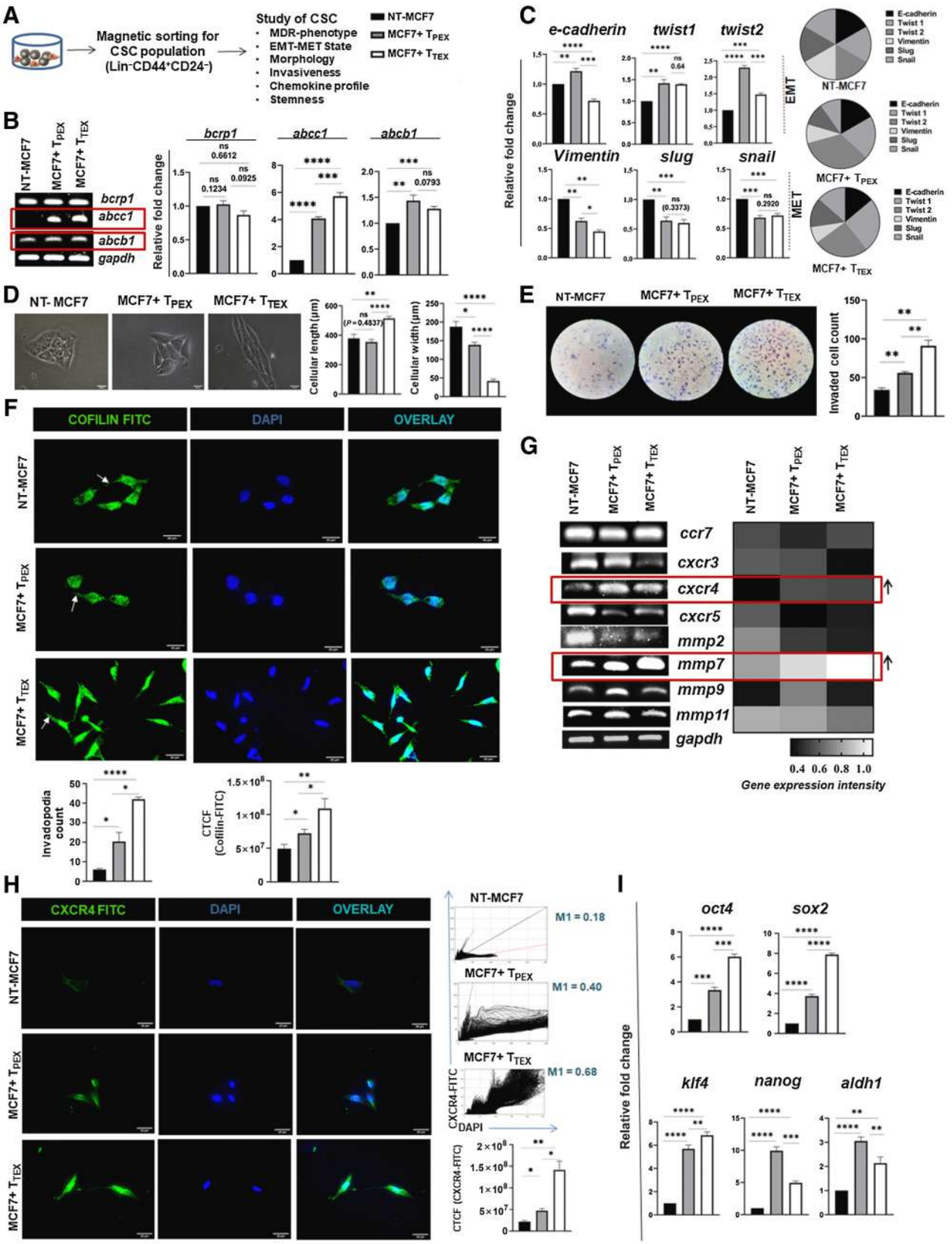

Purification of CSCs and CD8$^+$ T cells by magnetic cell sorting

Target cell suspensions were magnetically labeled with CD8/CD44/CD24/Lineage-cocktail antibodies as required. For Lin, that is, Lineage markers, following sets were used to rule out differentiated population. The human Lineage cocktail included CD2, CD3, CD11B, CD14, CD15, CD16, CD19, CD56, CD123, and CD235a. The murine Lineage cocktail included CD11b, CD3e, CD45R, TER-119, and Ly-6G/Ly-6C. Cell purification was followed according to the manufacturer's protocol (MicroBead kit). Cell purity was checked using flow cytometry.

Coculture and transwell assay

Purified exhausted CD8$^+$ T-cell subtypes were cultured in MEM and RPMI1640 complete media (1:1) with MCF7/MDA-MB-231/4T1 cells in a 5:1 ratio for 48 hours. After incubation, the T-cell suspension was removed and adherent MCF7/MDA-MB-231/4T1 population was trypsinized, centrifuged, and collected for downstream assays.

For the transwell assay, exhausted CD8$^+$ T-cell subtypes were cocultured in presence of a 0.4-μm transwell membrane (Himedia) with MCF7/MDA-MB-231/4T1 cells in a 5:1 ratio for 48 hours. After incubation period, membrane was removed and adhered cancer cells were examined further.

qRT-PCR

Total RNA was extracted using TRIzol (Ambion, Thermo Fisher Scientific) and cDNA was extracted using RevertAid First Strand cDNA Synthesis Kit (Thermo Fisher Scientific) according to manufacturer's protocol.

RT-PCR was carried out using 2x Go Taq Green Mix (Promega). PCR products were visualized and identified by image Lab softwareV5.1 on ChemiDoc XRS$^+$ (BioRad Laboratories) after 1.5% agarose gel electrophoresis and staining with ethidium bromide. Band intensity was quantified using ImageJ software.

Quantitative PCR was performed using RocheLightCycler 96 Instrument (Roche). Fold change in mRNA expression was evaluated from $2^{-\Delta\Delta C_t}$. Gene-specific PCR primers are listed in Supplementary Table S3.

Immunofluorescence, confocal microscopy, and analysis

The target samples adhered to slides were blocked in 5% BSA at room temperature. For intracellular staining, cells were perforated by 0.15% Triton X-100 prior to blocking. Sections were incubated with specific primary antibodies overnight at 4°C, then with fluorescent-tagged secondary antibodies at room temperature for 3 hours. Sections were then washed and mounted with Fluoroshield-DAPI (Abcam) and acquired with Olympus-BX53 (Olympus Lifesciences) and Leica STELLARIS 5 (confocal) microscopes (Leica Microsystems) as per required. Glycerol (Merck) was used to enhance refractive index at ×100 magnification.

Fluorescence intensity was evaluated by ImageJ software (33). The corrected total cell fluorescence (CTCF) was computed using the following formula: CTCF = Integrated density − (area of selected cell × mean fluorescence of background readings).

Sample preparation for detecting phosphorylated proteins via flow cytometry

The samples were prepared for phosphorylated-protein detection via flow cytometry as previously described (34). Briefly, experimental samples were harvested without delay and immediately fixed in 4% PFA, then incubated at room temperature for 15 minutes to preserve their phosphorylation status. Fixed cells were permeablized by adding absolute methanol drop wise to the sample while vortexing at 10 to 15 seconds at 2500 rpm at room temperature. Permeablized samples were stored at −20°C for minimum 1-hour prior to staining.

Flow cytometry

Target cells were counted and labeled with antigen specific fluorescent-tagged antibodies in the dark at 4°C for 30 minutes. For intracellular molecules, cells were simultaneously treated with a permeabilization buffer (0.2% saponin in PBS). Finally washed and fixed with 1% PFA. Data were acquired using FACSCalibur, FACSVerse, and LSRFortessa X-20 Cell Analyzer (Becton Dickinson) as required along with appropriate negative isotype controls. For data collection, Cell Quest Pro 5.1 and for data analysis FlowJo (Becton Dickinson) were used. Cellular morphology was determined via FSC-A and SSC-A. Gating strategies are provided in the respective figures.

ELISA

Antigens harvested from experimental groups were immobilized on 96-well microtiter plate, labeled with specific primary antibody overnight at 4°C, followed by horseradish peroxidase (HRP)-conjugated secondary antibody incubation. The addition of TNB substrate (BD OptEIA, BD Biosciences) resulted in a visible colorimetric output. This was measured by absorbance microplate reader Spectramax i3x (Molecular Devices) at 450 nm. SoftMax Pro 7.1 software was used for data collection.

Figure 3.

T_{TEX} cells generate aggressive CSCs, governed by OCT4-SOX2-KLF4-NANOG-ALDH1. **A,** Schematics disclosing study design for magnetic-isolation and characterization of $T_{PEX}/_{TEX}$-influenced CSCs. Inset, Black, gray, and white column denoting NT-MCF7, MCF7$^+$ T_{PEX}, and MCF7$^+$ T_{TEX} across all groups. **B,** mRNA expression of MDR-phenotype regulating genes *bcrp1*, *abbc1* and *abcb1* by RT-PCR. GAPDH was used as loading control. Quantified values are represented as relative fold changes in bar diagrams (mean ± SD). Statistical significance was assessed by unpaired *t* test ($n = 4$). **C,** EMT–MET phenotype analysis of altered CSCs by qRT-PCR. Relative fold changes are represented by summary bars (mean ± SD), with statistical significance calculated by unpaired *t* test ($n = 6$). Cumulative EMT-MET profile of CSCs from respective groups is represented by parts of whole pie chart on right. **D,** Representative micrographs of isolated CSCs from each group for assessment of morphologic features. Cellular length and width were quantified and are represented by bars (mean ± SD). Statistical significance was calculated by unpaired *t* test ($n = 6$). **E,** Representative micrographs for Matrigel invasion assay of isolated CSCs from each group. Invaded cells were quantified and are displayed as mean ± SD in the column graph. Statistical significance was calculated by unpaired *t* test ($n = 4$). **F,** Representative IF micrographs at ×100 magnification for CSCs stained with cofilin-FITC. White arrows, invadiopodias. CTCF and number of invadopodias were quantified and are displayed as column graph (mean ± SD). Statistical alpha value was calculated by unpaired *t* test ($n = 4$). **G,** mRNA expression of chemokine-associated molecules in $T_{PEX}/_{TEX}$-influenced CSCs by RT-PCR. Quantified gene expression intensities are represented by heatmap (mean ± SD) where dark color denotes weak and light color suggests strong expression respectively. Statistical significance was assessed by unpaired *t* test ($n = 4$). **H,** Representative IF micrographs at ×100 magnification for CSCs stained with CXCR4–FITC are provided. Right, cytofluoromicrographs and Mander colocalization coefficient (M1) for CXCR4 and nuclear signal colocalization. CTCF for overall CXCR4 intensity is provided in bar graph (mean ± SD; bottom). Statistical significance was calculated by unpaired *t* test ($n = 6$). **I,** $T_{PEX}/_{TEX}$-influenced CSCs were isolated and evaluated for stemness regulating genes *oct4, sox2, nanog, klf4*, and *aldh1* via qRT-PCR. Relative fold changes are represented by summary bars (mean ± SD). Statistical significance was calculated by unpaired *t* test ($n = 6$). **B**, **C**, **D**, **E**, **H**, and **I,** *, $P < 0.05$; **, $P < 0.01$; ***, $P < 0.001$; ****, $P < 0.0001$; ns, nonsignificant.

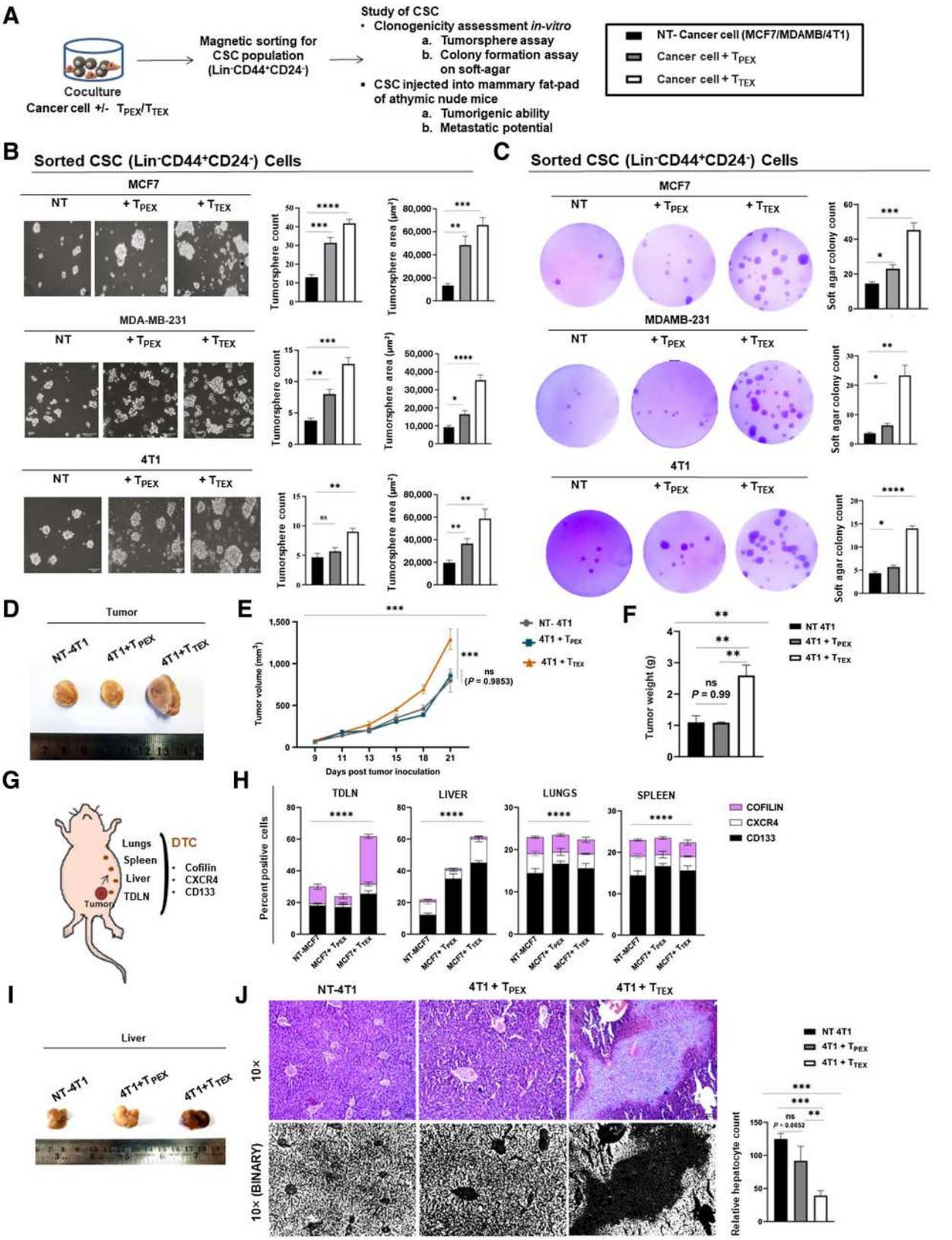

Matrigel invasion assay

After coculture, magnetically purified CSCs suspended in basal medium were layered on top of the Matrigel-coated transwell inserts (8 μm; Corning-354480). Aseptically the cell suspension containing inserts were loaded onto chemoattractant (FBS) containing 24-well plates and incubated for 22 hours. Invaded cells that adhered to the membrane were fixed in PFA, permeablized by absolute methanol and stained with 0.2% crystal violet. Migrated cells were imaged and quantified from five random fields.

The invasion index was calculated from the following formula: Percentage of invasion = % of invasion of control cells/% of invasion of test cells.

Tumorsphere assay

IMag-purified CSCs (1×10^4) from *in vitro* culture were seeded in ultra-low adherent plates in 2-mL CSC enrichment media and incubated for 7 days. The number of tumorspheres from five random spots per well was counted and micrographed. Area of tumorspheres was documented and tabulated using ImageJ software.

Colony formation assay on soft agar

Cells (5×10^3) were grown on an upper layer of soft agar (0.35% agarose) blended with cell culture medium. This layer was rested on a bottom layer consisting of 0.7% agar and cell culture medium. The culture setup was incubated for 21 days with media supplementation every 4 days. Finally, total numbers of colonies were quantified from five randomly taken micrographs/well (magnification, ×10). For envision, colonies were fixed in 2% PFA, stained with 0.04% crystal violet and 2% ethanol in PBS.

In vivo tumorigenicity assay

CSCs from T_{TEX}/T_{PEX} and cancer cell coculture were magnetically isolated. Cells (1×10^5) were inoculated into the mammary fat pad of female athymic Crl:NU-*Foxn1nu* nude mice. Tumor volume was measured as mentioned previously.

VEGFR2 neutralization *in vitro*

Cancer cells were primarily seeded to reach 70% confluency; then transferred to 2% FBS containing culture media for overnight. The next day, cells were treated with 1 nmol/L VEGFR2 inhibitor (VEGFR2 Kinase Inhibitor I, ab145888) for 24 hours.

siRNA-mediated silencing *in vivo*

siRNAs for murine VEGFR2 were primarily constructed using the Silencer R siRNA construction kit (Life Technologies) according to the manufacturer's protocol. Primers used are mentioned below. Intratumoral knockdown of VEGFR2 was conducted by intratumoral delivery of siRNA (10 μg) after combining with *in vivo*-jet PEI (1.2 μL) and 5% sucrose solution (50 μL). Delivery volume was calculated from N:P ratio according to manufacturer's protocol (35). First delivery was performed when tumor volume reached approximately 70 to 90 mm^2. Three doses of siRNAs were administered to each mouse with a 2-day interval. Mice were sacrificed 6 days after the last injection.

VEGFR2si sense: 5′AAGGCGCTGCTAGCTGTCGCTCCTGTCTC3′

VEGFR2si anti-sense: 5′AAGCGACAGCTAGCAGCGCCTCCT-GTCTC3′

siRNA-mediated silencing *in vitro*

siRNA for human-LAMP3 and human-NRP1 were constructed *in vitro* using the Silencer R siRNA construction kit (Life Technologies) according to the manufacturer's protocol. Primers utilized are mentioned below. The target-specific siRNA and scramble control siRNA (Sigma-Aldrich) were added to *in vitro* setup to a final concentration of 50 nmol/L to the 2-hour serum-starved cells in presence of Lipofectamine 2000 reagent (Invitrogen).

LAMP3si sense: 5′-AAGGTTGAGAATAATCTCTGGCCTGTC-TC-3′

LAMP3si anti-sense: 5′-AACCAGAGATTATTCTCAACCCCT-GTCTC-3′

NRP1si sense: 5′-AACCGGAGCCTCAATCAGCCACCTGTCTC-3′

NRP1si anti-sense: 5′-AATGGCTGATTCAGGCTCCGGCCTG-TCTC-3′

Statistical analysis

To ensure adequate power, all results represent the mean ± SD of data obtained from either one ($n = 6/7$ for *in vivo*) or three to six (for *in vitro*) independent experimental arms. All patients' samples ($n = 45$) were randomized prior to group allocation. Therefore, the data distribution was presumed to be normal with similar variances.

Statistical significance was established from unpaired Student *t* test (for two groups) or one-way/two-way ANOVA. Positive and/or negative correlation was deduced from Pearson correlation coefficient. All statistical analyses and heatmaps were generated by GraphpadPrism 8.4.2 software (GraphPad Software). The number of *in vitro* or *in vivo* experiments used for each analyses and particular statistical test used are indicated in each figure legend. Experimental groups attaining a $P \le 0.05$ were considered as significant.

Figure 4.

T_{TEX}-influenced CSCs are highly clonogenic, causeing hepatic metastasis. **A,** Diagrammatic representation of workflow to assess tumorigenic and metastatic potentiality of altered-CSCs. **B,** *In vitro*, CSCs magnetically sorted post coculture and plated for tumorsphere assay. Representative images for all three groups in MCF7, MDA-MB-231, and 4T1 cell line cocultures are provided. In bar graph, mean ± SD for tumorsphere count and size is indicated. Statistical significance is inferred from unpaired *t* test ($n = 6$). **C,** *In vitro*, post coculture–sorted CSCs were plated for colony-forming assay on soft agar. Representative photographs for developed colonies in each group for three cell lines are provided. Number of colonies (mean ± SD) is displayed by column bars. Statistical significance is calculated from unpaired *t* test ($n = 4$). **D,** *In vivo*, CSCs isolated from 4T1 ± T_{PEX}/T_{TEX} coculture was subcutaneously injected into mammary fat pad of athymic nude mice for development of tumor. Representative photographs of harvested tumors are presented ($n = 6$ mice per group). **E,** Tumor growth curve representing tumor volume, keeping mean ± SD at each time point per group. Statistical significance was calculated by two-way ANOVA ($n = 6$ mice per group). **F,** Difference in tumor weight (in grams) in three groups represented by column bar (mean ± SD). Statistical significance drawn from unpaired *t* test ($n = 6$ mice per group). **G,** Schematic diagram displaying possible spread sites for DTCs. DTCs were evaluated on the basis of their expression of CD133, CXCR4, and cofilin. **H,** Summary bars displaying DTC accumulation across TDLN, liver, lungs, and spleen and their relative expression of CD133, CXCR4, and cofilin (mean ± SD). Statistical significance was calculated by two-way ANOVA ($n = 6$ mice per group). **I,** Representative photograph of metastatic spread in harvested and formalin-fixed liver tissue across all groups ($n = 6$ mice per group). **J,** Representative micrographs of H&E-stained liver tissue and their binary front at ×10 magnification across all groups ($n = 6$ mice per group). Column bars represent relative hepatocyte count (number of hepatocytes/total area), mean ± SD, nonparametric unpaired *t* test ($n = 6$ mice per group). **B**, **C**, **E**, **F**, **H**, and **J,** *, $P < 0.05$; **, $P < 0.01$; ***, $P < 0.001$; ****, $P < 0.0001$; ns, nonsignificant.

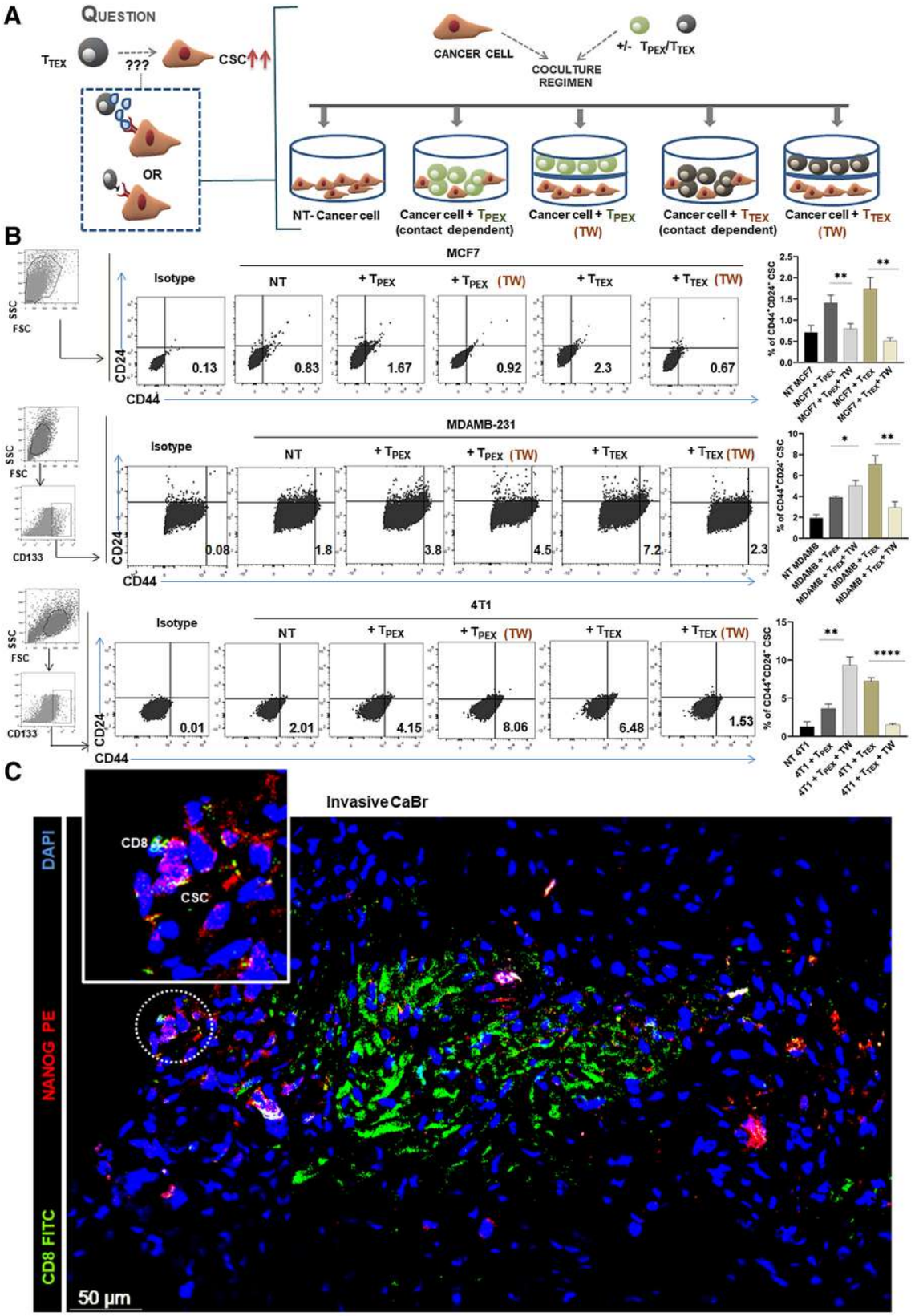

Data availability

Data supporting this study are available from the corresponding author upon reasonable request.

Results

T_{TEX} cells positively correlate with elevated CSC frequency within TME

Clinical responses to anti–PD-1 therapy in patients with breast and ovarian cancer have been insufficient with longer complete response rates and shorter duration. Therefore, a better understanding of intratumoral CD8$^+$ T-cell composition and analyzing their exhausted semifunctional states would benefit future of immunotherapies.

So, to primarily investigate the influence of CD8$^+$ T-cell exhaustion on the CSCs of these solid TME, pretreatment tumor biopsies of breast ($n = 28$) and ovarian ($n = 11$) origin were screened for exhausted CD8$^+$ T (*Lin*$^+$ *CD8*$^+$ *PD1*$^+$) cells and CSCs (*Lin*$^-$ *CD44*$^+$ *CD24*$^-$ in breast and *Lin*$^-$ *CD44*$^+$ *CD133* $^+$*CD117*$^+$ in ovary; **Fig. 1A**). It was found that advanced stage carcinomas (invasive ductal breast carcinoma and stage IIIovarian carcinoma) were enriched for both exhausted CD8$^+$ T cells and CSCs in comparison with tumor-adjacent normal and early-stage carcinoma (*in situ* breast carcinoma and stage I ovarian carcinoma) tissues. Furthermore, a strong positive correlation between exhausted CD8$^+$ T cells and CSCs was noted across breast ($r = 0.8955$) and ovarian ($r = 0.9284$) carcinoma biopsies (**Fig. 1B**).

Further studies were centralized on the advanced breast ($n = 16$) and ovarian carcinomas ($n = 7$) only. They were screened for progenitor exhausted (T_{PEX}; *Lin*$^+$ *CD8*$^+$ *PD1*$^+$ *TCF1*$^+$) and T_{TEX} (*Lin*$^+$ *CD8*$^+$ *PD1*$^+$ *TCF1*$^-$) populations. It was revealed that both exhausted CD8$^+$ T-cell subsets- T_{PEX} and T_{TEX} do exist within tumor-infiltrated CD8$^+$ T-cell pool. Surprisingly, T_{TEX} followed a negative correlation with infiltrated CD8$^+$ T-cell frequency ($r = -0.8837$ in breast carcinoma and $r = -0.9402$ in ovarian carcinoma). To understand the implication of this phenomena, we further subcategorized the advanced carcinomas into inflamed tumors (high CD8$^+$ T-TIL > 10%) and cold tumors (low CD8$^+$ T-TIL < 10%) according to International Guidelines on TIL assessment (TIL frequency < 10% considered as cold or poor-immune infiltrated tumor; **Fig. 1C**; Supplementary Fig. S1A; refs. 36–39). This classification revealed that T_{TEX} and CSC frequencies were more strongly elevated in cold tumors than in inflamed tumors. In addition, the relative T_{TEX} frequency (over T_{PEX}) positively correlated with the CSC population ($r = 0.9077$ in the breast, $r = 0.8809$ in the ovary), indicating a possible CSC-uprising role of T_{TEX} in cold tumors (**Fig. 1D**).

Next, to delineate the functional status of CSCs belonging to both cold and inflamed tumors, several CSC-fate regulatory molecules were analyzed via flow cytometry. It was revealed that in cold tumor (T_{TEX} high) CSCs had overexpression of OCT4, KLF4, NANOG, and ALDH1 compared with inflamed tumor (T_{TEX} low) cohort, while SOX2 expression remained borderline elevated (**Fig. 1E**). These data suggests that in cold-tumors enriched with T_{TEX} population, CSCs remain in an aggravated form.

Because mutual association between T_{TEX} and CSCs indicated toward disease advancement, we wanted to discern whether they have any role in metastasis. Therefore, patients with breast carcinoma with reported history of metastasis (primarily lymph node metastasis) were screened. It was observed that both T_{TEX} and CSCs remained thoroughly enriched in metastatic cohort ($n = 6$), unlike the nonmetastatic cohort ($n = 6$). To further validate, these two populations were studied in nonmetastatic murine breast carcinoma model-Ehrlich carcinoma ($n = 6$) and metastatic murine breast carcinoma model-4T1 ($n = 6$). In-line with our data from patient samples, it was observed that murine metastatic tumor (4T1) exhibited higher frequency of T_{TEX} and CSCs (Lin$^-$ CD44$^+$ CD24$^-$ CD133$^+$) compared with nonmetastatic tumor (Ehrlich carcinoma; **Fig. 1F**). In addition, metastatic murine melanoma tumor-B16F10 ($n = 7$) showed similar results, higher CSCs (Lin$^-$ CD44$^+$ CD133$^+$ CD34 $^+$Nanog$^+$), and T_{TEX} accumulation in contrast to nonmetastatic B16F1 melanoma tumor ($n = 7$; Supplementary Fig. S1B).

T_{TEX} induces CSC upregulation, nonremediable by anti–PD-1 therapy

Given the positive correlation between T_{TEX} cells and CSCs and their possible involvement in tumor advancement, their direct interplay was further investigated *in vitro*. Initially, T_{PEX} and T_{TEX} populations were generated from human PBMCs and murine splenocytes *in vitro* (**Fig. 2A**). Although both T_{PEX} and T_{TEX} were found to be enriched for exhaustion signature, they showed separate and distinct gene expression profiles. T_{PEX} displayed PD1$^+$ TIM3$^-$ TCF1$^+$ CXCR5^{low} IFNγ^{low} TOX^{low} KLRG1$^-$ Eomes$^-$ phenotype, while T_{TEX} retained PD1$^+$ TIM3$^+$ TCF1$^-$ CXCR5$^-$ IFNγ^{low} TOX^{high} KLRG1$^-$ Eomes$^+$ phenotype (**Fig. 2B** and **C**). Functionally both T_{TEX} and T_{PEX} exhibited lower expression of *perforin*, *granzyme-B* in comparison with activated CD8$^+$ T cells, attributing to their exhausted state (**Fig. 2D**). Next, these T_{PEX} and T_{TEX} cells were cocultured with MCF7, MDA-MB-231, and 4T1 cells for 48 hours. A significant surge in CSC percentage was noted in presence of T_{TEX} with respect to untreated control. This CSC elevation was observed in all three cancer cell lines propagated on both monolayer and 3D-CSC enrichment setting. Surprisingly, T_{PEX} -induced CSC elevation was also prominent (**Fig. 2E**). However, this exhausted CD8$^+$ T-cell–induced CSC upregulation was markedly absent in presence of polyclonally activated (CD3, CD28, and rIL2) CD8$^+$ T cells (Supplementary Fig. S2A).

Next, we investigated whether T_{PEX}- and T_{TEX}-induced CSC uprising can be reverted by anti–PD-1 therapy. So, coculture was conducted in the presence and absence of a PD-1–PD-L1 interaction inhibitor [PD-1/PD-L1 inhibitor 1, small-molecule inhibitor (ab230369, ICI agent)]. A differential response of T_{TEX} and T_{PEX} to anti–PD-1 therapy was found. Although anti–PD-1 therapy administration significantly brought down CSC frequency in the T_{PEX} cohort, CSC population was maintained in a static elevated state in the T_{TEX} group (**Fig. 2F**). Furthermore, investigation of one of the most fundamental characteristics of CSCs, that is, their tumorigenic potential through tumorsphere assay disclosed that administration of ICI agent did no significant

Figure 5.

T_{TEX} cells upregulate CSCs by receptor-ligand interaction. **A,** Illustrative representation for probable scenarios of CD8$^+$ $T_{PEX}/_{TEX}$-mediated CSC elevation. **B,** Flow cytometric dot plots for CSC frequency in coculture setups with and without transwell membrane, keeping cancer cell with no treatment as control. Representative plots for MCF7, MDA-MB-231, and 4T1 cell lines are displayed, respectively. Right, summary bar graphs, presenting mean ± SD for CSC frequencies in respective groups. Statistical significance was calculated from unpaired *t* test ($n = 4$). **C,** Representative IF micrographs of human advanced breast carcinoma tumor tissue at ×20 magnification for CSCs (stained with nanog-PE) and infiltrated CD8$^+$ T cells (FITC). Their close proximity is enlarged in inset. Scale bar, 50 μm. **B,** *, $P < 0.05$; **, $P < 0.01$; ****, $P < 0.0001$.

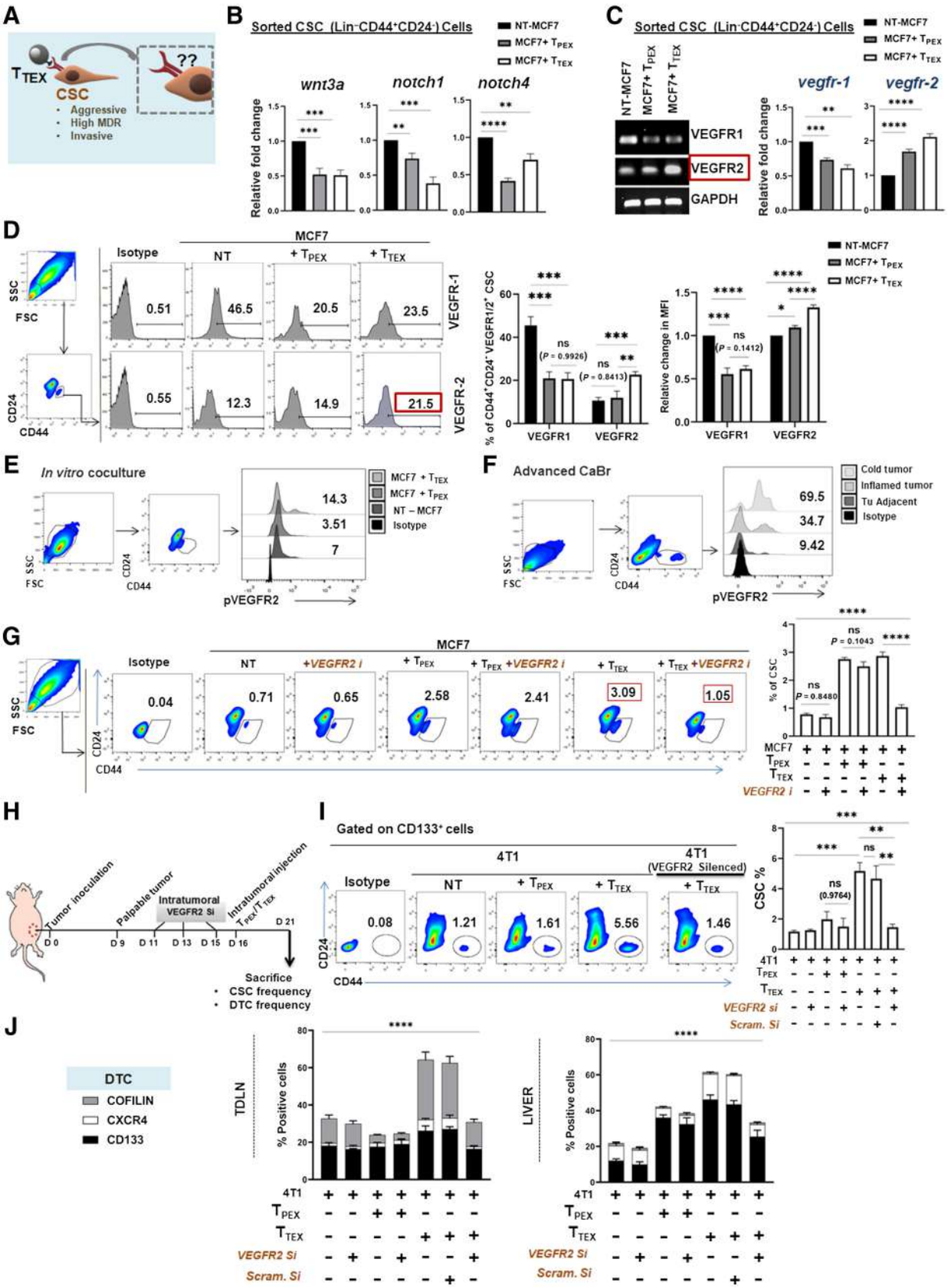

downregulation of this property in CSCs of T_{TEX}-treated group. Meanwhile T_{PEX} -induced CSCs remained highly responsive to PD-1–PD-L1 inhibition, exhibiting a lesser tumorsphere formation (Supplementary Fig. S2B). Similar fate was also noted in expression of stem-cell governing transcription factor NANOG within CSCs (Supplementary Fig. S2C).

T_{TEX}-influenced CSCs are aggressive, resistant, and invasive, overseen by OCT4-SOX2-KLF4-NANOG

Deciphering specific hallmarks of T_{TEX}-CSCs are crucial to determine their impact on overall tumor progression. For this, CSCs were primarily isolated post coculture, and undertaken for analysis of some of its major attributes and regulatory transcription factors (**Fig. 3A**).

RT-PCR analysis of MDR-phenotype regulating genes revealed an upsurge in *abcc1* and *abcb1* in T_{TEX}-influenced CSCs (**Fig. 3B**). Analyses of EMT-associated gene expression profile have unexpectedly revealed that T_{TEX}-influenced CSCs remain in transitory phase between epithelial and mesenchymal lineages. They simultaneously coexpress mesenchymal state with elevated *twist1*, *twist2*, and low *e-cadherin* expressions; and epithelial state with low *vimentin*, *slug*, and *snail* expressions. Notably, T_{PEX} influenced CSCs skew toward the mesenchymal state, expressing elevated *e-cadherin* (**Fig. 3C**).

Phase-contrast microscopy revealed that T_{TEX}-influenced CSCs uptake a very linear invasive morphology with increment in cellular length and reduction in cellular width (**Fig. 3D**). Matrigel invasion assay disclosed strong invasive vigor in T_{TEX}-influenced CSCs (**Fig. 3E**). To ascertain how the cytoskeleton is aiding in this invasion, an actin-binding cytoskeletal protein cofilin was analyzed. Immunofluorescence (IF) imaging for cofilin revealed its variance in subcellular distribution; showcasing increased nuclear expression within T_{TEX}-CSCs. In addition, it revealed cytosolic and nuclear elongation, supporting development of invadopodias in T_{TEX}-CSCs (**Fig. 3F**).

To predict probable migratory sites, gene expression status of chemotaxis associated molecules was screened by RT-PCR. Elevation in CXCR4 and matrix metalloproteinase 7 (MMP7) was observed (**Fig. 3G**), indicating the possibility of metastasis in lungs, liver, bone, brain, kidney, and lymph node. Further study of subcellular distribution of CXCR4 by IF imaging revealed a strong nuclear localization of CXCR4 within T_{TEX}-CSCs (Mander colocalization coefficient; M1 = 0.68). Overall, cellular CXCR4 intensity was also strongly elevated in T_{TEX} -CSCs (**Fig. 3H**).

CSC-attributable regulatory transcription factors *oct4, sox2, klf4*, and *nanog* were upregulated in presence of T_{TEX} as evident from qRT-PCR. Moreover, *aldh1*, regulator of stem cell metabolism, was also overexpressed in T_{TEX}-CSCs (**Fig. 3I**).

T_{TEX}-influenced CSCs are highly clonogenic and metastasize in the liver by disseminating through TDLN

Tumorigenicity, the key attribute of CSCs, was evaluated next. CSCs were magnetically isolated post coculture, plated into *in vitro* 7-day tumorsphere assay and 21-day colony formation assay on soft agar (**Fig. 4A**). T_{TEX}-influenced CSCs showed increased sphere and colony formation compared with untreated CSCs or T_{PEX}-influenced CSCs (**Fig. 4B** and **C**).

For *in vivo* study, CSCs (1×10^4) were isolated from 4T1- T_{PEX} /T_{TEX} *in vitro* coculture and inoculated into the mammary fat pad of Crl:NU-*Foxn1nu* athymic nude mice for tumor development. A significant upsurge in tumor growth and weight was noted in presence of T_{TEX}-influenced CSCs, compared with untreated control CSCs or T_{PEX}-influenced CSCs (**Fig. 4D–F**).

Because, T_{TEX}-influenced CSCs exhibited migratory and invasive phenotypes, we examined disseminated tumor cells (DTC) in the migratory sites – tumor draining lymph node (TDLN), liver, lungs, and spleen; on the basis of their chemokine expression pattern. DTCs were evaluated on the basis of their expression of CD133, CXCR4, and cofilin—markers that remained thoroughly upregulated in T_{TEX}-influenced CSCs. Flow cytometric analysis revealed a heavy infiltration of DTCs in the TDLN of T_{TEX}-CSC cohort; exhibiting upsurge in CD133, CXCR4, and cofilin. Among the distant metastatic sites, accumulations of CD133$^+$ CXCR4$^+$ DTCs were noted in the liver. In contrast, the lungs and spleen showed no significant assembly. Cofilin expression within DTCs remained unaltered at all distant metastatic sites (Supplementary Fig. S3A–S3E). Cumulatively, highest migratory DTCs were congregated in TDLN and liver of T_{TEX} -CSC cohort (**Fig. 4G** and **H**).

Moreover, within 25 days of tumor inoculation, liver metastasis was found in mice inoculated with T_{TEX}-CSCs. The liver parenchyma was heavily disrupted. It was fibrous and necrotic, observed from both macroscopic imaging and H&E staining (**Fig. 4I** and **J**). In addition, a significant decline in the relative hepatocyte count (hepatocyte count/total area) was noted in T_{TEX}-CSCs treated group (**Fig. 4J**).

T_{TEX} influences CSC population in a contact-dependent manner

Given the prominence of T_{TEX} in upregulating CSCs, we sought to determine whether T_{TEX} requires cell-to-cell receptor-ligand contact or can act independently. Coculture assays were performed in two different setups to distinguish as such (**Fig. 5A**). In one setup, $T_{PEX/TEX}$ and cancer cells were physically separated using a 0.4-μm transwell membrane, so that target population can only communicate via cellular-secretions (contact-independent). Although, in another, both the cells were cultured in same well, to initiate receptor–ligand interaction (contact dependent). After 48 hours of

Figure 6.

T_{TEX} influences CSC aggressiveness by stimulating VEGFR2 on CSC surface. **A,** Schematic representation of the study question; identification of the involved receptor on CSC surface. **B,** Analyzing the status of CSC fate–regulating cell-surface receptors within CSC-population via q-RT PCR. Relative fold changes in gene expression across all groups are displayed via bar graphs (mean ± SD); unpaired *t* test ($n = 5$). **C,** Status of *vegfr1* and *vegfr2* within CSC population across all groups via RT-PCR. Relative fold changes in gene expression are displayed via bar-graphs (mean ± SD); unpaired *t* test ($n = 5$). **D,** Vegfr1 and Vegfr2 protein expression in CSC population via flow cytometry. Percentage of CD44$^+$ CD24$^-$ VEGFR1$^+$/R2$^+$ population and relative change of MFI of VEGFR1 and VEGFR2 within CD44$^+$ CD24$^-$ CSC pool is represented by bar graphs (mean ± SD); two-way ANOVA followed by Tukey multiple comparison test ($n = 4$). **E,** Representative histogram plots exhibiting pVEGFR2 status within CSCs of all *in vitro* experimental coculture cohorts ($n = 4$). Left, gating strategies. **F,** Representative histogram plots exhibiting pVEGFR2 status within CSCs of patients with advanced carcinoma ($n = 6$ in each group). Left, gating strategies. **G,** Representative flow cytometric plots for MCF7 and T_{PEX}/T_{TEX} coculture in presence and absence of 1 nmol/L small-molecule VEGFR2 inhibitor (VEGFR2 kinase inhibitor I, ab145888; VEGFR2i). CSC frequency is displayed in the column graph (mean ± SD); one-way ANOVA followed by Tukey multiple comparison test ($n = 5$). **H,** Schematic diagram explaining the experimental design for *in vivo* VEGFR2 knockdown in 4T1 tumor–bearing mice and subsequent T_{PEX}/T_{TEX} administration. **I,** Representative pseudo-color flow cytometric plots for NT-4T1, 4T1-T_{PEX}, 4T1-T_{TEX}, and 4T1 (VEGFR2 Si)-T_{TEX} groups showcasing CSC frequency. Right, column bars displaying CSC frequency across all experimental groups (mean ± SD); one-way ANOVA followed by Tukey multiple comparison test ($n = 6$ mice per group). **J,** Summary bars disclosing DTC frequency across TDLN and liver for all experimental groups (mean ± SD); two-way ANOVA followed by Tukey multiple comparison test ($n = 6$ mice per group). **B**, **C**, **D**, **G**, **I**, and **J,** *, $P < 0.05$; **, $P < 0.01$; ***, $P < 0.001$; ****, $P < 0.0001$; ns, nonsignificant.

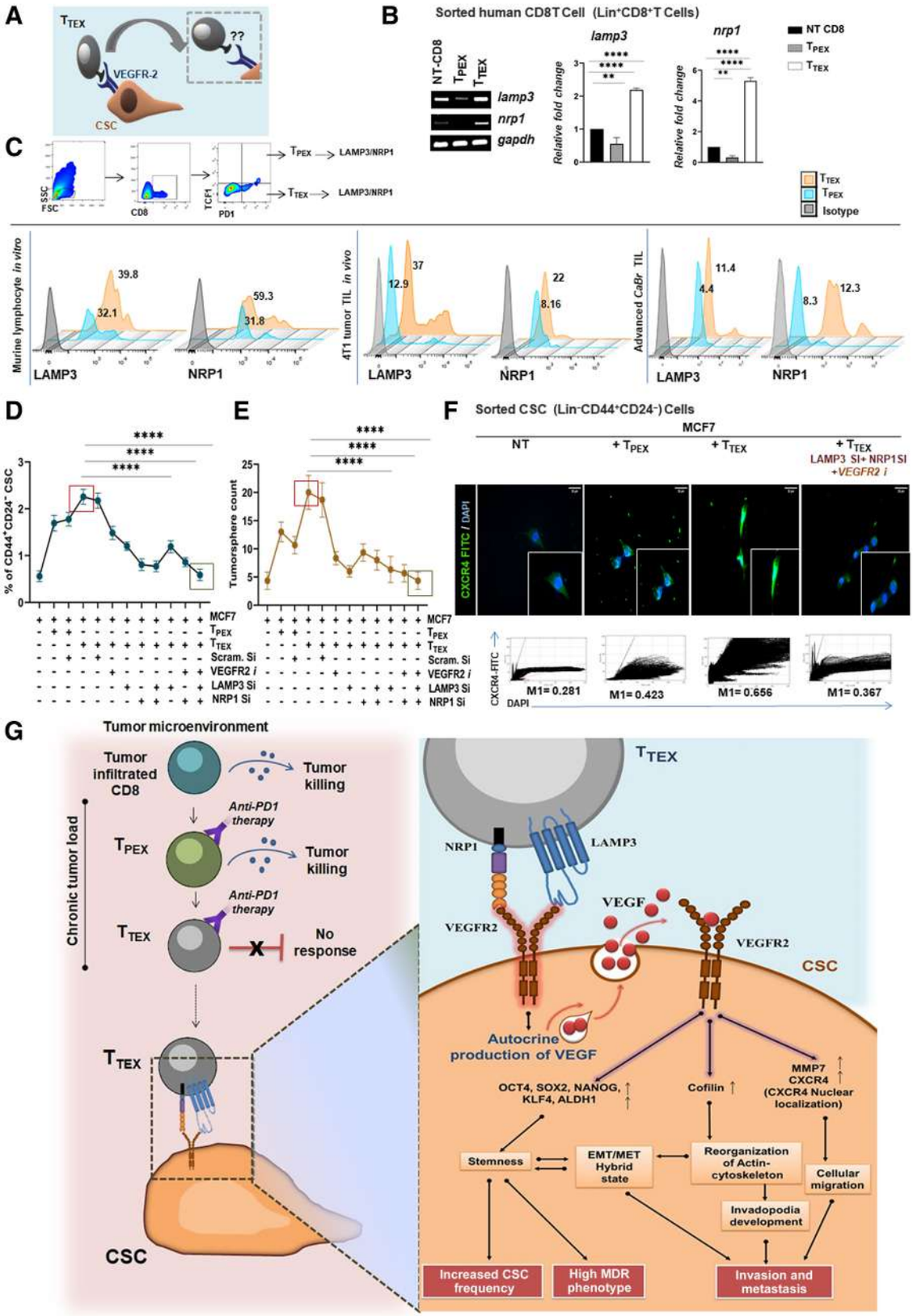

coculture, T_{TEX}-induced CSC hike was only evident in contact-dependent setup across all cell lines, indicating an absolute necessity for receptor–ligand interaction. However, it was interesting to note that T_{PEX}-induced CSC elevation was very much dependent on secretory factors particularly in case of aggressive triple-negative breast cancer (TNBC) cell lines (MDA-MB-231 and 4T1). In contrast no such dependency was noted in less aggressive luminal-A (MCF7; **Fig. 5B**).

To further validate that T_{TEX}-induced CSC upregulation is not cytokine mediated, we evaluated cytokines present in the coculture supernatant (Supplementary Fig. S4A). Using ELISA, we evaluated a panel of secreted cytokines: IL2, IL4, IL5, IL6, IL10, IL12, IL13, IFNγ, TGFβ, and TNFα, keeping untreated-T_{PEX},-T_{TEX}, and untreated cancer cells as controls. It was observed that all the examined cytokines were at the lowest at T_{TEX}-treated cohort. However, T_{PEX} addition increased IL10 production particularly in aggressive TNBC (MDA-MB-231 and 4T1 cohort), which ties to our previous observation as well. These data suggest that T_{TEX}-mediated CSC upregulation does not invoke activity of said cytokines; rather it involves a contact-dependent pathway (Supplementary Fig. S4B).

Simultaneously human advanced breast carcinoma tumor tissues were explored for colocalization of T_{TEX} and CSCs to validate the possibility of their contact-dependent interaction. Confocal microscopy revealed that within solid TME, CSCs and infiltrated CD8$^+$ T cells do remain in a very close proximity, thus suggesting the likelihood of their receptor–ligand–mediated interaction (**Fig. 5C**).

T_{TEX} triggers VEGFR2 on the CSC surface to initiate CSC aggression

Because previous results direct toward a physical contact-dependent CSC upregulation for T_{TEX}, we screened the CSCs for such receptor–ligand–based signaling pathways governing CSC fate (**Fig. 6A**). Meanwhile pathways that are activated through secretory factors like JAK-STAT, PI3-AKT-mTOR, and NF- κB pathways were not considered. Our qRT-PCR analysis of *wnt3a*, *notch1*, *notch4* out ruled involvement of these pathways (**Fig. 6B**). Consequently, other possible avenues were explored. On the basis of several reports on the VEGF-mediated upregulation of the OCT4–SOX2–NANOG pathway and CXCR4, MMP7-induced metastasis; we looked into the VEGF receptor status on isolated CSC surface. In both protein and mRNA levels a significant upregulation in VEGFR2, but not VEGFR1, was noted selectively within T_{TEX}-influenced CSCs compared with T_{PEX}-influenced CSCs (**Fig. 6C** and **D**; Supplementary Fig. S5A). Although MFI of VEGFR2 on T_{PEX}-CSCs was borderline elevated, it still remained significantly lower than T_{TEX}-CSCs (**Fig. 6D**). Moreover, phosphorylation status of VEGFR2 on CSC surface remained thoroughly upregulated in T_{TEX}-influenced cohort, compared with other two groups as evident in both *in vitro* coculture setup and in patients with advanced breast carcinoma (**Fig. 6E** and **F**).

Interestingly, when we crosschecked, these VEGFR2 was not being stimulated by T_{TEX}-secreted VEGFs, as VEGF-mRNA in T_{TEX} remained unaltered (Supplementary Fig. S5B). However, the total secretory VEGF remained elevated in the T_{TEX} coculture supernatant (Supplementary Fig. S5C). Cumulatively, these observations suggest the involvement of T_{TEX}-mediated contact-dependent activation of VEGFR2 on CSC surface, which activates autocrine VEGF feedback loop within them.

Next to confirm this conjecture, VEGFR2 was selectively neutralized *in vitro* within MCF7 cell line via a selective VEGFR2-inhibitor (VEGFR2*i*; VEGFR2 kinase inhibitor I, ab145888; *in vitro* VEGFR2 neutralization frequency; Supplementary Fig. S5D) and cocultured. Flow cytometry revealed that the VEGFR2 inhibitor treatment significantly lowered the CSC frequency in the T_{TEX}-influenced group, however VEGFR2-neutralization on the T_{PEX} group yielded no significant alterations (**Fig. 6G**). This was also reflected in the tumorsphere forming capacity of the T_{TEX}-influenced CSCs, where VEGFR2 inhibition yielded less tumorsphere formation (Supplementary Fig. S5E).

To further validate the results, VEGFR2 was knocked down *in vivo* within 4T1-tumor using target-specific VEGFR2-siRNA (*in vivo* VEGFR2 neutralization frequency; Supplementary Fig. S5F). Following the last dose of intratumoral-siRNA challenge, antigen-specific *in vitro* generated T_{PEX} and T_{TEX} were delivered within tumor. CSC and DTC frequency were evaluated 6 days postinjection of T_{PEX} and T_{TEX} (**Fig. 6H**). In-line with *in vitro* neutralization, *in vivo* observation revealed a significant downregulation of the CSC frequency within the VEGFR2-neutralized tumor, despite addition of the T_{TEX} (**Fig. 6I**). Moreover, overinfiltration of DTCs (CD133$^+$ CXCR4$^+$ Cofilin$^+$) within TDLN and liver of T_{TEX}-influenced group was markedly lowered in the VEGFR2-neutralized tumor (**Fig. 6J**). *In vivo* neutralization of VEGFR2 exhibited no significant changes in the T_{PEX} group for both CSC and DTC frequencies (**Fig. 6I** and **J**).

T_{TEX}-influenced CSC aggressiveness is regulated by the LAMP3/NRP1–VEGFR2 cascade

Because cell surface ligands of VEGFR2 present on the T_{TEX} surface were responsible for triggering this entire phenomenon, respective trans-ligands on CSC surface were explored (**Fig. 7A**). Previous reports have indicated existence of three such ligands, namely, LAMP3, NRP1, and SYNDECAN-1 (40). However, as SYNDECAN-1 is not expressed in murine-splenocyte CD8$^+$ T cells and is intracellularly expressed in human-PBMCs (41), their possible involvement was negated. Analysis of LAMP3 and NRP1 in *in vitro* generated human T_{TEX} cells showed their overexpression compared with T_{PEX} cells (**Fig. 7B**). Similar trend was also noted in murine-T_{TEX} (*in vitro*), 4T1-tumor TIL-T_{TEX}, and in TIL-T_{TEX} cells in patients with advanced breast carcinoma (**Fig. 7C**).

To validate our observation, we silenced *lamp3* and *nrp1* via target-specific siRNA on T_{TEX} (*lamp3* and *nrp1* silencing frequency;

Figure 7.

T_{TEX} influences CSC aggressiveness through LAMP3/NRP1–VEGFR2 cascade. **A,** Schematic representation of the study question; identification of the ligand on T_{TEX} cell surface. **B,** Studying mRNA expression of VEGFR2 ligands on T_{TEX} surface via RT-PCR. Relative fold changes in gene expression displayed by bar graphs (mean ± SD); one-way ANOVA followed by Tukey multiple comparison test ($n = 5$). **C,** Representative histograms displayed in staggered plot exhibiting expression of LAMP3 and NRP1 in *in vitro*–generated murine T_{TEX}, 4T1 tumor–derived T_{TEX}, and human breast carcinoma–derived T_{TEX}, respectively. Top, gating strategy. **D,** Scatterplot displaying frequency of CD44$^+$ CD24$^-$ population after siRNA silencing of *lamp3* and *nrp1* in T_{TEX} population, followed by coculture with ± VEGFR2-neutralized MCF7. Each dot plot represents mean ± SD of respective cohorts; one-way ANOVA followed by Tukey multiple comparison test ($n = 3$). **E,** Frequency of tumorsphere formation from CSCs isolated from previous siRNA treatment coculture (**D**). Each dot plot represents mean ± SD of each cohort; one-way ANOVA followed by Tukey multiple comparison test ($n = 3$). **F,** Representative IF micrographs of CXCR4 expression within CSC population in NT-MCF7, MCF7 + T_{PEX}/T_{TEX}, and MCF7 (VEGFR2-neutralized) + T_{TEX} (*lamp3* and *nrp1*siRNA silenced) group; magnification, ×100. Bottom, cytofluromicrographs and Mander colocalization coefficient (M1) for respective population. **G,** Summary picture describing T_{TEX}-mediated CSC aggression through LAMP3/NRP1–VEGFR2 cascade. **, $P < 0.01$; ****, $P < 0.0001$.

Supplementary Fig. S6A and S6B). Coculturing was conducted using silenced and nonsilenced T_{TEX} with MCF7 cells in the presence or absence of VEGFR2*i*. The flow cytometric analysis disclosed that CSC frequency was significantly lowered by individual siRNA-silencing of both *lamp3* and *nrp1* in T_{TEX}. However, CSC frequency was normalized, where T_{TEX} was concomitantly silenced for both *lamp3* and *nrp1* in conjunction with VEGFR2-neutralized MCF7 (**Fig. 7D**). The tumorsphere count also followed the same pattern (**Fig. 7E**). Nuclear localization of CXCR4 in T_{TEX}-CSCs (Mander colocalization M1 = 0.656), were found to be relocalized back to cytoplasm in *lamp3*Si+ *nrp1*Si+ VEGFR2*i*group (Mander colocalization M1 = 0.367). In addition, a decline in overall CXCR4 intensity, normalization of elongated cytosols and nuclei was also noted (**Fig. 7F**). Cumulatively, our finding validates the involvement of LAMP3/NRP1–VEGFR2 axis in triggering T_{TEX}-mediated CSC upregulation and aggravation (**Fig. 7G**).

Discussion

Heterogeneity within dysfunctional exhausted $CD8^+$ T cells and its role in tumor progression are poorly understood. In this report, we identified two different exhausted $CD8^+$ T-cell subpopulations within the human breast and ovarian tumor tissues, designated Lin^+ $PD1^+$ $TCF1^+$ T_{PEX} and Lin^+ $PD1^+$ $TCF1^-$ T_{TEX} cells. These two subsets are phenotypically and functionally distinct, exhibiting differential responses to PD-1 blockade. Our findings corroborate with the preliminary reports of such subsets in patients with melanoma (27). However, previous studies were centralized on improving the therapeutic candidature of T_{PEX} cells without highlighting T_{TEX} cells and their direct impact within the TME. Therefore, in this study, we aimed to analyze dysfunctional T_{TEX} cells and their ramifications on tumor advancement.

Our study disclosed a strong association between dysfunctional exhausted $CD8^+$ TIL population and CSCs in breast and ovarian carcinoma, indicating their possible alliance in tumor promotion. Furthermore, it was uncovered that $CD8^+$ T cell exhaustion status, early-state progenitor exhaustion or late-state terminal exhaustion might depend on overall immune infiltration or immune contexture of the TME. Moreover, because patient with cold tumor shows more tumor aggressiveness with increased T_{TEX} frequency and CSCs with accentuated stem-cell transcription factors than inflamed tumors, it can be postulated that weak tumor infiltration of $CD8^+$ T cells and their exhaustion state may dictate the clinical outcome. The association of T_{TEX} and CSCs across human and murine metastatic scenarios further solidifies this notion. This corroborates with previous studies where CSC elevation corresponded to poor prognosis and decreased overall survival (OS; refs. 42, 43).

When this T_{TEX} and CSC kinship was further investigated *in vitro*, it was found that both exhausted $CD8^+$ T-cell subsets actively upregulated the CSC population. However, the degree of CSC elevation varied weakly between the T_{PEX}- and T_{TEX}-influenced cohorts. Furthermore, treatment with the PD-1–PD-L1 interaction inhibitor (ab230369) prohibited T_{PEX}-induced CSC generation, whereas T_{TEX}-induced CSC upregulation remained unhinged. This was also reflected in other CSC-attributes like tumorigenic potential and stem-cell regulatory transcription factors. Thus, it can be speculated that a patient with a noninflamed tumor stroma, with a higher frequency of T_{TEX} may not benefit from anti–PD-1 therapy.

Furthermore, to assess T_{TEX}'s precise impact on tumor progression, T_{TEX}-influenced CSCs were characterized. It was found that T_{TEX}-influenced CSCs mostly remain in a hybrid EMT/mesenchymal-epithelial transition (MET) state pertaining both epithelial and mesenchymal features. Previously it has been demonstrated that hybrid-E-M–state confers highest plasticity and stemness of CSCs (44–45). In line with their report, here we have found T_{TEX}-CSCs with higher clonogenicity exhibiting significantly higher rates of hepatic metastasis in athymic nude mice. Interestingly, T_{PEX}-CSCs with the mesenchymal traits demonstrated a lower rate of metastasis. Apart from metastatic potential, the EMT–MET state may manifest other CSC characteristics; such as the overexpression of *twist* in T_{TEX}-CSCs. This might play a multi-faceted role by maintaining stemness via OCT4 and by promoting invasiveness and metastasis through the sustained development of invadopodia and drug resistance via the SOX2–ABCG2 axis (46–48). Downregulation of *vimentin* may provide more nuclear flexibility and migration of amoeboid-T_{TEX}–CSCs through confined environments (49).

This EMT–MET dynamicity is strongly reflected in the morphology of T_{TEX}-induced–CSCs, which display an invasive architecture through invadopodia development, nuclear and cytosolic elongation and cofilin overexpression. Previous reports showed that cancer cells typically use invadopodia to mediate focal degradation of ECM by MMPs for their invasion and metastasis (50). Remarkably, a positive correlation between increased cofilin expression and proliferation, invasion, migration, and reduced OS of patients was reported in various forms of cancer such as non–small cell lung cancer (NSCLC), breast, and prostate cancers (51–53). Complementing these reports, our Matrigel invasion assay and RT-PCR analysis revealed that T_{TEX}-induced CSCs are indeed highly invasive with MMP7 overexpression. Because these invasive CSCs tend to migrate to secondary sites, chemotaxis associated molecules were canvassed. Our notion was further confirmed by increased expression of CXCR4, indicating the possibility of metastatic spread. Surprisingly, CXCR4 was found to be heavily localized in the nucleus of T_{TEX}-induced CSCs. A similar observation was also reported in patients with metastatic renal and colorectal carcinomas, where high nuclear CXCR4 expression, but not cytoplasmic CXCR4 expression correlated with a poor prognosis and reduced progression-free survival (PFS; refs. 54–55).

Recent reports on human colorectal cancer have highlighted the importance of immune contexture, lymphatic vessel densities, and *in situ* T-cell infiltrate or immunoscore in determining distant metastasis via DTCs (56). We also observed a similar pattern. In cold tumors with elevated T_{TEX}-influenced–CSCs, heavy accumulations of flexible invasive DTCs were noted. These DTCs overly infiltrate TDLNs through lymphatic vessels and eventually reach to a distant site to initiate hepatic metastasis.

Moreover, T_{TEX}-influenced CSCs displayed high MDR phenotypes with overexpressed drug efflux pump-regulating genes such as *abcc1* and *abcb1*. Thus targeting them with conventional chemotherapy becomes considerably more difficult. Earlier reports suggested a survival benefit of CSCs acquiring MRP1 after chemotherapy in patients with brain tumors (57). Thus, our observation further solidifies that CSCs residing stably in an intermediate EMT–MET state and coexpressing both E and M markers, are critical for rapid polyfunctionality, increased drug resistance, invasiveness, and metastatic ability.

Because CSC attributes are primarily orchestrated by transcription factors such as OCT4, SOX2, KLF4, NANOG (58), their status was evaluated. Our results disclosed the significant upregulation of these molecules in T_{TEX}-CSCs, correlating to previous findings. T_{TEX}-CSCs were also enriched with *aldh1*, that may contributed to their invasive morphology (59). Therefore, our study demonstrated that T_{TEX} do not

lay silently within the TME, but rather generate a tumor-promoting, highly invasive, aggressive variant of CSC, that are therapeutically resistant. Although, our study could have benefitted from functional assessments of patient-derived T_{TEX}-influenced CSCs, they were not conducted due to limitations in patient samples.

In addition, it is interesting to note that because NOTCH and WNT are linked in their oscillatory pattern to govern stem-cell fate determination, they echo similar expression curves (60). Previous studies have reported that NOTCH inhibition actively results in VEGFR2 increment, followed by cellular sprouting that ultimately aids cellular migration (61–62). In line with these reports, we also observed T_{TEX}-induced CSCs expressing low NOTCH and WNT, overexpressing VEGFR2 and showcasing cellular sprouting in the form of invadopodia, which helps in metastasis.

Finally, because T_{TEX} cells remain active perpetrators and are nonresponsive to anti–PD-1 therapy, determining combat strategies are urgently needed. Given this, we explored the involved signaling networks that might have therapeutic implications. Our results suggest that T_{TEX} instigates this aggressive CSC generation via contact-dependent receptor–ligand interactions. They involve unorthodox LAMP3/NRP1–VEGFR2 signaling cascade instead of canonical ligand–dependent pathways such as NOTCH and WNT (63). Our observation correlate with previous reports of positive associations between LAMP3 and invasiveness, resistance to chemotherapy and radiotherapy and poor survival in patients with ovarian carcinoma (64). Moreover, according to recent report on human lung cancer, T_{TEX} CD8$^+$ T-cell populations with higher frequency of NRP1 show a negative regulation of antitumor immunity (65). Silencing of the axis resulted in CSC frequency reduction, tumorsphere formation and normalized CXCR4 distribution from the nucleus to the cytosol. Therefore, our observation provides a directive for therapeutic targeting of T_{TEX}-induced tumor promotion.

Altogether, this study provides mechanistic insights into how heterogeneous, exhausted cell subsets differentially modulate CSC population to drive tumor aggressiveness. Our findings suggest that the ultimate therapeutic benefit of ICI therapy depends on both the frequency and exhausted state of infiltrated CD8$^+$ T cells. Furthermore, vicious T_{TEX} not only escapes the scythe of the PD-1 blockade but also simultaneously promotes tumor advancement. Thus, in the future, T_{TEX} frequency could be used as a prospective biomarker for identifying potential nonresponders to anti-PD1-therapy, particularly in cold tumors. In addition, our study implies that neutralizing LAMP3/NRP1 on T_{TEX} cells has a possible therapeutic benefit in patients with poor immune infiltration. As such, LAMP3/NRP1 may serve as potential drug targets; that require thorough validation from a large pool of human tumor samples.

Future studies are needed to investigate how T_{TEX} evade the PD-1 blockade despite their overexpression of PD-1. Possible antitumor roles of other inhibitory receptors in T_{TEX} may also be ascertained. The alternate route, could also be investigated, that is, the possibility of CSC-mediated T_{TEX} generation.

Authors' Disclosures

No disclosures were reported.

Authors' Contributions

M. Chakravarti: Conceptualization, resources, data curation, software, formal analysis, validation, investigation, visualization, methodology, writing–original draft, writing–review and editing. **S. Dhar:** Data curation and investigation. **S. Bera:** Software and investigation. **A. Sinha:** Data curation. **K. Roy:** Software. **A. Sarkar:** Methodology. **S. Dasgupta:** Methodology. **A. Bhuniya:** Methodology. **A. Saha:** Methodology. **J. Das:** Methodology. **S. Banerjee:** Visualization and methodology. **M. Vernekar:** Resources. **C. Pal:** Resources. **N. Alam:** Resources. **D. Datta:** Resources. **R. Baral:** Conceptualization, resources, supervision, funding acquisition, validation, visualization, methodology, project administration, writing–review and editing. **A. Bose:** Conceptualization, resources, data curation, supervision, funding acquisition, validation, investigation, visualization, project administration, writing–review and editing.

Acknowledgments

In addition to institutional support, this study was supported by Department of Science and Technology, New Delhi, Government of India (grant numbers: SB/YS/LS-289/2013 and SR/WOS-A/LS-152/2017; to A. Bose), University Grant Commission, New Delhi, Government of India (Ref. number: 21/06/2015(I)EU-V) (PhD fellowship to M. Chakravarti), and Indian Council of Medical Research, New Delhi, India (grant number: 61/1/2019-BMS) for providing partial support. Funding includes fellowship to scholars and cost of reagents only. The authors thank Director, CNCI, Kolkata, India, for providing institutional facilities. Special thanks to Dr. Abhijit Rakshit, Head, Animal Facilities, CNCI, Kolkata. The authors also wish to thank all members of our respective laboratories for their technical support for this work. They would like to thank Editage (www.editage.com) for English language editing.

Note

Supplementary data for this article are available at Cancer Research Online (http://cancerres.aacrjournals.org/).

Received December 10, 2022; revised February 22, 2023; accepted March 22, 2023; published first March 27, 2023.

References

1. Batlle E, Clevers H. Cancer stem cells revisited. Nat Med 2017;23:1124–34.
2. Nassar D, Blanpain C. Cancer stem cells: basic concepts and therapeutic implications. Annu Rev Pathol Mech Dis 2016;11:47–76.
3. Chaffer CL, Brueckmann I, Scheel C, Kaestli AJ, Wiggins PA, Rodrigues LO, et al. Normal and neoplastic nonstem cells can spontaneously convert to a stem-like state. Proc Natl Acad Sci 2011;108:7950–5.
4. Auffinger B, Tobias AL, Han Y, Lee G, Guo D, Dey M, et al. Conversion of differentiated cancer cells into cancer stem-like cells in a glioblastoma model after primary chemotherapy. Cell Death Differ 2014;21:1119–31.
5. Lytle NK, Barber AG, Reya T. Stem cell fate in cancer growth, progression and therapy resistance. Nat Rev Cancer 2018;18:669–80.
6. Najafi M, Mortezaee K, Majidpoor J. Cancer stem cell (CSC) resistance drivers. Life Sci 2019;234:116781.
7. Steinbichler TB, Dudás J, Skvortsov S, Ganswindt U, Riechelmann H, Skvortsova I-I. Therapy resistance mediated by cancer stem cells. Semin Cancer Biol 2018;53:156–67.
8. Najafi M, Farhood B, Mortezaee K, Kharazinejad E, Majidpoor J, Ahadi R. Hypoxia in solid tumors: a key promoter of cancer stem cell (CSC) resistance. J Cancer Res Clin Oncol 2020;146:19–31.
9. Yao X, Ping Y, Bian X. Contribution of cancer stem cells to tumor vasculogenic mimicry. Protein Cell 2011;2:266–72.
10. Koren E, Fuchs Y. The bad seed: cancer stem cells in tumor development and resistance. Drug Resist Updat 2016;28:1–12.
11. Papadaki MA, Stoupis G, Theodoropoulos PA, Mavroudis D, Georgoulias V, Agelaki S. Circulating tumor cells with stemness and epithelial-to-mesenchymal transition features are chemoresistant and predictive of poor outcome in metastatic breast cancer. Mol Cancer Ther 2019;18:437–47.
12. Zhao Y, Bao Q, Renner A, Camaj P, Eichhorn M, Ischenko I, et al. Cancer stem cells and angiogenesis. Int J Dev Biol 2011;55:477–82.
13. Markowska A, Sajdak S, Markowska J, Huczyn´ski A. Angiogenesis and cancer stem cells: new perspectives on therapy of ovarian cancer. Eur J Med Chem 2017;142:87–94.

14. Choi S-H, Kim A-R, Nam J-K, Kim J-M, Kim J-Y, Seo HR, et al. Tumour-vasculature development via endothelial-to-mesenchymal transition after radiotherapy controls CD44v6+ cancer cell and macrophage polarization. Nat Commun 2018;9:5108.
15. Huang H, Wang C, Liu F, Li H-Z, Peng G, Gao X, et al. Reciprocal network between cancer stem-like cells and macrophages facilitates the progression and androgen deprivation therapy resistance of prostate cancer. Clin Cancer Res 2018;24:4612–26.
16. Kuroda H, Mabuchi S, Yokoi E, Komura N, Kozasa K, Matsumoto Y, et al. Prostaglandin E2 produced by myeloid-derived suppressive cells induces cancer stem cells in uterine cervical cancer. Oncotarget 2018;9:36317–30.
17. Solis-Castillo LA, Garcia-Romo GS, Diaz-Rodriguez A, Reyes-Hernandez D, Tellez-Rivera E, Rosales-Garcia VH, et al. Tumor-infiltrating regulatory T cells, CD8/Treg ratio, and cancer stem cells are correlated with lymph node metastasis in patients with early breast cancer. Breast Cancer 2020;27: 837–49.
18. Yin T, Wang G, He S, Liu Q, Sun J, Wang Y. Human cancer cells with stem cell-like phenotype exhibit enhanced sensitivity to the cytotoxicity of IL-2 and IL-15 activated natural killer cells. Cell Immunol 2016;300:41–5.
19. Todaro M, D'Asaro M, Caccamo N, Iovino F, Francipane MG, Meraviglia S, et al. Efficient killing of human colon cancer stem cells by γδ T lymphocytes. J Immunol 2009;182:7287–96.
20. Chen W, Qin Y, Liu S. Cytokines, breast cancer stem cells (BCSCs) and chemoresistance. Clin Transl Med 2018;7:27.
21. Wherry EJ, Kurachi M. Molecular and cellular insights into T cell exhaustion. Nat Rev Immunol 2015;15:486–99.
22. Thommen DS, Schumacher TN. T cell dysfunction in cancer. Cancer Cell 2018; 33:547–62.
23. Hashimoto M, Kamphorst AO, Im SJ, Kissick HT, Pillai RN, Ramalingam SS, et al. CD8 T cell exhaustion in chronic infection and cancer: opportunities for interventions. Annu Rev Med 2018;69:301–18.
24. Blank CU, Haining WN, Held W, Hogan PG, Kallies A, Lugli E, et al. Defining 'T cell exhaustion'. Nat Rev Immunol 2019;19:665–74.
25. Darvin P, Toor SM, Sasidharan Nair V, Elkord E. Immune checkpoint inhibitors: recent progress and potential biomarkers. Exp Mol Med 2018;50:1–11.
26. Zarour HM. Reversing T-cell dysfunction and exhaustion in cancer. Clin Cancer Res 2016;22:1856–64.
27. Miller BC, Sen DR, Al Abosy R, Bi K, Virkud YV, LaFleur MW, et al. Subsets of exhausted CD8+ T cells differentially mediate tumor control and respond to checkpoint blockade. Nat Immunol 2019;20:326–36.
28. Siddiqui I, Schaeuble K, Chennupati V, Fuertes Marraco SA, Calderon-Copete S, Pais Ferreira D, et al. Intratumoral Tcf1+PD-1+CD8+ T cells with stem-like properties promote tumor control in response to vaccination and checkpoint blockade immunotherapy. Immunity 2019;50:195–211.
29. Im SJ, Ha S-J. Re-defining T-cell exhaustion: subset, function, and regulation. Immune Netw 2020;20:e2.
30. Jensen EC. Quantitative analysis of histological staining and fluorescence using ImageJ. Anat Rec 2013;296:378–81.
31. Nair S, Archer GE, Tedder TF. Isolation and generation of human dendritic cells. Curr Protoc Immunol 2012;Chapter 7:7.32.1–7.32.23.
32. Ghosh T, Nandi P, Ganguly N, Guha I, Bhuniya A, Ghosh S, et al. NLGP counterbalances the immunosuppressive effect of tumor-associated mesenchymal stem cells to restore effector T cell functions. Stem Cell Res Ther 2019;10:296.
33. Schneider CA, Rasband WS, Eliceiri KW. NIH image to ImageJ: 25 years of image analysis. Nat Methods 2012;9:671–5.
34. Sharma R, Sharma A, Kumar A, Jaganathan B. Phospho-protein analysis in adherent cells using flow cytometry. Bio-Protocol 2019;9:e3395.
35. Dasgupta S, Ghosh T, Dhar J, Bhuniya A, Nandi P, Das A, et al. RGS5–TGFβ–Smad2/3 axis switches pro- to anti-apoptotic signaling in tumor-residing pericytes, assisting tumor growth. Cell Death Differ 2021;28: 3052–76.
36. Denkert C, von Minckwitz G, Darb-Esfahani S, Lederer B, Heppner BI, Weber KE, et al. Tumour-infiltrating lymphocytes and prognosis in different subtypes of breast cancer: a pooled analysis of 3771 patients treated with neoadjuvant therapy. Lancet Oncol 2018;19:40–50.
37. Salgado R, Denkert C, Demaria S, Sirtaine N, Klauschen F, Pruneri G, et al. The evaluation of tumor-infiltrating lymphocytes (TILs) in breast cancer: recommendations by an International TILs working group 2014. Ann Oncol 2015;26: 259–71.
38. Hendry S, Salgado R, Gevaert T, Russell PA, John T, Thapa B, et al. Assessing tumor-infiltrating lymphocytes in solid tumors: a practical review for pathologists and proposal for a standardized method from the international immunooncology biomarkers working group: Part 1: assessing the host immune response, TILs in invasi. Adv Anat Pathol 2017;24:235–51.
39. Hendry S, Salgado R, Gevaert T, Russell PA, John T, Thapa B, et al. Assessing tumor-infiltrating lymphocytes in solid tumors: a practical review for pathologists and proposal for a standardized method from the international immuno-oncology biomarkers working group: Part 2: TILs in melanoma, gastrointestinal tract carcinom. Adv Anat Pathol 2017;24:311–35.
40. Domigan CK, Ziyad S, Luisa Iruela-Arispe M. Canonical and noncanonical vascular endothelial growth factor pathways: new developments in biology and signal transduction. Arterioscler Thromb Vasc Biol 2015;35:30–9.
41. Kouwenberg M, Rops A, Bakker-Van Bebber M, Diepeveen L, Götte M, Hilbrands L, et al. Role of syndecan-1 in the interaction between dendritic cells and T cells. PLoS One 2020;15:1–16.
42. Joseph C, Arshad M, Kurozomi S, Althobiti M, Miligy IM, Al-izzi S, et al. Overexpression of the cancer stem cell marker CD133 confers a poor prognosis in invasive breast cancer. Breast Cancer Res Treat 2019;174:387–99.
43. Connor EV, Saygin C, Braley C, Wiechert AC, Karunanithi S, Crean-Tate K, et al. Thy-1 predicts poor prognosis and is associated with self-renewal in ovarian cancer. J Ovarian Res 2019;12:112.
44. Liu S, Cong Y, Wang D, Sun Y, Deng L, Liu Y, et al. Breast cancer stem cells transition between epithelial and mesenchymal states reflective of their normal counterparts. Stem Cell Reports 2014;2:78–91.
45. Jolly MK, Jia D, Boareto M, Mani SA, Pienta KJ, Ben-Jacob E, et al. Coupling the modules of EMT and stemness: a tunable 'stemness window' model. Oncotarget 2015;6:25161–74.
46. Izadpanah MH, Abbaszadegan MR, Fahim Y, Forghanifard MM. Ectopic expression of TWIST1 upregulates the stemness marker OCT4 in the esophageal squamous cell carcinoma cell line KYSE30. Cell Mol Biol Lett 2017;22:33.
47. Eckert MA, Santiago-Medina M, Lwin TM, Kim J, Courtneidge SA, Yang J. ADAM12 induction by TWIST1 promotes tumor invasion and metastasis via regulation of invadopodia and focal adhesions. J Cell Sci 2017;130: 2036–48.
48. Mukherjee P, Gupta A, Chattopadhyay D, Chatterji U. Modulation of SOX2 expression delineates an end-point for paclitaxel-effectiveness in breast cancer stem cells. Sci Rep 2017;7:9170.
49. Lavenus SB, Tudor SM, Ullo MF, Vosatka KW, Logue JS. A flexible network of vimentin intermediate filaments promotes migration of amoeboid cancer cells through confined environments. J Biol Chem 2020;295:6700–9.
50. Kumar S, Das A, Barai A, Sen S. MMP secretion rate and inter-invadopodia spacing collectively govern cancer invasiveness. Biophys J 2018;114:650–62.
51. Chang C, Chang S, Leu J, Chang Y, Hsiao M, Lin L, et al. Comparison of cofilin-1 and Twist-1 protein expression in human non□small cell lung cancer tissues. Oncol Rep 2019;42:805–16.
52. Maimaiti Y, Tan J, Liu Z, Guo Y, Yan Y, Nie X, et al. Overexpression of cofilin correlates with poor survival in breast cancer: a tissue microarray analysis. Oncol Lett 2017;14:2288–94.
53. Chen L, Cai J, Huang Y, Tan X, Guo Q, Lin X, et al. Identification of cofilin-1 as a novel mediator for the metastatic potentials and chemoresistance of the prostate cancer cells. Eur J Pharmacol 2020;880:173100.
54. Wang S-C, Lin J-K, Wang H-S, Yang S-H, Li AF-Y, Chang S-C. Nuclear expression of CXCR4 is associated with advanced colorectal cancer. Int J Colorectal Dis 2010;25:1185–91.
55. Bao Y, Wang Z, Liu B, Lu X, Xiong Y, Shi J, et al. A feed-forward loop between nuclear translocation of CXCR4 and HIF-1α promotes renal cell carcinoma metastasis. Oncogene 2019;38:881–95.
56. Bindea G, Mlecnik B, Galon J. Tumor spread or siege immunity: dissemination to distant metastasis or not. Oncoimmunology 2021;10:1–3.
57. Jin F, Zhao L, Guo Y-J, Zhao W-J, Zhang H, Wang H-T, et al. Influence of Etoposide on anti-apoptotic and multidrug resistance-associated protein genes in CD133 positive U251 glioblastoma stem-like cells. Brain Res 2010;1336:103–11.
58. Yang L, Shi P, Zhao G, Xu J, Peng W, Zhang J, et al. Targeting cancer stem cell pathways for cancer therapy. Signal Transduct Target Ther 2020;5:8.
59. Yang L, Ren Y, Yu X, Qian F, Bian B-S-J, Xiao H, et al. ALDH1A1 defines invasive cancer stem-like cells and predicts poor prognosis in patients with esophageal squamous cell carcinoma. Mod Pathol 2014;27:775–83.

60. Sonnen KF, Lauschke VM, Uraji J, Falk HJ, Petersen Y, Funk MC, et al. Modulation of phase shift between Wnt and notch signaling oscillations controls mesoderm segmentation. Cell 2018;172:1079–90.
61. Bentley K, Franco CA, Philippides A, Blanco R, Dierkes M, Gebala V, et al. The role of differential VE-cadherin dynamics in cell rearrangement during angiogenesis. Nat Cell Biol 2014;16:309–21.
62. Meisel CT, Porcheri C, Mitsiadis TA. Cancer stem cells, Quo Vadis? The notch signaling pathway in tumor initiation and progression. Cells 2020; 9:1879.
63. Fendler A, Bauer D, Busch J, Jung K, Wulf-Goldenberg A, Kunz S, et al. Inhibiting WNT and NOTCH in renal cancer stem cells and the implications for human patients. Nat Commun 2020;11:929.
64. Wang D, Cao X, Zhang Y, Liu Y, Yao C, Ge W, et al. LAMP3 expression correlated with poor clinical outcome in human ovarian cancer. Tumor Biol 2017;39:101042831769501.
65. Liu C, Somasundaram A, Manne S, Gocher AM, Szymczak-Workman AL, Vignali KM, et al. Neuropilin-1 is a T cell memory checkpoint limiting long-term antitumor immunity. Nat Immunol 2020;21:1010–21.

Journal for ImmunoTherapy of Cancer

Dendritic cell vaccines targeting tumor blood vessel antigens in combination with dasatinib induce therapeutic immune responses in patients with checkpoint-refractory advanced melanoma

Walter J Storkus ,[1] Deena Maurer,[2] Yan Lin,[3] Fei Ding,[4] Anamika Bose,[5] Devin Lowe,[6] Amy Rose,[7] Melissa DeMark,[8] Lilit Karapetyan,[9] Jennifer L Taylor,[1] Manoj Chelvanambi,[10] Ronald J Fecek,[11] Jessica N Filderman,[10] Timothy J Looney,[12] Lauren Miller,[13] Elizabeth Linch,[13] Geoffrey M Lowman ,[13] Pawel Kalinski,[14] Lisa H Butterfield ,[15,16] Ahmad Tarhini ,[17] Hussein Tawbi ,[18] John M Kirkwood[19]

To cite: Storkus WJ, Maurer D, Lin Y, *et al*. Dendritic cell vaccines targeting tumor blood vessel antigens in combination with dasatinib induce therapeutic immune responses in patients with checkpoint-refractory advanced melanoma. *Journal for ImmunoTherapy of Cancer* 2021;**9**:e003675. doi:10.1136/jitc-2021-003675

► Additional supplemental material is published online only. To view, please visit the journal online (http://dx.doi.org/10.1136/jitc-2021-003675).

WJS and DM are joint first authors.

HT and JMK are joint senior authors.

Accepted 17 October 2021

For numbered affiliations see end of article.

Correspondence to
Professor Walter J Storkus; storkuswj@upmc.edu

ABSTRACT

Background A first-in-human, randomized pilot phase II clinical trial combining vaccines targeting overexpressed, non-mutated tumor blood vessel antigens (TBVA) and tyrosine kinase inhibitor dasatinib was conducted in human leukocyte antigen (HLA)-A2$^+$ patients with advanced melanoma.

Methods Patient monocyte-derived type-1-polarized dendritic cells were loaded with HLA-A2-presented peptides derived from TBVA (DLK1, EphA2, HBB, NRP1, RGS5, TEM1) and injected intradermally as a vaccine into the upper extremities every other week. Patients were randomized into one of two treatment arms receiving oral dasatinib (70 mg two times per day) beginning in week 5 (Arm A) or in week 1 (Arm B). Trial endpoints included T cell response to vaccine peptides (interferon-γ enzyme-linked immunosorbent spot), objective clinical response (Response Evaluation Criteria in Solid Tumors V.1.1) and exploratory tumor, blood and serum profiling of immune-associated genes/proteins.

Results Sixteen patients with advanced-stage cutaneous (n=10), mucosal (n=1) or uveal (n=5) melanoma were accrued, 15 of whom had previously progressed on programmed cell death protein 1 (PD-1) blockade. Of 13 evaluable patients, 6 patients developed specific peripheral blood T cell responses against ≥3 vaccine-associated peptides, with further evidence of epitope spreading. All six patients with specific CD8$^+$ T cell response to vaccine-targeted antigens exhibited evidence of T cell receptor (TCR) convergence in association with preferred clinical outcomes (four partial response and two stabilization of disease (SD)). Seven patients failed to respond to vaccination (one SD and six progressive disease). Patients in Arm B (immediate dasatinib) outperformed those in Arm A (delayed dasatinib) for immune response rate (IRR; 66.7% vs 28.6%), objective response rate (ORR) (66.7% vs 0%), overall survival (median 15.45 vs 3.47 months; p=0.0086) and progression-free survival (median 7.87 vs 1.97 months; p=0.063). IRR (80% vs 25%) and ORR (60% vs 12.5%) was greater for females versus male patients. Tumors in patients exhibiting response to treatment displayed (1) evidence of innate and adaptive immune-mediated inflammation and TCR convergence at baseline, (2) on-treatment transcriptional changes associated with reduced hypoxia/acidosis/glycolysis, and (3) increased inflammatory immune cell infiltration and tertiary lymphoid structure neogenesis.

Conclusions Combined vaccination against TBVA plus dasatinib was safe and resulted in coordinating immunologic and/or objective clinical responses in 6/13 (46%) evaluable patients with melanoma, particularly those initiating treatment with both agents.

Trial registration number NCT01876212.

INTRODUCTION

The incidence of melanoma continues to rise, with American Cancer Society estimates of >100,000 diagnoses of this form of cancer in 2021, and over 7180 disease-associated deaths.[1] The landscape of first-line treatment options for patients with advanced-stage IIIB-IV melanoma has been recalibrated over the past decade with the advent of targeted small molecule inhibitors (ie, BRAFi, MEKi) and immune checkpoint blockade, resulting in increased rates of objective clinical response (OCR) but also a significant rise in the incidence of immune-related adverse events.[2 3] Despite improved rates of response, most patients with melanoma exhibit primary

or acquired resistance to immune checkpoint blockade, reinforcing the need to develop effective salvage therapies.[4]

Although melanoma vaccines have been universally well-tolerated by patients,[5] their performance in past phase II/III trials has proven disappointing overall, with minimal clinical benefits reported versus new standard-of-care therapies.[6] Numerous factors have been posited to limit vaccine efficacy in patients with cancer, including variance in host immune competency, heterogeneity in tumor antigenicity/immunogenicity, a tumor microenvironment (TME) refractory to vaccine-induced T effector cell infiltration and sustained 'fitness', and expansion of immunoregulatory networks, among others.[3 5 7] We have previously demonstrated in preclinical models that vaccines targeting non-mutated antigens (ie, DLK1, EphA2, HBB, NRP1, RGS5 and TEM1) overexpressed by tumor-associated (but not normal tissue-associated) vascular endothelial cells or pericytes promote T cell-dependent tumor vascular normalization in mice, resulting in superior immune cell recruitment, a pro-inflammatory TME and slowed tumor growth or regression.[8–10] While dasatinib monotherapy is ineffective in treating patients with advanced melanoma,[11] we and others have also reported that dasatinib functions as a potent adjuvant to specific vaccination in murine melanoma models.[12 13] In this context, the combination of dasatinib +vaccine therapy promoted: (1) superior expansion and recruitment of therapeutic T cells into tumors (via locoregional production of CXCR3 ligand chemokines), (2) reduced tumor hypoxia and prevalence of myeloid-derived suppressor cells (MDSC) and regulatory T cells (Treg), (3) broadening/spreading in the antitumor $CD8^+$ T cell repertoire, and (4) extended overall survival.[12]

Based on these translational findings, we developed a single-center, prospective randomized pilot phase II clinical trial combining these modalities for the treatment of human leukocyte antigen (HLA)-$A2^+$ patients with advanced melanoma. We confirmed the safety, immunogenicity and antitumor efficacy of intradermal administration of autologous type-1 dendritic cells (αDC1) loaded with a mixture of six HLA-A2-presented peptides derived from the tumor-associated vascular antigens DLK1, EphA2, HBB, NRP1, RGS5 and TEM1 combined with daily oral administration of dasatinib (70 mg two times per day) as an immune adjuvant/conditioning agent in patients who had failed prior therapies, including checkpoint blockade.

MATERIALS AND METHODS

Patients

This was a single-center, first-in-human, prospective randomized pilot phase II clinical trial (University of Pittsburgh Cancer Institute (UPCI) 12-048) for HLA-$A2^+$ patients with advanced-stage (IIC-IV) cutaneous, mucosal or uveal melanoma (performed between May 2014 and July 2019) for whom standard curative or palliative measures did not exist or were no longer effective. The study was ended due to conclusion of NIH R01 CA169118 grant support. Patient eligibility/exclusion criteria are described in online supplemental materials. Informed consent was obtained from all patients entered onto this study. Patient demographic information is provided in online supplemental table S1.

Autologous αDC1/TBVA peptide vaccine generation (BB-IND 15224)

Patient αDC1 vaccines were generated from apheresis products and quality controlled as previously described,[14] with further details provided in online supplemental file 3. Aliquots of cryopreserved vaccine αDC1 were analyzed for transcriptional and proteomic profiles in exploratory studies using Affymetrix GeneChips and FACS analysis, respectively, as described below (online supplemental figure 1).

Study design and treatment

Sixteen patients were enrolled, with one patient voluntarily withdrawing from trial prior to vaccine generation and one patient expiring after vaccine generation but prior to treatment. Of the 14 patients receiving treatment, 13 were evaluable for all endpoint analyses, with 1 patient expiring prior to the completion of treatment cycle 1. Patients were randomized onto one of two treatment arms (figure 1A). All treated patients received an autologous αDC1/peptide vaccine administered by a single intradermal injection of approximately 10^7 cells on days 1 and 15 of each monthly therapy cycle. Intradermal administration of the vaccine was provided in the vicinity of the nodal drainage groups of the four extremities and was performed on an outpatient basis in the Hillman Cancer Center Clinical and Translational Research Center. Patients on Arm A started dasatinib administration (70 mg orally two times per day) on cycle 2, day 1 (ie, in week 5), while patients on Arm B began dasatinib administration on cycle 1, day 1 (ie, in week 1). Study treatment was continued for at least six cycles or until disease progression, intercurrent illness preventing further treatment, unacceptable adverse event(s), or unacceptable changes in the patient's condition. Patients were followed for 1 year after removal from study treatment or until death, whichever occurred first.

Study endpoints

The primary endpoint of this clinical trial was patient peripheral blood T cell response to vaccine peptides based on interferon (IFN)-γ enzyme-linked immunosorbent spot (ELISPOT) analyses. Secondary endpoints included safety and investigator-assessed OCR and objective response rate (ORR) by Response Evaluation Criteria in Solid Tumors (RECIST) V.1.1, progression-free survival (PFS), overall survival (OS) and exploratory analyses of patient blood, tumor and serum specimens for treatment-associated changes in Treg/MDSC content (blood),

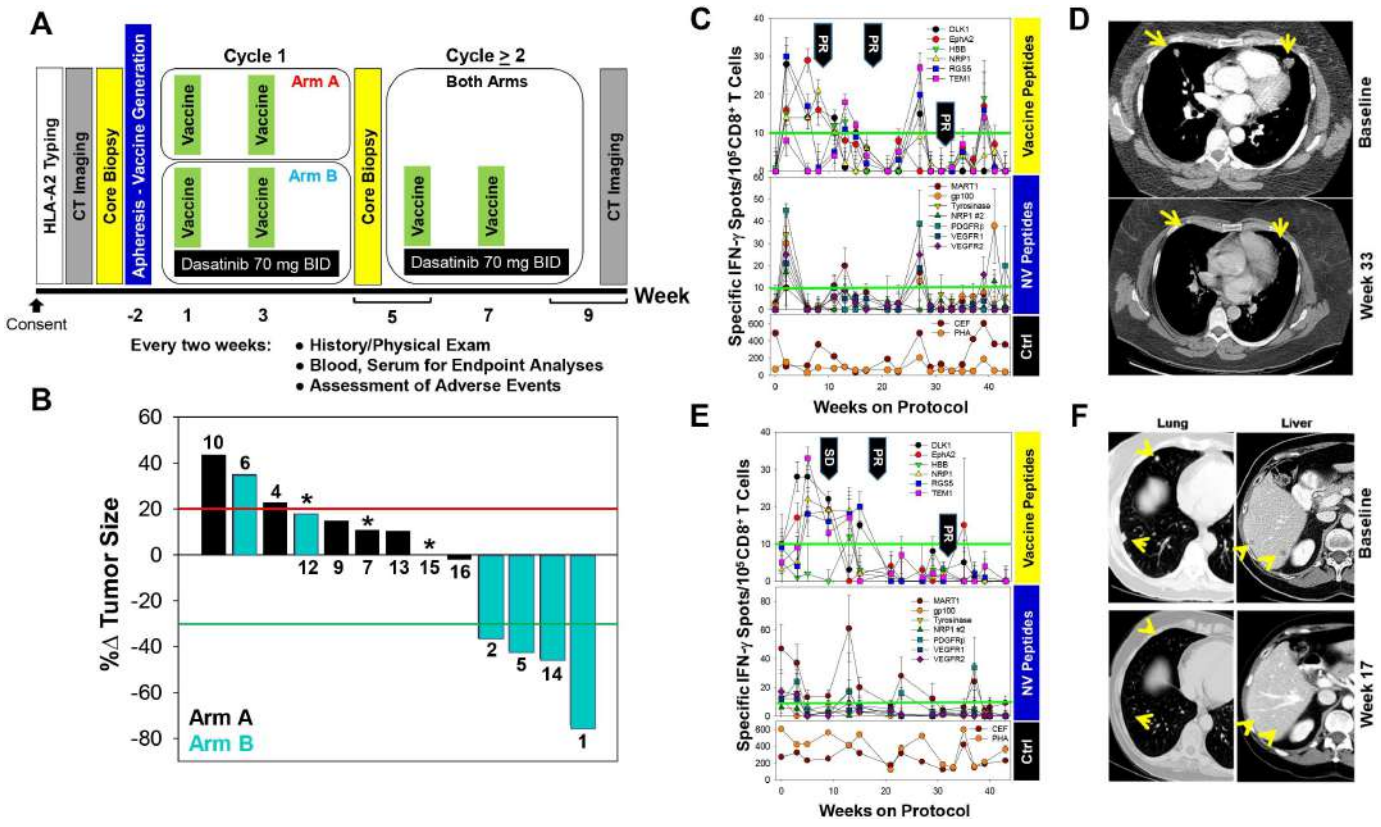

Figure 1 Protocol schema and examples of immunologic and clinical responses to treatment with dendritic cell/tumor blood vessel antigens peptide-based vaccines + dasatinib. In (A), outline of treatment schema on Arm A (vaccine + dasatinib beginning in week 5) or Arm B (vaccine + dasatinib beginning in week 1). In (B), a waterfall plot is provided depicting greatest change in tumor burden on-treatment, with 20% increase/30% decrease in tumor size indicated by solid red/green horizontal lines, respectively. Inset numbers reflect patient #. *Patients with progressive disease based on development/progression of new disease sites on-treatment. Patients #1 (B/D) and #5 (panels E/F) were both treated on Arm B of this trial and developed coordinate immune response to vaccine peptides as well as non-vaccine, but disease-relevant peptides as determined in IFN-γ enzyme-linked immunosorbent spot assays (C/E), and objective partial clinical responses exemplified by shrinkage of visceral metastases in positron emission tomography/CT imaging (D/F). Yellow arrows in panels D and F indicate target lesions at baseline versus on-treatment. BID, two times per day; Ctrl, control stimuli (peptides derived from cytomegalovirus, Epstein-Barr virus and influenza virus (CEF) proteins; HLA, human leukocyte antigen; IFN, interferon; NV, non-vaccine; PR, partial response; SD, stabilization of disease.

vascular structure (tumor) and pro-inflammatory CXCL10 levels (serum). Radiographic imaging was performed at baseline and then approximately every 8–9 weeks until disease progression by CT or positron emission tomography/CT. Response assessments were predicated on RECIST V.1.1 criteria. Adverse events (AEs) were evaluated using the National Cancer Institute Common Terminology Criteria for Adverse Events V.4.0. Tumor biopsies were obtained prior to treatment and at week 5 on-treatment. Peripheral blood specimens were obtained at baseline and then every 2 weeks while on the study protocol. Biopsy tissues were analyzed using quantitative real-time PCR (qRT-PCR) and Thermo Fisher Ion Torrent-based transcriptional profiling platforms (Oncomine TCRB-LR Assay, Oncomine Immune Response Research Assay (OIRRA)).

IFNγ ELISPOT assays

Patient peripheral blood T cell responses against peptides in the vaccine formulation were examined using standardized IFNγ ELISPOT assays as previously described,[15] with further details provided in online supplemental materials. A positive ELISPOT finding on-treatment was defined as a greater than twofold increase in spot-forming reactive T cells versus baseline and at least 10 specific spots (minus background for T2 cells only) per 10^5 immune cells plated. Primary endpoint was considered positive if the patient responded positively against three or more peptides in the vaccine formulation at any time point on-treatment.

Flow cytometry

Baseline and on-treatment patient peripheral blood mononuclear cells were analyzed for frequencies of $CD4^+Foxp3^+$ Treg, $HLA\text{-}DR^{neg}CD3^{neg}CD11b^+CD14^+CD15^{neg}CD19^{neg}CD33^+$ monocytic MDSC (M-MDSC) and $HLA\text{-}DR^{neg}CD3^{neg}CD11b^+CD14^{neg}CD15^+CD19^{neg}CD33^+$ polymorphonuclear MDSC (PMN-MDSC) using an LSRFortessa flow cytometer (BD Biosciences, San Jose,

California, USA) within the Department of Immunology's Unified Flow Core. Vaccine dendritic cells were also phenotyped for expression of costimulatory or checkpoint molecules by flow cytometry as detailed in online supplemental methods.

RNA isolation and gene expression analyses

Total RNA was isolated from vaccine αDC1, tumor biopsies and peripheral blood mononuclear cells and subjected to qRT-PCR and GeneChip Human Genome U133A 2.0 Arrays (Thermo Fisher Scientific) profiling performed by the University of Pittsburgh Genomics Research Core, to the Oncomine TCRB-LR Assay and to the Oncomine Immune Response Research Assay (OIRRA; Thermo Fisher Scientific, Carlsbad, California, USA) under an institutional material transfer agreement. TCRβ chain repertoire libraries were constructed by multiplex PCR utilizing FR1 and constant gene targeting primers via the Oncomine TCRB-LR assay, then sequenced using the Ion Torrent S5 to a target depth of 1.5M raw reads per library. To evaluate T cell receptor (TCR) convergence, we searched for instances where TCRβ chains were identical in amino acid space but had distinct nucleotide sequences owing to N-addition and exonucleotide chewback within the V-D and D-J junctions of the complementary determining region 3. Targeted gene expression profiling of pretreatment and post-treatment tumor biopsies was performed using the OIRRA and total RNA input.

Biostatistics and bioinformatics analyses

Details for biostatistical and bioinformatic methods may be found in online supplemental file 3.

RESULTS

Autologous αDC1/TBVA peptide vaccines + dasatinib are safe, immunogenic and promote clinical responses in PD-1-resistant patients with melanoma in association with extended OS

Fourteen of 16 patients received autologous αDC1/tumor blood vessel antigens (TBVA) peptide vaccines plus dasatinib in two treatment arms distinguished by the start date for dasatinib administration (figure 1, online supplemental figure S1A). The treatment arms were chosen to allow for a comparison of immunogenicity induced by vaccine alone versus vaccine + dasatinib in the first cycle, and to test whether concurrent or sequential administration of dasatinib is more effective. Thirteen of these 14 patients were evaluable for endpoint blood, serum and tumor biopsy analyses at the week 5 time point and CT imaging beginning in week 8/9, with 1 patient expiring in association with disease progression prior to completing cycle 1 of treatment. Although patient immunologic response to vaccine peptides was the primary endpoint in this study, we were struck by unexpected reductions in patient tumor sizes on-treatment, particularly for individuals treated on Arm B versus Arm A (figure 1B; p=0.044). Of the 13 evaluable patients, 6 patients (2 in Arm A and 4 in Arm B) developed specific peripheral blood $CD8^+$ T cell responses against ≥3 of the vaccine peptides that were not detected at baseline based on results obtained in IFN-γ ELISPOT assays (figures 1 and 2). As depicted in figure 1C (patient #1, Arm B) and figure 1E (patient #5, Arm B) examples, vaccine-specific immune responses were detectable as early as trial week 3, with undulating levels of peptide-specific $CD8^+$ T cells observed in longitudinal monitoring of peripheral blood on-treatment. Each of the six vaccine peptides was recognized by at least three evaluable patients, with peptides $DLK1_{310\text{-}318}$, $EphA2_{883\text{-}891}$, $HBB_{31\text{-}39}$, $NRP1_{433\text{-}441}$, $RGS5_{5\text{-}13}$ and $TEM1_{691\text{-}700}$ recognized by 6/6, 3/6, 5/6, 5/6, 4/6 and 4/6 of the immunologic responder patients on-treatment, respectively (figure 2A).

Notably, four out of six patients exhibiting vaccine-specific T cell responses developed OCRs (four partial response (PR) and two stabilization of disease (SD); figure 1D,F and 2A), and of the seven patients that failed to respond immunologically to vaccination, one patient exhibited SD (PFS, OS=8.3 months) while six patients had progressive disease (PD). Of the four patients achieving a PR on this trial, on-treatment $CD8^+$ T cell responses were detected against the vaccine DLK1, EphA2, HBB, NRP1, RGS5 and TEM1 peptides in 4/4, 2/4, 4/4, 3/4, 2/4 and 3/4 cases, respectively (figure 2A). Patients treated on Arm B (ie, combined vaccine + immediate dasatinib from treatment outset) displayed significantly improved OS (median 19.1 vs 8.3 months; p=0.0086) and a trend for improved PFS (median 7.9 vs 2.2 months; p=0.063) versus patients treated on Arm A (ie, vaccine + delayed dasatinib administration beginning in week 5; figure 2B, online supplemental table S2). Patient T cell response to vaccine peptides (figure 2C) and non-vaccine (NV; ie, 'spread') peptides (figure 2D) as determined in IFN-γ ELISPOT assays was predictive of extended OS in vaccinated patients.

Overall, the combination vaccine + dasatinib immunotherapy was well-tolerated, with no treatment-related AEs > grade 3 observed (online supplemental tables S3 and S4). Among the 15 patients receiving at least one vaccine, the most commonly observed AEs included anemia (8 patients), fatigue (10 patients) and hyponatremia (9 patients), consistent with AEs reported for dasatinib monotherapy. Patients treated on Arm B versus Arm A had increased incidence of fever (33% vs 0%), headache (33% vs 0%), maculopapular rash (50% vs 11%), nausea (83% vs 11%), neutrophil count reduction (67% vs 22%), platelet count reduction (50% vs 22%) and vomiting (67% vs 0%).

Clinical benefit of vaccination is associated with epitope spreading in patient T cell response against non-vaccine tumor and vascular antigens, and with increased TCR convergence

Given previous reports for epitope/determinant spreading in vaccinated patients with melanoma with superior outcomes in immunotherapy trials,[16] and the ability of dasatinib to improve epitope spreading when

A

Pat. #	Arm	Vaccine Antigens: DLK1	EphA2	HBB	NRP1	RGS5	TEM1	Acquired Reactivity Against Non-Vaccine Peptides? (# Total of 7)	OCR	PFS (Mos)	OS (Mos)	Resistance to Checkpoint Blockade (Primary/Acquired)?	Gender (F/M)
1	B	■	■	■	■	■		M, G, T, N, P, V1, V2 (7)	PR	13.6	20.3	Primary [b,c]	F
2	B	■	■	■			■	M, G, T, N, P, V1, V2 (7)	PR	4.3	28.4	Primary [b]	M
4	A							None	PD	2.0	3.5	Primary [b], Acquired [a]	F
5	B	■		■	■	■		P (1)	PR	11.5	11.5	Primary [a,b]	F
6	B							None	PD	2.2	17.8	Primary [a]	M
7	A							G (1)	PD	2.2	3.7	Primary [a], Acquired [b]	M
⑨	A	■	■	■	■	■	■	M, G, T, N, P, V1, V2 (7)	SD	8.5	15.2	Primary [a], Acquired [b]	M
10	A							None	PD	1.9	3.0	Primary [b,c]	M
12	B							G (1)	PD	2.1	9.1	Primary [a], Acquired [b]	M
13	A							G (1)	SD	8.3	8.3	Primary [b]	M
14	B	■		■	■			M, G, T, N, V2 (5)	PR	25.3	25.6*	-	F
15	A							None	PD	1.9	15.2	Primary [b], Acquired [a]	M
16	A	■			■	■		G (1)	SD	9.7	20.0*	Acquired [a,b]	F
	# Pts	6	3	5	5	4	4						

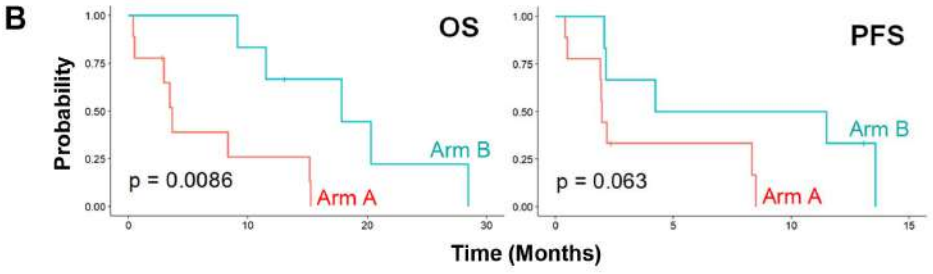

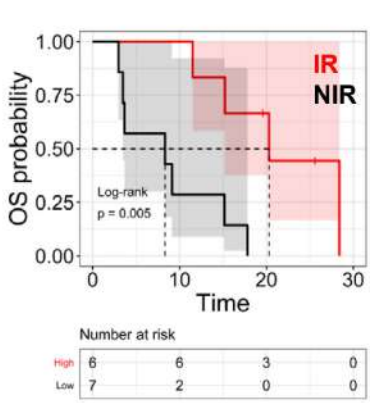

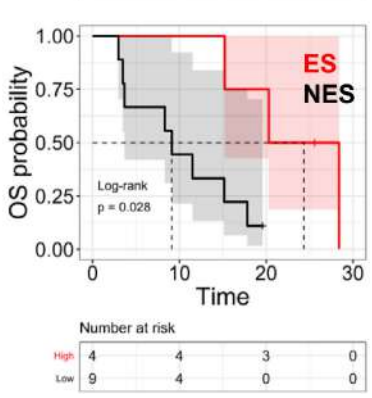

Figure 2 Summary of immunologic and clinical response data. In (A), a summary is provided for individual patient treatment arm, response to individual TBVA peptides used in the vaccine and spread (non-vaccine) peptides derived from TBVA or melanoma-associated antigens (interferon-γ enzyme-linked immunosorbent spot), OCR, PFS, OS, prior primary or acquired resistance to treatment with checkpoint blockade, and gender. For resistance to checkpoint blockade status, prior treatments included anti-CTLA4 [a], anti-PD-1 [b] and combined anti-CTLA4 + anti-PD-1 [c]. Pt. # (underlined) indicates patients with uveal melanoma. Circled Pt. # indicates a patient with mucosal melanoma. *indicates patient still alive. In (B), Kaplan-Meier plots comparing treatment arm versus patient OS and PFS are depicted. Patient immune response to vaccine peptides versus epitope spreading in the response to non-vaccine peptides is correlated to patient OS in panels (C and D), respectively. CTLA-4, cytotoxic T lymphocyte-associated antigen-4; ES, epitope spreading; IR, immune response to vaccine peptides; Mos, Months; NES, no epitope spreading; NIR, no immune response to vaccine peptides; OCR, objective clinical response; OS, overall survival; PD, progressive disease; PFS, progression-free survival; PR, partial response; Pt. patient; SD, stabilization of disease; TBVA, tumor blood vessel antigens.

combined with DC/peptide-based vaccination in murine melanoma models,[12] we investigated on-treatment patient peripheral blood CD8$^+$ T cell reactivity against HLA-A2-presented, vaccine-unrelated peptide epitopes (ie, NV peptides) derived from melanoma antigens (MART-1, gp100, tyrosinase) or TBVA (NRP1, PDGFRβ, VEGFR1, VEGFR2) using IFN-γ ELISPOT assays (figure 1C,E and 2A). As exemplified for patients #1 and #5 (both PR, Arm B) in figure 1C,E, spread T cell responses were detected in patient peripheral blood on-treatment largely in a temporally coordinate manner with (or slightly delayed from) specific T cell responses against vaccine peptide epitopes, with spread responses against > 2 of the seven screened NV peptides only detected in patients #1 (PR), #2 (PR), #9 (SD) and #14 (PR) (figure 2A). The number of vaccine peptides recognized by patient peripheral blood T cells on-treatment was correlated with the number of NV peptides recognized by that same individual (p=0.0019; online supplemental figure S2). When considering T cell responses based on the total number of peptide epitopes recognized, patient response to vaccine, NV or total (vaccine + NV) peptide epitopes correlated with both PFS and OS, with the exception of NV peptides and PFS, where only a trend was observed (figure 3A). The aggregate frequency of CD8$^+$ T cell responses (in IFN-γ ELISPOT assays) appeared better correlated with OS versus PFS for vaccine (p=0.0052vs p=0.229), NV (p=0.0047vs. p=0.109) and total (p=0.0016vs. p=0.167) peptides (figure 3B).

As baseline or on-treatment TCR repertoire diversity has been reported to represent a prognostic indicator of clinical outcome and response to checkpoint blockade in patients with cancer,[17] we next performed TCRseq analyses of patient peripheral blood specimens using the Thermo Fisher Oncomine TCRB-LR Assay.[18] In particular, we focused on determining the relationship of baseline versus on-treatment TCR clonotypic evenness (ie, degree of oligoclonality) and convergence (ie, frequency of non-identical variable-diversity-joining (VDJ) recombination events resulting in identical TCR protein sequence/

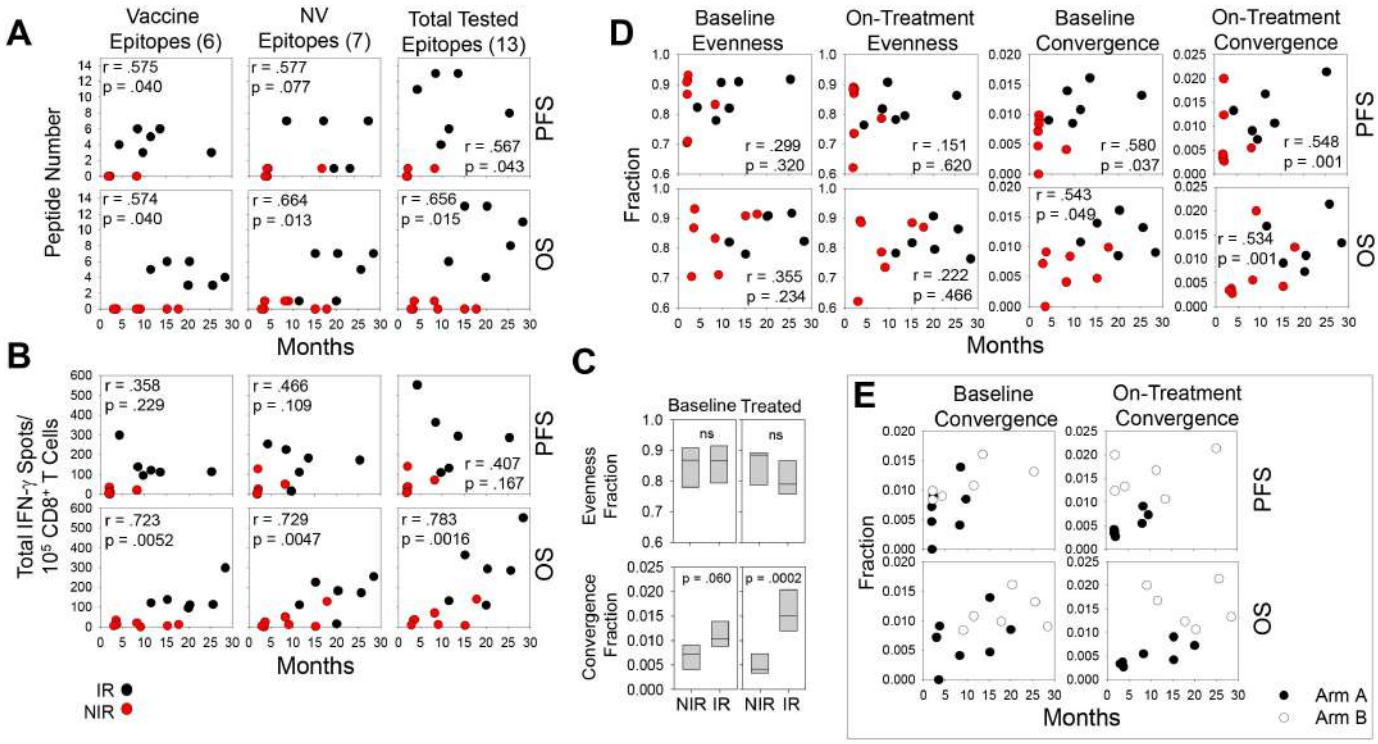

Figure 3 Patient peripheral blood T cell response to vaccine peptides, epitope spreading in the T cell response and baseline TCR convergence are correlated with OCR in treated patients. In (A), patient T cell response to peptide number (vaccine, non-vaccine (NV), total) is plotted as a function of PFS, OS. In (B), aggregate number of spots per 10^5 peripheral blood T cells reactive against screened (vaccine, NV, total) peptides is plotted as a function of PFS, OS. In (C), TCR evenness and convergence in baseline versus on-treatment peripheral blood T cells is reported in immunologic responders (IR) versus patients with no immune response (NIR) to vaccination (as in figure 2A). In (D and E), baseline and on-treatment TCR evenness and convergence are plotted versus patient PFS, OS. In panels (A, B and D), black and red symbols indicate individual patients that were immunologically responsive or non-responsive to vaccine peptides, respectively. In (E), empty versus filled symbols indicate individual patients discriminated by treatment arm. IFN, interferon; OCR, objective clinical response; OS, overall survival; PFS, progression-free survival; TCR, T cell receptor.

antigenic specificity and indicative of antigenic focus) in patients' peripheral T cell repertoires with response to vaccination, OS and PFS. We observed that while evenness in patients' TCR repertoires at baseline or on-treatment failed to correlate with immunologic response to vaccination or to patient PFS or OS (figure 3C,D), TCR convergence was significantly associated with all three of these trial endpoints (figure 3C–E). This was most evident for baseline and on-treatment TCR convergence in the peripheral blood repertoire (figure 3C,D), which was associated with patient immunologic response to vaccination (baseline: p=0.060; on-treatment: p=0.0002), PFS (baseline: p=0.037; on-treatment: p=0.001) and OS (baseline: p=0.049; on-treatment: p=0.001). The highest levels of baseline and on-treatment TCR convergence were observed in patients treated on trial Arm B (baseline: p=0.047; on-treatment: p=0.00015 for Arm B vs Arm A), in association with superior RECIST V.1.1 OCR (0.0123±0.0026 vs 0.0054±0.0027, p=0.0077 for PR vs PD) and spreading in the T cell repertoire (p=0.0022; online supplemental figure S3). Peripheral blood TCR convergence in these treatment-responsive (PR) patients either remained stable or it increased over time (>5 weeks) on treatment (online supplemental figure S4).

These data suggest that αDC1-TBVA peptide-based vaccines were most effective in patients who were immunologically competent to (1) respond to vaccine inclusive peptide epitopes and (2) coordinately develop spreading in their antitumor T cell repertoires. Therapeutic T cell responses were not characterized by the expansion of dominant T cell clonotypes within the peripheral repertoire, but rather with the development of polyclonal populations of T cells exhibiting common specificity (ie, convergence).

αDC1 biomarkers predict patient immunologic response to vaccination and OS

To determine characteristics of the autologous αDC1 cell product that might be associated with patient on-treatment T cell responses against vaccine epitopes (ie, immune response (IR)) and beneficial clinical outcome (ie, PR), patient vaccine DC were phenotypically-profiled and transcriptionally-profiled in exploratory analyses. Levels of cytokines secreted from patient αDC1 were also analyzed by ELISA. We observed that DC expression (%-positive and mean fluorescence intensity (MFI)) of biomarkers traditionally used in αDC1 cell product release criteria, including CD11c, CD14, CD25, CD40,

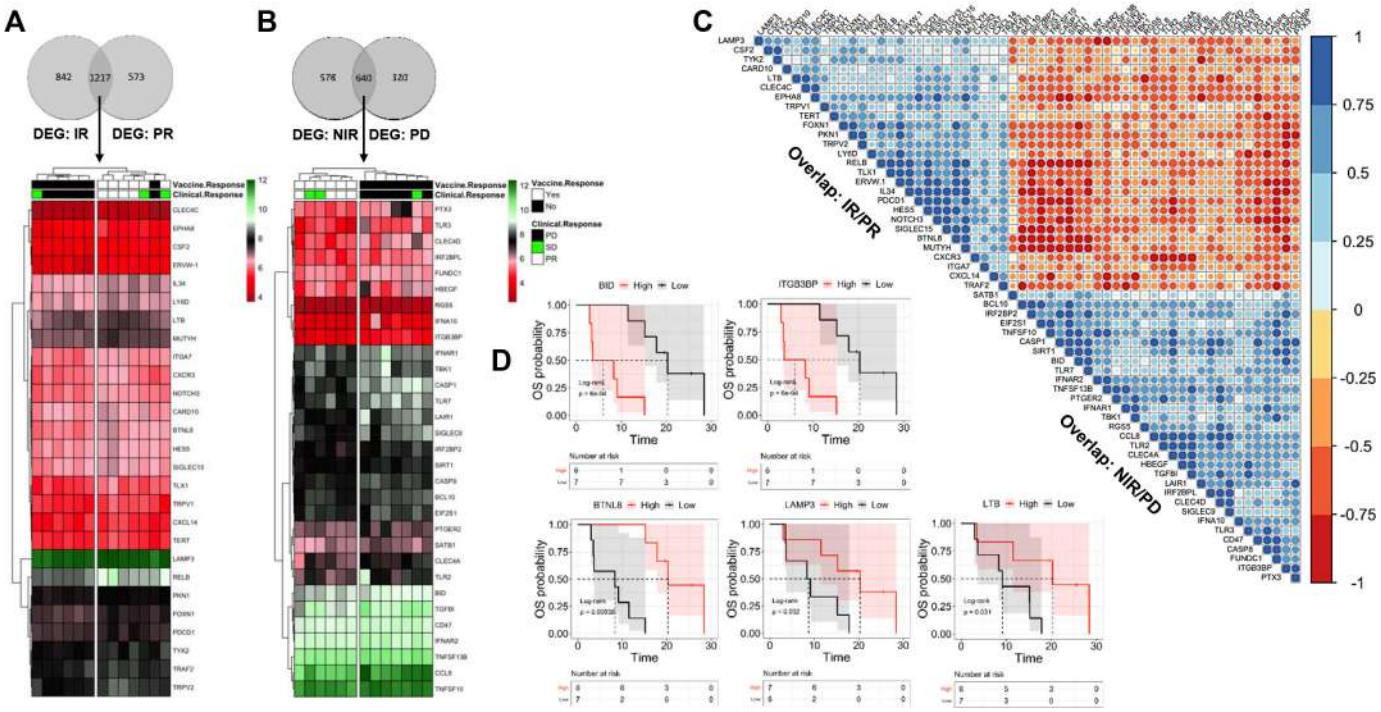

Figure 4 Analysis of αDC1 cells for biomarkers associated with immunologic and clinical response to therapeutic vaccination. Affymetrix gene chips were used to analyze patient αDC1 vaccine cells (n=13) for DEG associated with immune response (IR) and PR status to vaccination (A) or no immune response (NIR) and PD status post-vaccination (B), with data reported in depicted heat maps. In (C), a correlation matrix is provided for DEGs associated with preferred treatment outcomes (IR and PR) versus poor outcomes (NIR and PD). In (D), representative DEGs correlated negatively or positively with patient OS are depicted in Kaplan-Meier plots. BID, two times per day; DEG, differentially expressed genes; OS, overall survival; PD, progressive disease; PR, partial response; SD, stabilization of disease; αDC1, autologous type-1 dendritic cells.

CD80, CD83, CD86, CD206, CCR7 and HLA-DR failed to discriminate vaccine DC generated from responders versus non-responders (data not shown). Extended flow cytometry analyses of cell surface costimulatory and checkpoint molecules on vaccine αDC1 similarly failed to identify potential biomarkers associated with treatment outcome, with the possible exception of OX40L, which appeared to be expressed at higher levels on αDC1 from patients who failed to respond immunologically to vaccination (online supplemental figure S5; p = 0.035). Analyses of levels of interleukin (IL)-12p70 and IL-10 secreted by vaccine αDC1 did not identify differences associated with patient immunologic or clinical response to treatment (data not shown).

Using Affymetrix gene chip profiling, we then compared αDC1 between patients differing in immunologic response to vaccine peptides (based on IFN-γ ELISPOT assays) and OCR (figure 4). We identified 2059 and 1790 DEG positively associated with T cell responses and PR status on-trial, respectively, with 1217 overlapping DEG identified in these cohorts (figure 4A). Examples of overlapping DEG with high correlations with extended OS included *BTNL8, CSF2/GMCSF, CXCL14, CXCR3, IL34, IRF3, LAMP3, LTB, LY6D, PKN1, RELB, TRAF1 and TRAF2*, among others (figure 4A,C and D). Conversely, αDC1 transcripts associated with patient lack of immunologic response, disease progression and shorter OS included *BID*, *CD47*, *CLEC4C*, *IL18BP* (encoding an IL-18 decoy receptor), *ITGB3BP*, *LAIR*, *PTGER2*, *SIRT1*, *SATB1*, *TGFBI*, and interestingly, *RGS5* (one of the TBVA targeted in this vaccine trial), among others (figure 4B–D). Gene set enrichment analyses (GSEA) supported the predominance of gene signatures associated with deficiency in antigen-presenting cell function, IFN/Toll-like receptor (TLR)/IL1 family cytokine signaling and pyruvate metabolism/tricarboxylic acid (TCA) cycle in vaccine αDC1 from NIR/PD versus IR/PR patients (online supplemental figure S6).

Vaccine efficacy is only moderately inversely correlated with changes in regulatory immune cell populations

As we had previously observed that combination vaccines + dasatinib reduced MDSC and Treg frequencies in murine melanoma models,[12] with others reporting that dasatinib reduced circulating levels of MDSC and Treg in treated patients with chronic myeloid leukemia,[19 20] we monitored these immune cell populations in patient peripheral blood on-treatment by flow cytometry. As shown in online supplemental figure S7, peripheral blood $CD4^{+}Foxp3^{+}$ Treg frequencies failed to differ at baseline versus on-treatment (at week 5) between immunologic responders and non-responders to vaccination or between treatment Arms A and B (data not shown). There was a trend (p=0.092) for reduced levels of Treg in PR versus PD patients, and a statistical difference observed for

reduced Treg in PR versus SD (p=0.029) patients on-treatment (online supplemental figure S7B). Except for higher levels of HLA-DR^{neg}CD11b^{+}CD14^{+}CD15^{neg}CD33^{+} monocytic MDSC (M-MDSC) in PR versus PD (p=0.021) and PR versus SD (trend p=0.091) patients at baseline, no other significant differences in M-MDSC and HLA-DR^{neg}CD11b^{+}CD14^{neg}CD15^{+}CD33^{+} PMN-MDSC subsets were observed in patient blood that correlated with immunologic response to vaccination, treatment arm or OCR status (online supplemental figure S7 and data not shown).

Serum analyses for biomarkers of vaccine efficacy

Based on our translational findings for increased in vivo production of the pro-inflammatory chemokine CXCL10 in B16 melanoma-bearing mice treated with combination vaccines + dasatinib,[12] and reports for predictive changes in levels of CXCL10 and soluble checkpoint molecules in the serum/plasma of patients with melanoma effectively treated with immunotherapy,[21 22] we analyzed levels of these factors in patients are at baseline and at week 5 on-treatment. We observed no significant association in serum concentrations of CXCL10 (online supplemental figure S8) or soluble costimulatory/checkpoint molecules (online supplemental figure S9) with immunologic response to vaccination or clinical outcomes.

Activation of intratumoral immunity predicts vaccine clinical activity

Given limiting quantities of tumor biopsy tissue obtained from patients in the current trial, formal histopathologic analyses of vascular normalization, tissue hypoxia, immune cell infiltration and TLS as anatomic structures within the TME could not be performed. Instead, transcriptional profiling was performed on the available biopsy material, including matched baseline and on-treatment tissues from 12 patients (4 PR, 2 SD and 6 PD). Messenger RNA extracted from tumor specimens was analyzed using the OIRRA detecting 395 targets relevant to immune-oncology, and a custom-designed NanoString panel targeting selected gene products associated with TLS formation.

As shown in figure 5A, hierarchical clustering of selected, significant (p<0.05, Wilcoxon test) differentially expressed genes (OIRRA) in baseline tumor biopsies was performed, allowing for segregation of patients based on immunologic and clinical response to treatment. A correlation matrix (figure 5B) was then developed to highlight baseline tumor transcripts associated with best patient outcomes (ie, immune response to vaccination and clinical PR; n=4) versus worst patient outcomes (ie, lack of immune response and clinical PD; n=6). Melanomas in patients responding to the combination vaccine were characterized by genes associated with innate/adaptive immune cell function (*CBLB, CD48, IL2RG, GLNY, KIR2DL2, NCR1, NCR3, SRGN*), antigen presentation (*CD80, CD86, CD226, HLA-DMB, ICOSLG, ITGAM, ITGB2*) and inflammation/immune cell recruitment (*CCL3, CCR5, CD274/PD-L1, CMKLR1, IFIH1, ITGB7*), while baseline tumors in patients who fared poorly on trial expressed elevated levels of transcripts encoding the anti-apoptotic protein BCL2 and CA4, a biomarker of tissue acidosis/hypoxia[23] (figure 5B,C). Baseline tumor *BCL2* and *CA4* expression appeared most strongly negatively associated with *CBLB* and *KIR2DL2* expression (figure 5B). GSEA further revealed baseline enrichment in gene signatures associated with the adaptive immune system, cellular interactions with the vasculature and immunoregulatory interactions between immune and non-immune cell types among patients with IR/PR versus NIR/PD, and conversely enrichment in a (tumor) cell cycle gene signature in patients with NIR/PD versus IR/PD (online supplemental figure S10).

Similar analyses were then performed to determine on-treatment changes in tumor transcriptional profiles associated with therapy outcomes (figure 5D–F). OIRRA-based analyses (figure 5D,E) revealed that tumors in patients that responded immunologically and clinically to vaccination (n=4) became enriched in DEGs associated with inflammatory innate/adaptive immune cell infiltration (*CCL2, CD22, CX3CL1, FCGR3A, GNLY, HLA-DQB2, ID3, JAML, KIR2DL2, MRC1, S100A8, S100A9*). Conversely, as shown in figure 5D–F, tumors in patients that progressed on trial (n=6; all of whom failed to respond immunologically to vaccination) were enriched in DEGs associated with tissue hypoxia (*HIF1A*), glycolysis (*IRS1*), tumor cell proliferation/renewal and DNA repair (*BRCA2, KIAA0101, MELK, MKI67, TOP2A*), tumor cell metastasis (*ITGAE*) and immune suppression (*PTPN11*). Correlation matrix analyses suggest strongest general negative associations between *IRS1* and *PTPN11* with on-treatment biomarkers linked to immune/clinical response to vaccination (figure 5E). GSEA supported on-treatment enrichment in gene signatures associated with adaptive and innate immunity, (MHC I) antigen processing and cross-presentation, immune interactions with blood vessels and neutrophil degranulation in patients with IR/PR versus NIR/PD (online supplemental figure S10). As was the case for baseline tumor analyses, a (tumor) cell cycle gene signature was enriched in patients with NIR/PD versus IR/PD (online supplemental figure S10).

Development of a TLS transcriptional profile in tumors on-treatment predicts immunologic/clinical outcomes

Based on recent reports linking patient with melanoma response to immunotherapy with the presence or treatment-induced formation of tertiary lymphoid structures (TLS) within the TME,[24–26] we developed a custom NanoString probe set for 23 TLS-associated genes and analyzed RNA isolated from patient tumor biopsies at baseline and for changes in transcript expression on-treatment. While baseline profiling of TLS-associated gene transcripts was not predictive of subsequent patient response to vaccination (figure 6A), hierarchical clustering of TLS-associated DEGs segregated patients with

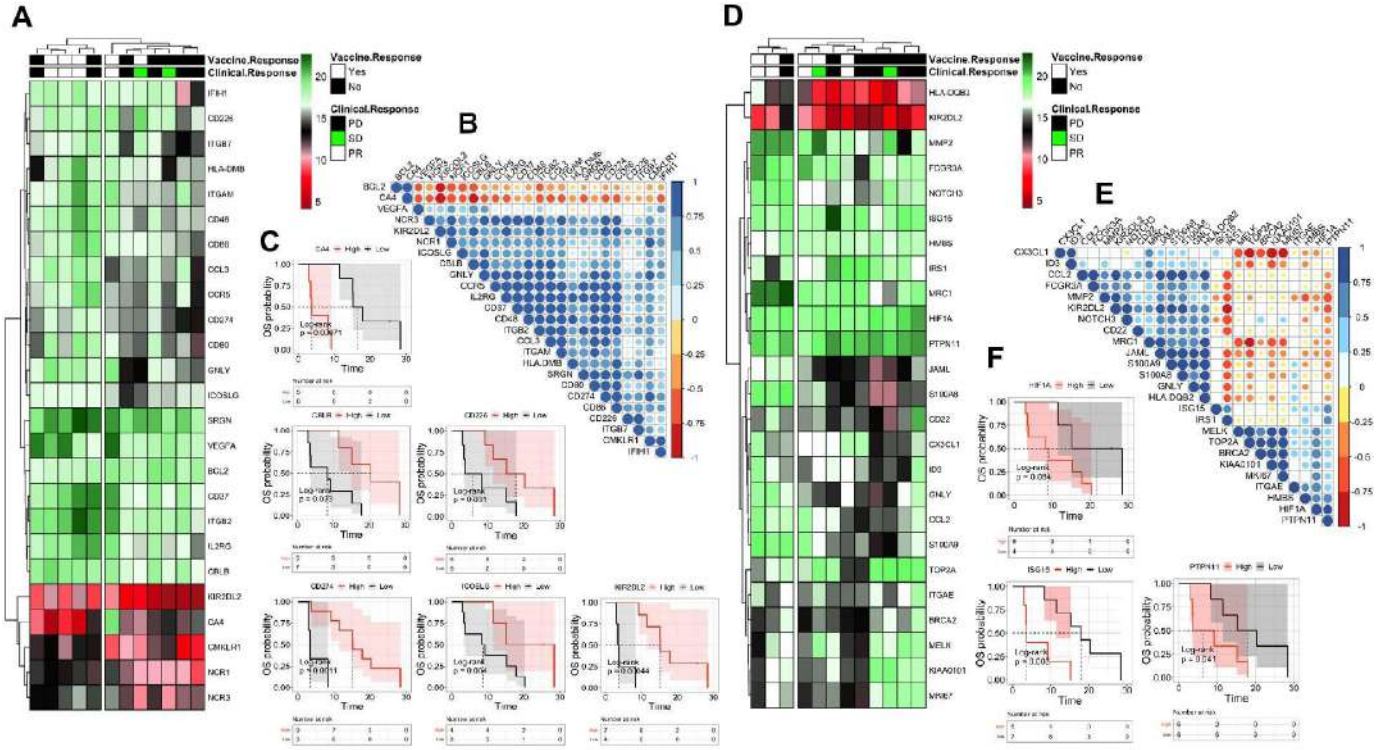

Figure 5 Transcriptional profiling of tumor biopsies for predictive DEG associated with patient outcomes on trial. Oncomine Immune Response Research Assay profiling of tumor biopsy tissues was performed as outlined in Materials and Methods. Hierarchical clustering of selected, significant (p<0.05, Wilcoxon test) DEGs in patient baseline (A) and on-treatment (D) tumor biopsies (n=12) is shown. The genes shown were selected from two individual differential expressional analyses: (1) PR versus PD and (2) (vaccine-induced, antigen-specific) immune response (IR) versus no immune response (NIR). Data is clustered by objective clinical response and immune response of each patient. Rows represent individual genes and columns represent individual patient tumor samples. Gene expression is expressed as log2 normalized read counts. Correlation matrices for baseline (B) and on-treatment (E) tumor DEG associated with IR/PR versus NIR/PD are depicted. Spearman's correlation coefficients were calculated. Positive and negative correlations are shown in blue and red, respectively. The size of the circle and color intensity are proportional to the calculated Spearman's correlation coefficient. Kaplan-Meier estimates of survival based on the expression of representative baseline (C) and on-treatment (F) tumor DEGs are reported. The logrank test was used to test the significance and censored patients were indicated by a vertical line. The median survival for each group is indicated by the dotted line. DEG, differentially expressed genes; OS, overall survival; PD, progressive disease; PR, partial response; SD, stabilization of disease.

vaccine/clinical responses versus those with progressive disease that failed to respond immunologically to the vaccine (figure 6B). Specifically, as shown in figure 6B,C, only patients with positive outcomes displayed increased on-treatment expression of gene transcripts linked to TLS formation (*CCL19, CCL21, LTA, LTB, TNFSF14*), high endothelial venule development (*CHST2, FUT4*), immune cell infiltration and inflammation (*CD8A, CD20, CD274, CXCL10, IFNG, LAMP3, TBX21*). Patient #13 (SD, immunologic non-responder) clustered with PD patients in exhibiting a deficiency in expression of TLS-associated biomarker transcripts. Furthermore, we noted that the emergence of a TLS biosignature in the therapeutic TME was strongly correlated (p<0.001) with epitope spreading in the peripheral $CD8^+$ T cell repertoire (figure 6D,E). Hence, while we were unable to assess histopathologic presence of TLS in situ due to limited amounts of tumor biopsy tissue, these data suggest that effective vaccination against TBVA may promote a therapeutic TME characterized by a TLS transcriptional bio-signature and epitope spreading in the peripheral T cell repertoire.

DISCUSSION

In this pilot phase II trial, we observed that treatment of advanced, patients with checkpoint-refractory melanoma with an autologous αDC1-based vaccine targeting TBVA together with a TME conditioning agent (dasatinib) was safe, immunogenic and therapeutically effective. These results parallel findings in our preclinical tumor models.[12] AEs were consistent with those observed in previous clinical studies of dasatinib monotherapy,[27 28] with no discernable impact from the vaccine component in the combination regimen, as one would predict from the consensus safety profile (ie, grade 1–2 skin reactions, flu-like symptoms) for past DC/peptide-based vaccines administered alone or in combination with alternate interventional agents.[29]

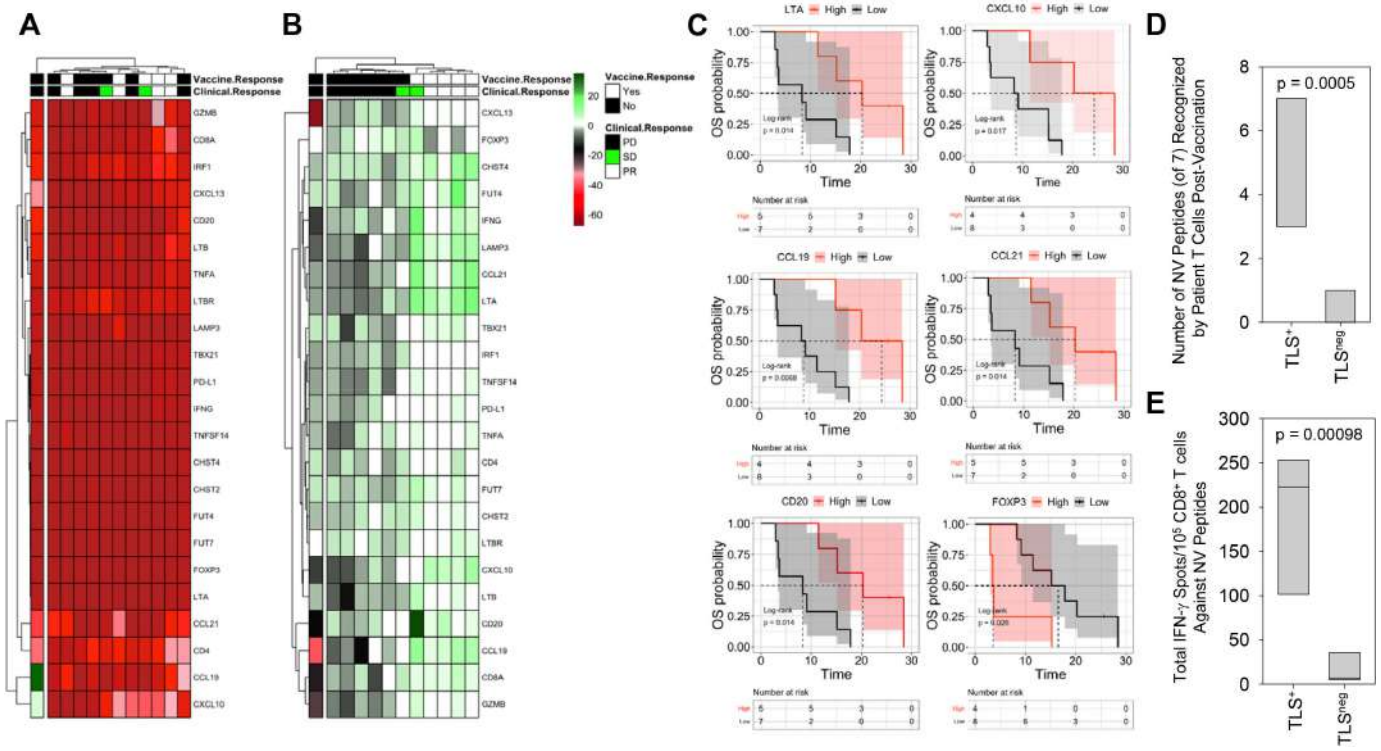

Figure 6 Acquisition of TLS-associated DEG in the tumor microenvironment on-treatment predicts patient immunologic/clinical response to therapeutic vaccination. Tumor biopsies isolated at baseline and 5 weeks after beginning treatment were processed to recover total RNA which was analyzed using a custom NanoString array targeting pro-inflammatory/pro-TLS transcripts, as outlined in Materials and methods. Hierarchical clustering of selected, significant (p<0.05, Wilcoxon test) DEG in patient baseline tumor tissues (A) or from on treatment versus baseline time points (B) are depicted (n=12 in both cases). The data are clustered based on the OCR and IR status of each patient. Rows represent individual proteins and columns represent individual patients. In (C), Kaplan-Meier estimates of survival based on the expression of representative DEGs associated with changes in immunologic/clinical response on-treatment are reported for LTA, CXCL10, CCL19, CCL21, CD20 and Foxp3. Patient peripheral blood T cell response to non-vaccine (NV) peptides (as reported in figure 2A, online supplemental figure S3A,B) based on total number of NV peptides reacted against (D) and total IFN-γ spots/10^5 $CD8^+$ T cells against NV peptides (E) and were plotted versus patient on-treatment TLS status based on biomarker signature. Patients with TLS biosignatures (TLS^+; n=5; Pt. #'s 1, 2, 5, 9, 14). Patients without TLS biosignatures (TLS^{neg}; n=7; including Pt. #'s 4, 6, 7, 10, 12, 13, 15). Differences between groups were determined by student t-test. IFN, interferon; IR, immune response; OCR, objective clinical response; OS, overall survival; PD, progressive disease; PR, partial response; Pt., patient; SD, stabilization of disease; TLS, tertiary lymphoid structure.

Given previous reports for clinical efficacy of DC-based vaccines being associated with patient with melanoma T cell responses against multiple versus single target epitopes,[30] our primary endpoint required patient T cell reactivity against three or more vaccine peptides for designation as a positive response. Six of 13 evaluable patients developed specific $CD8^+$ T cell responses to ≥3 vaccine peptides on-treatment (ie, 46% IRR), with all of the immunologic responder patients exhibiting preferred clinical outcomes (ie, 4 PR and 2 SD). Notably, in patients responding to vaccination, anti-TBVA peripheral blood T cell responses undulated over time on treatment, consistent with results from prior DC-based vaccine trials[31–33] and suggestive of reiterative temporal rounds of specific T cell cross-priming and recruitment of vaccine-induced T cells from blood into the TME. Conversely, seven evaluable patients who failed to respond to vaccination had comparatively poor clinical outcomes (one SD and six PD). Remarkably, patients treated on Arm B developed superior outcomes versus patients treated on Arm A with respect to IRR (66.7% vs 28.6%), ORR (66.7% vs 0%), OS (median 15.45 vs 3.47 months) and PFS (median 7.87 vs 1.97 months). By comparison, a phase II study of dasatinib (70 mg two times per day) monotherapy in 51 evaluable patients with advanced-stage melanoma yielded an ORR of 5.9%, with median OS and PFS of 7.5 and 2.1 months, respectively.[27]

The observed inter-cohort differences in immunologic/clinical outcomes could reflect the benefit of dasatinib administered during the initial vaccine priming phase of therapy for patients on Arm B versus Arm A, with the latter patients receiving vaccine alone for the first cycle of treatment. In this regard, dasatinib has been previously reported to enhance specific T cell cross-priming and to improve OS in murine tumor (melanoma, breast carcinoma) models treated with combination vaccine protocols.[12 34] Dasatinib is also known to improve innate pro-inflammatory natural killer (NK) effector cell activity[35] and to enhance the immunostimulatory capacity of DC,[36] while coordinately reducing

levels of immunoregulatory cell populations such as Treg and MDSC in the TME of treated animals.[12] Any of these drug-associated effects would be anticipated to augment DC-mediated CD8+ T cell cross-priming in vivo.[37] With these caveats, we observed that while the magnitude of peak T cell responses against vaccine and non-vaccine peptides did not differ significantly between the immunologic responders in Arm A versus Arm B (data not shown), the kinetics of patient T cell responses were strikingly different based on treatment arm. On-treatment time to first detection of positive patient T cell response against vaccine peptides was 3.5±1.0 weeks in Arm B versus 8.5±0.7 in Arm A (p=0.0035, t-test), while time to first detection of positive patient T cell response to non-vaccine peptides was 3.9±1.1 weeks in Arm B versus 9.5±0.7 weeks in Arm A (p=0.0018, t-test). This temporal shift in patient response between the two treatment arms roughly approximates to the delay in initiating dasatinib administration as a co-therapeutic agent/vaccine adjuvant to patients treated on Arm A, suggesting the importance of dasatinib in enabling vaccine-induced T cell (cross)priming by the combination regimen.

Counterintuitively, dasatinib can also (reversibly) inhibit lymphocyte cell-specific protein-tyrosine kinase (LCK), a Src-family tyrosine kinase required for effective TCR-mediated signaling in T cells.[38] In this regard, it has been suggested that transient interruption of TCR signaling in the cancer setting may be beneficial to sustaining antitumor T cell fitness and preventing T cell apoptosis due to chronic antigen-specific stimulation.[12] Expanded studies evaluating the fitness and polyfunctionality of therapeutic T cells in the periphery and the TME of treated individuals will be required to address these mechanistic possibilities in future dasatinib-based combination immunotherapies.

An alternate or additional consideration impacting the apparent superior efficacy of the Arm B regimen in our study may reflect an imbalance in male/female composition among evaluable patients in the two treatment arms (ie, 2/7 (28%) women in Arm A vs 3/6 (50%) women in Arm B). As such, the data could support possible gender bias in IRR (80% vs 25%) and ORR (60% vs 12.5%) favoring female versus male patients treated on the Arm B versus Arm A regimens, respectively. Interestingly, a growing literature argues for the convention that women (and males with hypogonadism) exhibit stronger pro-inflammatory responses when compared with intact men, with women at higher risk to develop autoimmune-related pathologies.[39–41] Indeed, 80% of systemic autoimmune diseases have been reported to occur in women.[41] Relevant to the UPCI 12-048 trial, women have also been reported to respond more robustly than men to vaccination in the infectious disease setting,[39 40] in murine tumor models receiving anti-PD-1 checkpoint blockade immunotherapy,[42] and in patients with melanoma with low-moderate levels of partially-exhausted cytotoxic CD8+ T lymphocytes receiving combination anti-PD-1-based immunotherapies.[43 44] Such female versus male dominance in response to immunotherapy has been correlated to sex-associated differences in the microbiome,[45 46] gene-dosing effects of X-chromosome-linked immune gene products, and the comparative immunostimulatory versus immunoregulatory action of estrogens versus androgens, respectively.[43] However, there are reports that clearly support an opposing viewpoint for the superior efficacy of vaccines and checkpoint blockade-based interventions in men versus women.[47 48] These contrasting results may relate to the specific immune pathways primarily targeted by the applied regimens, with gender-dimorphism in the targeted pathways dictating differential outcomes to treatment between the sexes. Given the greater incidence of solid cancers in men versus women,[49] it will be important that prospective translational and clinical studies of (combination vaccine) immunotherapies be designed in accordance with sex and gender equity in research guidelines.[50] Furthermore, confounding variables such as age, sex hormone concentrations, hormone replacement therapies, body mass index and menopausal status should be factored into the analysis and interpretation of future study outcomes as potential covariates.

Our trial included patients with cutaneous, mucosal and uveal melanoma, with the latter indications notoriously difficult to treat with interventional therapies, including immunotherapies.[51] Notably, the demographics of patient site of primary melanoma differed between the treatment arms (figure 2A, online supplemental table S1) which could conceivably impact vaccine outcomes, with Arm A containing a higher frequency of patients with uveal melanoma (44.4% vs 16.7% in Arm B) and mucosal melanoma (11.1% vs 0% for Arm B) and Arm B containing more patients with cutaneous melanoma (83.3% vs 44% in Arm A). However, IRR was greater for both cutaneous (60% vs 0%) and uveal (100% vs 25%) patients with melanoma treated on Arm B versus Arm A, and PR to treatment was observed in 60% versus 0% of patients with cutaneous melanoma and 100% versus 0% of patients with uveal melanoma treated on Arm B versus Arm A (figure 2A). These data suggest that the Arm B treatment regimen may be superior to Arm A irrespective of the patient's site of primary disease.

As was the case in foundational murine melanoma modeling developed using this combined vaccine approach,[12] we observed that patients that coordinately developed CD8+ T cell responses against multiple vaccine peptides and OCR also displayed evidence for expanded T cell reactivity against antigens that were not targeted in the vaccine, but which are considered disease-relevant as they derive from known melanoma differentiation antigens or TBVA. Such DC-dependent spreading in the peripheral T cell repertoire has been previously reported to occur in patients exhibiting OCR after treatment with a range of immunotherapies (ie, vaccines, gene therapies, checkpoint blockade, recombinant cytokines; online supplemental table S1).[14 15 52] In such cases, the extended T cell response against tumor (differentiation, oncofetal, mutated neo-) antigens is believed to improve immune-mediated control of antigenically-diverse tumor lesions, providing an operational improvement in immune

surveillance over that enforced by vaccine-specific T cells or adoptively-transferred monospecific T cells.[14 52 53]

As an alternate means to assess changes in the patient's T cell repertoire on trial, coordinate profiling of TCRVβ chain transcripts was performed. In contrast to several recent reports associating baseline/on-treatment peripheral blood TCR clonotypic evenness with improved PFS, OS, ORR and/or OCR in trials administering cancer vaccines or checkpoint blockade,[17 54] we did not observe a significant association between baseline or on-treatment TCR evenness in peripheral blood with patient responsiveness to vaccination, PFS, OS or OCR (figure 3). However, we did identify significant associations between TCR convergence (indicative of antigen-driven responses) and IRR, PFS, OS and OCR in baseline and (particularly) on-treatment peripheral blood specimens that were analyzed (figure 3). These findings are similar to those reported by Naidus *et al*[55] where peripheral blood TCR convergence was directly correlated to patient OS after PD-L1 blockade in patients with advanced-stage non-small cell lung cancer. These data suggest that TCR convergence in peripheral blood T cells may represent an actionable biomarker for (1) identification of patients most likely to respond to immunotherapeutic interventions that mechanistically require T cell responses to achieve preferred clinical outcomes and (2) effective longitudinal monitoring of therapeutically meaningful T cell responses in patients on-treatment.

One major unresolved question for the field of DC-based vaccines relates to the identification of biomarkers associated the ability of injected DC to elicit therapeutic antitumor T cell responses in treated patients. Although all patient-derived type-1-polarized αDC1 were generated using a standard operating protocol and passed release criteria for use in vaccine formulations, consistent with recent reports,[15 56] we observed that none of the markers used to traditionally qualify vaccine DC (ie, CD11c, CD14, CD25, CD40, CD80, CD83, CD86, CD206, CCR7, HLA-DR, IL-12p70 production, IL-10 production, IL-12p70/IL-10 ratio) were correlated with patient specific T cell or clinical responses. Extended analysis of costimulatory/coinhibitory molecules on vaccine αDC1 cells by flow cytometry similarly failed to demonstrate associations with patient response to vaccination (online supplemental figure S5), with the exception of OX40L which appeared to be expressed at higher levels on αDC1 generated from patients that failed to respond to vaccination. In this context, it is interesting to note that subsets of $OX40L^+$ DC have recently been reported to selectively promote Treg expansion[57] and melanoma progression.[58]

Despite our general inability to identify potential vaccine bioefficacy markers using protein-based methods, Affymetrix gene chip transcriptional profiling of patient-generated vaccine DC revealed possible associations between preferred outcomes (ie, IRR and OCR) with biomarkers linked to DC maturation (ie, *CSF2/GMCSF, LAMP3, RELB*), naïve T cell priming by antigen presenting cells (ie, *BTNL8*), pro-inflammatory immunity/Type-1 IFN signaling (ie, *CXCL14, CXCR3, IL34, IRF3, PKN1*), cell survival (ie, *TRAF1, TRAF2*) and intriguingly, the formation of lymphoid structures (ie, *LTB, TLX1*).[59 60] Conversely, vaccine DC associated with superior patient IRR/OCR were deficient in expression of gene products associated with immune cell apoptosis (ie, *BID*), immature DC (ie, *CD47, ITGB3BP*) or immune suppression/tolerance (ie, *IL18BP, LAIR, PTGER2, RGS5, SATB1, TGFBI*).[61 62] Gene signature analyses suggested inferiority in overall αDC1 functionality in patients with NIR/PD (online supplemental figure S6). Validation of these DC vaccine biomarkers for their capacity to predict patient IRR/OCR on-treatment will need to be carefully evaluated within the context of immunologic monitoring in future clinical trial designs.

Transcriptional profiling of tumor biopsies at baseline revealed several potential biomarkers associated with immunologic and clinical response to autologous αDC1-based vaccination in the current trial, with GSEA suggesting existing adaptive immune presence as predictive of patient IR/PR status on-treatment (online supplemental figure S10). Consistent with several recent reports, expression of CD274/PD-L1 in baseline tumors appeared predictive of patient response to our immunotherapeutic intervention.[63] These immunologically 'hot' tumors also expressed high levels of a range of transcripts associated with recruitment of inflammatory innate immune effector cells (*CCL3*), including NK andinnate lymphoid cells (*KIR2DL2, NCR1/NKp46, NCR3/NKp30*), secretory/cytolytic cells (*GLNY, SRGN*) and antigen presenting cells (*CD80, CD86, CD226, HLA-DMB, ICOSLG, ITGAM, ITGB2*) into a TME that is deficient in acidosis/hypoxia based on reduced expression of *CA4*.[23] That CBLB expression in baseline tumors was associated with superior response to treatment was somewhat surprising as this E3-ligase has been previously reported to negatively regulate the function of immune cells, including $CD8^+$ T cells and DC.[64] One possible explanation for our observations may reflect the reported need for Src family kinase activation of CBLB for its reported immunoregulatory activity.[65] Hence, provision of the Src inhibitor dasatinib within the context of our combined immunotherapy might be envisioned to release immune cells from CBLB-mediated suppression in support of beneficial immune-mediated treatment outcomes.

Molecular changes in the TME associated with response to vaccination (IR, OCR) included a reduction in hypoxia (*HIF1A*) and glycolysis (*IRS1*) indices, consistent with the expectation for vascular normalization as an endpoint for this vaccine approach targeting TBVA.[8–10] A strengthening of transcript profiles associated with immune cell recruitment (*CCL2, CX3CL1, JAML*), and a more diversified immune cell profile including B cells (*CD22*), DC/macrophages/monocytes (*MRC1, S100A8, S100A9*), NK cells (*FCGR3A/CD16, KIR2DL2*) and secretory/cytotoxic cells (*GNLY*) was observed in the tumors of patients responsive to treatment. Based on reduced levels of *PTPN11/SHP2* transcript expression in the tumors of responding

patients, one may also hypothesize that immune cells within the therapeutic TME may be less encumbered by regulatory signaling molecules containing ITIM motifs, including checkpoint and KIR molecules.[66 67] Surprisingly, OIRRA-based profiling suggested that lower levels of *ISG15* transcript expression in the TME on-treatment were linked to superior OS (figure 5F). Although ISG15 protein has been reported to serve as an effective adjuvant to vaccination,[68] it is also known to represent a biomarker of poor prognosis in the cancer setting[69] and to mediate pro-tumor immunoregulatory activity.[70] GSEA supported enhanced vascular-immune crosstalk, innate and adaptive immune cell presence, and antigen-presenting cell function in the TME of patients with IR/PR versus NIR/PD on trial (online supplemental figure S11).

Complementary NanoString-based transcriptional profiling clearly distinguished patients that performed well on trial (IR, OCR) versus patients that failed to respond to the vaccine either immunologically or clinically (figure 6B). Responding tumors transcript profiles were enriched in biomarkers of inflammation (*CD274, CXCL10, IFNG, IRF1, TBX21, TNFA*), cytotoxic effector cells (*GZMB*) and tertiary lymphoid structures (*CCL19, CCL21, CD8A, CD20, CHST4, CXCL13, FUT4, LAMP3, LTA, LTB, TNFSF14*). These findings are consistent with recent reports supporting the association of TLS neogenesis in the TME with favorable clinical response to immunotherapy.[24 25] It is also interesting to speculate that therapeutic TLS formation in the TME may serve as a center for expanded T cell cross-priming and spreading in the antitumor $CD8^+$ T cell repertoire, since these events were strongly correlated in this trial (p=0.0005 and p=0.00098, respectively; figure 6D,E).

Finally, it is worth noting that all patients treated on this trial had previously received at least one form of prior immunotherapy, including rIL-2, rIFNα, checkpoint blockade and/or vaccines (online supplemental table S1). We observed no apparent impact of prior treatment on patient outcomes on the current trial, with five of the six immunologic/clinical responders having demonstrated primary and/or acquired resistance to prior treatment with checkpoint blockade, and the remaining responder (ie, patient #14) being checkpoint treatment naive (figure 2A). Four patients, including three on treatment Arm A (ie, patients #4, #7, #9) and patient #5 treated on Arm B had received previous autologous DC-based vaccines (ie, adenovirus-engineered DC expressing MAGE-6, MART1 and tyrosinase; online supplemental table S1), however, the vaccine antigens used in the previous trial and the current trial do not overlap and we observed no baseline T cell responses against TBVA antigens in these patients (assuming spreading might could have occurred in T cell responses as a consequence of the prior vaccination regimen).

The authors acknowledge several limitations in this phase II clinical trial including its small sample size, its inclusion of advanced stage patients with cutaneous, mucosal or uveal forms of melanoma, and the characterization of the therapeutic TME which was restricted to use of transcriptional profiling rather than tissue imaging technologies (particularly in the context of TLS). Our findings must be confirmed in larger cohort studies in future trials. In this regard, we plan to extend our investigation of αDC1/TBVA peptide-based vaccines in two NIH-supported, prospective phase II clinical trials to be initiated in 2021. In one trial (NCT04093323), up to 24 advanced-stage HLA-$A2^+$ patients with melanoma with primary resistance to anti-PD-1 will be treated with autologous αDC1/TBVA and a systemic chemokine modulating regimen (ie, combined $IFN\alpha_2$, rintatolimod, celecoxib) designed to enhance vaccine-induced TIL recruitment and to potentially support enhanced TLS formation by sustaining inflammation in the therapeutic TME. In the other trial, up to 21 patients with early-stage HLA-$A2^+$ with clear-cell renal cell carcinoma will receive autologous αDC1/TBVA peptide-based vaccination combined with low-dose cabozantinib in the neoadjuvant setting beginning 6 weeks prior to planned surgery, with tumors evaluated for treatment-associated changes in size, vascular structure, immune infiltration, TIL TCR repertoire and TLS formation.

In summary, our data support the safety and immunogenicity of vaccination against non-mutated TBVAs overexpressed by the tumor-associated vasculature, and they provide a preliminary indication of the therapeutic efficacy of this treatment approach in patients with checkpoint-refractory disease particularly when combined with early dasatinib co-administration. Since the TBVAs targeted in this trial are overexpressed in multiple cancer types, these outcomes have implications for future vaccine protocols designed to treat patients with diverse forms of solid, vascularized tumors.

Author affiliations
[1]Dermatology and Immunology, University of Pittsburgh School of Medicine, Pittsburgh, Pennsylvania, USA
[2]Translational and Regulatory Affairs, Parker Institute for Cancer Immunotherapy, San Francisco, CA, USA
[3]Biostatistics, University of Pittsburgh Graduate School of Public Health, Pittsburgh, Pennsylvania, USA
[4]Biostatistics, UPMC Hillman Cancer Center, Pittsburgh, Pennsylvania, USA
[5]Immunoregulation and Immunodiagnostics, Chittaranjan National Cancer Institute, Kolkata, West Bengal, India
[6]Immunotherapeutics and Biotechnology, Texas Tech University Health Sciences Center, Abilene, Texas, USA
[7]Clinical Research Services, UPMC Hillman Cancer Center, Pittsburgh, Pennsylvania, USA
[8]Medicine, University of Pittsburgh School of Medicine, Pittsburgh, Pennsylvania, USA
[9]Medicine, UPMC Hillman Cancer Center, Pittsburgh, Pennsylvania, USA
[10]Immunology, University of Pittsburgh School of Medicine, Pittsburgh, Pennsylvania, USA
[11]Microbiology and Immunology, LECOM, Greensburg, Pennsylvania, USA
[12]Immunology, Singular Genomics, Austin, Texas, USA
[13]Molecular Biology, Thermo Fisher Scientific, Santa Clara, Carlsbad, California, USA
[14]Medical Oncology and Immunology, Roswell Park Cancer Institute, Buffalo, New York, USA
[15]Research and Development, Parker Institute for Cancer Immunotherapy, San Francisco, California, USA
[16]Microbiology and Immunology, University of California San Francisco, San Francisco, California, USA

[17]Cutaneous Oncology and Immunology, Moffitt Cancer Center, Tampa, Florida, USA
[18]Melanoma Medical Oncology, University of Texas MD Anderson Cancer Center, Houston, Texas, USA
[19]Medicine, University of Pittsburgh, Pittsburgh, Pennsylvania, USA

Twitter Hussein Tawbi @HTawbi_MD

Acknowledgements The authors wish to thank members of our Clinical Research Services (Barbara Stadterman, MPH, CPH, MSCR, CCRP and Mary Horak, BS, CCRP) and our Education and Compliance Office (Nita Missig Carroll, RN, BSN, OCN, CCRC) and Mr Josh Plassmyer for their assistance in protocol performance, regulatory compliance and clinical data analysis, respectively. We also wish to acknowledge the UPMC Hillman Immunologic Monitoring and Cellular Products Laboratory (sustained in part by P30 CA047904) for their outstanding support in DC vaccine manufacture and exploratory serum analyses, and the University of Pittsburgh Genomics Core Facility for their assistance in transcriptional profiling studies. We thank Drs Joseph Baar and Louis D Falo for their critical comments and suggestions made during the preparation of this manuscript.

Contributors Patient enrollment and management: AT, HT, JMK. Protocol coordination and assignment to treatment arm: AR, MD. Designing research studies: WJS, AB, DL, PK, LHB, HT. Conducting laboratory experiments: DM, JLT, MC, RJF, LM, EL. Acquiring data: DM, AR, MD, LK, JLT, MC, RJF, GML, LHB, AT, HT, JMK. Analyzing data: WJS, DM, YL, FD, JLT, MC, RJF, JNF, TJL, AT, HT, JMK. Writing/editing the manuscript: All authors. Guarantor: WJS.

Funding These studies were supported by NIH R01 CA169118 (to WJS), NIH R01 CA204419 (to WJS) and NIH P01 CA234212 (to WJS and PK).

Competing interests WJS, DM, YL, FD, LK, AB, DBL, AR, MD, JLT, MC, RJF, JNF and PK declare no competing interests. TJL was an employee of Thermo Fisher Scientific during the performance of this work. TJL, LM, EL and GML are/were employees of Thermo Fisher Scientific during the performance of this work. LHB declares the following unrelated advisory activities: StemImmune/Calidi Scientific and Medical Advisory Board, April 6, 2017–present; SapVax Advisory Board meetings November 15, 2017; December 6, 2018; NextCure, Scientific Advisory Board, 2018–2020; Western Oncolytics, Scientific Advisory Board, 2018–present; Torque Therapeutics, Scientific Advisory Board, 2018–2020; Khloris, Scientific Advisory Board, 2019–present; Pyxis, Scientific Advisory Board, 2019–present; Cytomix, Scientific Advisory Board, 2019–present; Vir, Scientific Advisory Board meeting, February 2020; DCprime, Scientific Advisory Board meeting, November 2020; RAPT, Scientific Advisory Board, 2020–present; Takeda, Scientific Advisor, 2020–present; EnaraBio scientific advisor, February 2021. AT declares the following unrelated advisory activities: Receipt of fees for consulting and/or advisory board participation from Partner Therapeutics, Merck, Bristol Myers Squibb, Novartis, Genentech-Roche, Array Biopharma, Sanofi-Genzyme/Regeneron, Pfizer, EMD Serono, NewLink Genetics, BioNTech, Immunocore, and Eisai; participation in a Data Safety Monitoring Board for Incyte; involvement with institution contracted research with Merck, OncoSec, Genentech-Roche, Bristol Myers Squibb, Amgen and Clinigen. HT declares the following unrelated consulting Honoraria: BMS, Novartis, Merck, Genentech, Eisai, Iovance, Boxer Capital, Karyopharm. Research Funding to Institution: BMS, Novartis, Merck, Genentech, GSK. JMK declares the following unrelated advisory activities and funding: Advisory Role: Bristol Myers Squibb, Novartis, Iovance Biotherapeutics, Elsevier, Amgen, Checkmate Pharmaceuticals, Harbour BioMed, Istari Oncology, OncoSec, Scopus BioPharma, Pfizer; Speakers' Bureau: Bristol Myers Squibb unbranded IO; Research Funding: Amgen, Bristol Myers Squibb, Castle Biosciences, Checkmate Pharmaceuticals, Immunocore, Iovance Biotherapeutics, Novartis, Merck.

Patient consent for publication Not applicable.

Ethics approval The study was conducted per Declaration of Helsinki principles. Approval to treat patients was obtained from the University of Pittsburgh Cancer Institute (UPCI)/Hillman Cancer Center (HCC) Institutional Review Board (No. PRO12060479). The authors attest that signed informed consent was obtained from all patients entered onto this study.

Provenance and peer review Not commissioned; externally peer reviewed.

Data availability statement Data are available upon reasonable request. The full trial protocol and all data relevant to the study will be provided upon reasonable request.

ORCID iDs
Walter J Storkus http://orcid.org/0000-0001-8961-4444
Geoffrey M Lowman http://orcid.org/0000-0002-1498-4165
Lisa H Butterfield http://orcid.org/0000-0002-3439-9844
Ahmad Tarhini http://orcid.org/0000-0002-3193-9702
Hussein Tawbi http://orcid.org/0000-0003-1942-851X

REFERENCES

1 Cancer Facts and Figures 2020. American Cancer Society, Atlanta, GA, USA, 2021. Available: https://www.cancer.org/content/dam/cancer-org/research/cancer-facts-and-statistics/annual-cancer-facts-and-figures/2021/cancer-facts-and-figures-2021.pdf
2 Balch CM, Gershenwald JE, Soong S-jaw, *et al*. Final version of 2009 AJCC melanoma staging and classification. *JCO* 2009;27:6199–206.
3 Linardou H, Gogas H. Toxicity management of immunotherapy for patients with metastatic melanoma. *Ann Transl Med* 2016;4:272.
4 Ascierto ML, Melero I, Ascierto PA. Melanoma: from incurable beast to a curable BET. The success of immunotherapy. *Front Oncol* 2015;5:152.
5 Melero I, Gaudernack G, Gerritsen W, *et al*. Therapeutic vaccines for cancer: an overview of clinical trials. *Nat Rev Clin Oncol* 2014;11:509–24.
6 Chi M, Dudek AZ. Vaccine therapy for metastatic melanoma: systematic review and meta-analysis of clinical trials. *Melanoma Res* 2011;21:165–74.
7 Zhang Y, Ertl HCJ. Starved and asphyxiated: How can $CD8^+$ T cells within a tumor microenvironment prevent tumor progression. *Front Immunol* 2016;7:32.
8 Zhao X, Bose A, Komita H, *et al*. Vaccines targeting tumor blood vessel antigens promote $CD8^+$ T cell-dependent tumor eradication or dormancy in HLA-A2 transgenic mice. *J Immunol* 2012;188:1782–8.
9 Chi Sabins N, Taylor JL, Fabian KPL, *et al*. DLK1: a novel target for immunotherapeutic remodeling of the tumor blood vasculature. *Mol Ther* 2013;21:1958–68.
10 Komita H, Zhao X, Taylor JL, *et al*. $CD8^+$ T-cell responses against hemoglobin-beta prevent solid tumor growth. *Cancer Res* 2008;68:8076–84.
11 Kluger HM, Dudek AZ, McCann C, *et al*. A phase 2 trial of dasatinib in advanced melanoma. *Cancer* 2011;117:2202–8.
12 Lowe DB, Bose A, Taylor JL, *et al*. Dasatinib promotes the expansion of a therapeutically superior T-cell repertoire in response to dendritic cell vaccination against melanoma. *Oncoimmunology* 2014;3:e27589.
13 Song N, Guo H, Ren J. Synergistic anti-tumor effects of dasatinib and dendritic cell vaccine on metastatic breast cancer in a mouse model. *Oncol Lett* 2018;15:6831–8.
14 Mailliard RB, Wankowicz-Kalinska A, Cai Q, *et al*. alpha-type-1 polarized dendritic cells: a novel immunization tool with optimized CTL-inducing activity. *Cancer Res* 2004;64:5934–7.
15 Butterfield LH, Vujanovic L, Santos PM, *et al*. Multiple antigen-engineered DC vaccines with or without IFNα to promote antitumor immunity in melanoma. *J Immunother Cancer* 2019;7:113.
16 Brossart P. The role of antigen spreading in the efficacy of immunotherapies. *Clin Cancer Res* 2020;26:4442–7.
17 Postow MA, Manuel M, Wong P, *et al*. Peripheral T cell receptor diversity is associated with clinical outcomes following ipilimumab treatment in metastatic melanoma. *J Immunother Cancer* 2015;3:23.
18 Looney TJ, Topacio-Hall D, Lowman G, *et al*. TCR convergence in individuals treated with immune checkpoint inhibition for cancer. *Front Immunol* 2019;10:2985.
19 Giallongo C, Parrinello NL, La Cava P, *et al*. Monocytic myeloid-derived suppressor cells as prognostic factor in chronic myeloid leukaemia patients treated with dasatinib. *J Cell Mol Med* 2018;22:1070–80.

20 Najima Y, Yoshida C, Iriyama N, *et al*. Regulatory T cell inhibition by dasatinib is associated with natural killer cell differentiation and a favorable molecular response-The final results of the D-first study. *Leuk Res* 2018;66:66–72.
21 Mohty A-M, Grob J-J, Mohty M, *et al*. Induction of IP-10/CXCL10 secretion as an immunomodulatory effect of low-dose adjuvant interferon-alpha during treatment of melanoma. *Immunobiology* 2010;215:113–23.
22 Zhou J, Mahoney KM, Giobbie-Hurder A, *et al*. Soluble PD-L1 as a biomarker in malignant melanoma treated with checkpoint blockade. *Cancer Immunol Res* 2017;5:480–92.
23 Winkler CA, Kittelberger AM, Schwartz GJ. Expression of carbonic anhydrase IV mRNA in rabbit kidney: stimulation by metabolic acidosis. *Am J Physiol* 1997;272:F551–60.
24 Cabrita R, Lauss M, Sanna A, *et al*. Tertiary lymphoid structures improve immunotherapy and survival in melanoma. *Nature* 2020;577:561–5.
25 Helmink BA, Reddy SM, Gao J, *et al*. B cells and tertiary lymphoid structures promote immunotherapy response. *Nature* 2020;577:549–55.
26 Petitprez F, de Reyniès A, Keung EZ, *et al*. B cells are associated with survival and immunotherapy response in sarcoma. *Nature* 2020;577:556–60.
27 Kalinsky K, Lee S, Rubin KM, *et al*. A phase 2 trial of dasatinib in patients with locally advanced or stage IV mucosal, acral, or vulvovaginal melanoma: a trial of the ECOG-ACRIN cancer research Group (E2607). *Cancer* 2017;123:2688–97.
28 Kluger HM, Dudek AZ, McCann C, *et al*. A phase 2 trial of dasatinib in advanced melanoma. *Cancer* 2011;117:2202–8.
29 Bol KF, Schreibelt G, Gerritsen WR, *et al*. Dendritic cell-based immunotherapy: state of the art and beyond. *Clin Cancer Res* 2016;22:1897–906.
30 Banchereau J, Palucka AK, Dhodapkar M, *et al*. Immune and clinical responses in patients with metastatic melanoma to CD34(+) progenitor-derived dendritic cell vaccine. *Cancer Res* 2001;61:6451–8.
31 Butterfield LH, Comin-Anduix B, Vujanovic L, *et al*. Adenovirus MART-1-engineered autologous dendritic cell vaccine for metastatic melanoma. *J Immunother* 2008;31:294–309.
32 Butterfield LH, Ribas A, Dissette VB, *et al*. Determinant spreading associated with clinical response in dendritic cell-based immunotherapy for malignant melanoma. *Clin Cancer Res* 2003;9:998–1008.
33 Butterfield LH, Ribas A, Dissette VB, *et al*. A phase I/II trial testing immunization of hepatocellular carcinoma patients with dendritic cells pulsed with four alpha-fetoprotein peptides. *Clin Cancer Res* 2006;12:2817–25.
34 Song N, Guo H, Ren J, *et al*. Synergistic anti-tumor effects of dasatinib and dendritic cell vaccine on metastatic breast cancer in a mouse model. *Oncol Lett* 2018;15:6831–8.
35 Climent N, Plana M. Immunomodulatory activity of tyrosine kinase inhibitors to elicit cytotoxicity against cancer and viral infection. *Front Pharmacol* 2019;10:1232.
36 Chu C-L, Lee Y-P, Pang C-Y, *et al*. Tyrosine kinase inhibitors modulate dendritic cell activity via confining c-Kit signaling and tryptophan metabolism. *Int Immunopharmacol* 2020;82:106357.
37 Boltjes A, van Wijk F. Human dendritic cell functional specialization in steady-state and inflammation. *Front Immunol* 2014;5:131.
38 Mestermann K, Giavridis T, Weber J, *et al*. The tyrosine kinase inhibitor dasatinib acts as a pharmacologic on/off switch for CAR T cells. *Sci Transl Med* 2019;11:eaau5907.
39 Furman D. Sexual dimorphism in immunity: improving our understanding of vaccine immune responses in men. *Expert Rev Vaccines* 2015;14:461–71.
40 Trigunaite A, Dimo J, Jørgensen TN. Suppressive effects of androgens on the immune system. *Cell Immunol* 2015;294:87–94.
41 Gold SM, Willing A, Leypoldt F, *et al*. Sex differences in autoimmune disorders of the central nervous system. *Semin Immunopathol* 2019;41:177–88.
42 Lin P-Y, Sun L, Thibodeaux SR, *et al*. B7-H1-dependent sex-related differences in tumor immunity and immunotherapy responses. *J Immunol* 2010;185:2747–53.
43 Capone I, Marchetti P, Ascierto PA, *et al*. Sexual dimorphism of immune responses: a new perspective in cancer immunotherapy. *Front Immunol* 2018;9:552.
44 Loo K, Tsai KK, Mahuron K, *et al*. Partially exhausted tumor-infiltrating lymphocytes predict response to combination immunotherapy. *JCI Insight* 2017;2:93433.
45 Gopalakrishnan V, Helmink BA, Spencer CN, *et al*. The influence of the gut microbiome on cancer, immunity, and cancer immunotherapy. *Cancer Cell* 2018;33:570–80.
46 Gomez A, Luckey D, Taneja V. The gut microbiome in autoimmunity: sex matters. *Clin Immunol* 2015;159:154–62.
47 Motzer RJ, Escudier B, McDermott DF, *et al*. Nivolumab versus everolimus in advanced renal-cell carcinoma. *N Engl J Med* 2015;373:1803–13.
48 Robert C, Long GV, Brady B, *et al*. Nivolumab in previously untreated melanoma without BRAF mutation. *N Engl J Med* 2015;372:320–30.
49 Botticelli A, Onesti CE, Zizzari I, *et al*. The sexist behaviour of immune checkpoint inhibitors in cancer therapy? *Oncotarget* 2017;8:99336–46.
50 Heidari S, Babor TF, De Castro P, *et al*. Sex and gender equity in research: rationale for the SAGER guidelines and recommended use. *Res Integr Peer Rev* 2016;1:2.
51 Rossi E, Schinzari G, Maiorano BA, *et al*. Efficacy of immune checkpoint inhibitors in different types of melanoma. *Hum Vaccin Immunother* 2021;17:4–13.
52 Ott PA, Hu-Lieskovan S, Chmielowski B, *et al*. A phase Ib trial of personalized neoantigen therapy plus anti-PD-1 in patients with advanced melanoma, non-small cell lung cancer, or bladder cancer. *Cell* 2020;183:347–62.
53 Lai J, Mardiana S, House IG, *et al*. Adoptive cellular therapy with T cells expressing the dendritic cell growth factor Flt3L drives epitope spreading and antitumor immunity. *Nat Immunol* 2020;21:914–26.
54 Charles J, Mouret S, Challende I, *et al*. T-cell receptor diversity as a prognostic biomarker in melanoma patients. *Pigment Cell Melanoma Res* 2020;33:612–24.
55 Naidus E, Bouquet J, Oh DY, *et al*. Early changes in the circulating T cells are associated with clinical outcomes after PD-L1 blockade by durvalumab in advanced NSCLC patients. *Cancer Immunol Immunother* 2021;70:2095–102.
56 Maurer DM, Adamik J, Santos PM, *et al*. Dysregulated NF-κB-dependent ICOSL expression in human dendritic cell vaccines impairs T-cell responses in patients with melanoma. *Cancer Immunol Res* 2020;8:1554–67.
57 Marinelarena A, Bhattacharya P, Kumar P, *et al*. Identification of a Novel OX40L^{+} Dendritic Cell Subset That Selectively Expands Regulatory T cells. *Sci Rep* 2018;8:14940.
58 Aspord C, Leccia M-T, Charles J, *et al*. Plasmacytoid dendritic cells support melanoma progression by promoting Th2 and regulatory immunity through OX40L and ICOSL. *Cancer Immunol Res* 2013;1:402–15.
59 Chapoval AI, Smithson G, Brunick L, *et al*. BTNL8, a butyrophilin-like molecule that costimulates the primary immune response. *Mol Immunol* 2013;56:819–28.
60 Ueno Y, Fujisaki K, Hosoda S, *et al*. Transcription factor Tlx1 marks a subset of lymphoid tissue organizer-like mesenchymal progenitor cells in the neonatal spleen. *Sci Rep* 2019;9:20408.
61 Tesone AJ, Rutkowski MR, Brencicova E, *et al*. Satb1 overexpression drives tumor-promoting activities in cancer-associated dendritic cells. *Cell Rep* 2016;14:1774–86.
62 Carvalheiro T, Garcia S, Pascoal Ramos MI, *et al*. Leukocyte associated immunoglobulin like receptor 1 regulation and function on monocytes and dendritic cells during inflammation. *Front Immunol* 2020;11:11.
63 Lin H, Wei S, Hurt EM, *et al*. Host expression of PD-L1 determines efficacy of PD-L1 pathway blockade-mediated tumor regression. *J Clin Invest* 2018;128:805–15.
64 Li X, Gong L, Gu H. Regulation of immune system development and function by Cbl-mediated ubiquitination. *Immunol Rev* 2019;291:123–33.
65 Okabe S, Tauchi T, Ohyashiki K, *et al*. Stromal-cell-derived factor-1/CXCL12-induced chemotaxis of a T cell line involves intracellular signaling through Cbl and Cbl-b and their regulation by Src kinases and CD45. *Blood Cells Mol Dis* 2006;36:308–14.
66 Li J, Jie H-B, Lei Y, *et al*. PD-1/SHP-2 inhibits Tc1/Th1 phenotypic responses and the activation of T cells in the tumor microenvironment. *Cancer Res* 2015;75:508–18.
67 Lanier LL. NK cell receptors. *Annu Rev Immunol* 1998;16:359–93.
68 Villarreal DO, Wise MC, Siefert RJ, *et al*. Ubiquitin-like molecule ISG15 acts as an immune adjuvant to enhance antigen-specific CD8 T-cell tumor immunity. *Mol Ther* 2015;23:1653–62.
69 Wood LM, Pan Z-K, Seavey MM, *et al*. The ubiquitin-like protein, ISG15, is a novel tumor-associated antigen for cancer immunotherapy. *Cancer Immunol Immunother* 2012;61:689–700.
70 Chen R-H, Xiao Z-W, Yan X-Q, *et al*. Tumor cell-secreted ISG15 promotes tumor cell migration and immune suppression by inducing the macrophage M2-like phenotype. *Front Immunol* 2020;11:594775.